



저작자표시-비영리-변경금지 2.0 대한민국

이용자는 아래의 조건을 따르는 경우에 한하여 자유롭게

- 이 저작물을 복제, 배포, 전송, 전시, 공연 및 방송할 수 있습니다.

다음과 같은 조건을 따라야 합니다:



저작자표시. 귀하는 원저작자를 표시하여야 합니다.



비영리. 귀하는 이 저작물을 영리 목적으로 이용할 수 없습니다.



변경금지. 귀하는 이 저작물을 개작, 변형 또는 가공할 수 없습니다.

- 귀하는, 이 저작물의 재이용이나 배포의 경우, 이 저작물에 적용된 이용허락조건을 명확하게 나타내어야 합니다.
- 저작권자로부터 별도의 허가를 받으면 이러한 조건들은 적용되지 않습니다.

저작권법에 따른 이용자의 권리는 위의 내용에 의하여 영향을 받지 않습니다.

이것은 [이용허락규약\(Legal Code\)](#)을 이해하기 쉽게 요약한 것입니다.

[Disclaimer](#)

Experimental Study on Flow Separation Upstream of a  
Riverine Weir

하천보 상류에서 발생하는 흐름 박리에 관한  
실험적 연구

December 2019

**Graduate School of Civil and Environmental Engineering**

**Seoul National University**

**Joo Young Bang**

# Abstract

The flow separation upstream of the riverine weir was investigated by the laboratory experiments using two-dimensional particle image velocimetry (PIV). The shape of the riverine weir was a typical finite-crested weir with a vertical front and a downstream ramp determined by the Korean River Design Standard. The hydraulic conditions of the experiments reflect the relationship between the upstream and downstream water depth.

The streamlines calculated from the mean streamwise and vertical velocity show the region of recirculation at the bottom upstream of the weir, and it is bounded by the outer flow. The reverse flow was developed in this region. From the root-mean-square streamwise and vertical velocity fields, substantial unsteadiness was found at the center of the rotating vortex.

The snapshot proper orthogonal decomposition (SPOD) was implemented to extract the deterministic velocity fields from the fluctuation velocity. The first mode has 20~25% of the energy level. The first three modes of streamwise and vertical velocity in each experimental case have similar shapes, but the sizes were changed according to the hydraulic conditions.

The conditional averaging of the total area of the reverse flow was applied for the estimation of the separation flow intensity at each time instant. The region of reverse flow is right-skewed distribution and always larger than 0. About 40% of the separation flow is closed-form. A massive ejection of upstream separation flow occurs, which implies that the separation flow over the weir is partially influenced by that upstream of the weir. The relationship between separation points and the area of reverse flow was analyzed, and it well represents the right-skewed distribution and the massive ejection.

The separation point at the channel bed and the reattachment point at the weir wall were estimated by the method of zero mean shear stress and the fraction of time. Although the distance of the separation and reattachment points are slightly influenced by the weir Reynolds and Froude number, they are highly dependent on the upstream water depth.

Keywords: Riverine weir, PIV, Boundary layer separation, Conditional averaging, Reverse flow, Snapshot POD.

# Table of Contents

## 1. Introduction

1.1. Research Background	1
1.2. Objectives	8

## 2. Theoretical Background 10

2.1. Boundary Layer Separation	10
2.2. Analysis of Temporal Spatial Velocity	14
2.2.1. Velocity Decomposition	14
2.2.2. Temporal Turbulent Properties	16
2.2.3. Spatial Velocity Properties	17
2.2.4. Classic and Snapshot Proper Orthogonal Decomposition	19
2.3. Particle Image Velocimetry (PIV)	20
2.3.1. Camera and Imaging	22
2.3.2. Particles	27
2.3.3. Image Enhancement and Displacement Interrogation	28
2.3.4. Data Validation and Replacement	34

## 3. Experimental Setup 36

3.1. Laboratory Flume	36
3.2. PIV Measurement	40
3.3. Dimensional Analysis and Experimental Conditions	44

## 4. Results and Discussion 50

4.1. Flow Field Analysis	50
4.1.1. Velocity Statistics	50

4.1.2. Conditional Averaging .....	60
4.1.3. Snapshot Proper Orthogonal Decomposition .....	71
4.2. Analysis of Separation and Reattachment Point .....	79
<b>5. Conclusions .....</b>	<b>86</b>
<b>Reference .....</b>	<b>89</b>

## List of Tables

Table 3.1 Experimental Conditions upstream of the finite crested weir with a downstream ramp .....	47
Table 4.1 Statistics of the size of reverse flow. ....	62
Table 4.2 Normalized separation and reattachment points with experimental hydraulic parameters. ....	80

## List of Figures

Figure 1.1 Flow pattern around the finite crested weir with the downstream ramps; (a) Hydraulic Jump, (b) Plunging Jet (c) Surface Wave (d) Surface Jet.....	3
Figure 1.2 Streamlines upstream of the step under laminar flow, (a) two dimensional (b) three dimensional diagram drawn by Stürer et al. (1999). As out of plane motion is established shown in (b), separation flow upstream of the step is three dimensional flow. ....	6
Figure 1.3 Conceptual diagram of experimental setup (a) upstream of FFS (b) upstream of finite crested weir with the downstream ramp .....	7
Figure 2.1 Configuration of the field of view, a particle, lens, and video array on camera modified from Adrian (1991). ....	24
Figure 2.2. Valid detection of image displacement (Keane and Adrian, 1992). ....	32
Figure 3.1 (a) Top-view and (b) side view of the flume. ....	37
Figure 3.2 (a) Top-view and (b) side view of the test section. ....	38
Figure 3.3 Conceptual diagram of the experimental setup with field of view and coordination .....	39
Figure 3.4 Cross-section view of the test section (AA').....	41
Figure 3.5 PIV setup – Laser, optical table and platform, and synchronized camera .....	42
Figure 3.6 PIV reflection mirror. To obtain proper field of view, the mirror is fixed with 45° angle. ....	43
Figure 3.7 Temporal mean of raw PIV images upstream of the weir.....	45

Figure 3.8 Water surface profile for the experiments; (a):  $Q=20$  L/s (b):  $Q=10$  L/s. The line is drawn by mean PIV image, and the circle points are point measured data. The dot line over the weir is linearly interpolated between points. .... 46

Figure 3.9 Log-law fitting of measured velocity profile and estimated velocity profile to estimate boundary layer thickness ..... 49

Figure 4.1 Instantaneous streamwise velocity at 15-17th frame and white line is  $u=0$ . .... 51

Figure 4.2 Mean streamwise and vertical velocity field upstream of the weir normalized by the cross-section averaged velocity,  $U_1$ , with the streamlines calculated from mean velocity (case: Q20-HJ). .... 52

Figure 4.3 Mean streamwise velocity normalized by the cross-section averaged velocity,  $U_1$ , with the streamlines calculated from mean velocity field. .... 54

Figure 4.4 Mean vertical velocity normalized by the cross-section averaged velocity,  $U_1$ , with the streamlines calculated from mean velocity field. .... 55

Figure 4.5 Normalized RMS streamwise velocity ..... 57

Figure 4.6 Normalized RMS vertical velocity ..... 58

Figure 4.7 Normalized Reynolds stress ..... 59

Figure 4.8 PDF of the reverse flow area at instantaneous streamwise velocity ..... 63

Figure 4.9 CDF of the reverse flow area at instantaneous streamwise velocity ..... 64

Figure 4.10 Streamlines of 0 ~ 10 % reverse flow fields ..... 65

Figure 4.11 Streamlines of 90 ~ 100 % reverse flow fields ..... 66

Figure 4.12 Streamlines of the maximum five flow fields ..... 67

Figure 4.13 Streamlines of the first closed separation flow .....	69
Figure 4.14 Comparison of the separation points with area of reverse flow .....	70
Figure 4.15 Energy level of the POD modes .....	72
Figure 4.16 First SPOD mode of the streamwise fluctuation velocity .....	73
Figure 4.17 Second SPOD mode of the streamwise fluctuation velocity .....	74
Figure 4.18 First SPOD mode of the vertical fluctuation velocity .....	75
Figure 4.19 Second SPOD mode of the vertical fluctuation velocity .....	76
Figure 4.20 TKE and Reynolds stress of the (a) $N=5$ and (b) $N=20$ .....	78
Figure 4.21 Comparison of separation point derived by the mean zero shear stress and 50% fraction of time.....	82
Figure 4.22 Relationship between separation and reattachment points .....	82
Figure 4.23 Variation of the separation (a) and reattachment points (b) with $\mathbf{Re}_w$ .....	83
Figure 4.24 Variation of the separation (a) and reattachment points (b) with $\mathbf{Fr}$ .....	84
Figure 4.25 Variation of the separation (a) and reattachment points (b) with $h_1/h_w$ .....	85

## List of Symbols

### Latin Uppercase

$A_I$	Size of the interrogation window
$A_M$	Size of the main channel
$A_S$	Size of storage zone
$B$	Width of channel
$D_a$	Diameter of the lens aperture
$D_0$	Peak detectability
$F_O$	Probability of out-of-plane motion particle
$F_I$	Probability of in-plane motion particle
$I(\mathbf{X}, t)$	Image intensity of the particle located on $\mathbf{X}$ at time $t$
$I_{filt}[x, y, t]$	Filtered image
$I_m[x, y]$	Minimum valued image
$I_t$	Turbulence Intensity
$L_C$	Crest length
$L_{step}$	Step crest length
$M_0$	Constant magnification of the lens
$N_I$	Image density
$N_S$	Source density
$P$	Weir height
$Q$	Discharge
$R(\mathbf{s})$	Cross-correlation estimator
$R_C(\mathbf{s})$	Convolution of the mean intensities in $R(\mathbf{s})$

$R_D(\mathbf{s})$	Displacement correlation in $R(\mathbf{s})$
$R_F(\mathbf{s})$	Noise (fluctuation) components in $R(\mathbf{s})$
$Re$	Reynolds number based on water depth
$Re_p$	Particle Reynolds number
$Re_w$	Weir Reynolds number based on weir height
$\mathbf{S}$	Auto-covariance matrix of trajectory matrix $\mathbf{X}_t$
$U_e$	Free stream velocity
$U_1$	Oncoming cross-section averaged velocity
$U_k$	$k^{\text{th}}$ eigenvalue
$U_S$	Cross-section averaged velocity
$\bar{X}$	Temporal mean of $X$
$X'$	Fluctuation of $X$
$\mathbf{X}_p$	position of a particle in the image plane
$\mathbf{X}_t$	Trajectory matrix
$Z_0$	Image distance

### Latin Lowercase

$d_a$	Lens aberration diameter
$d_p$	Particle diameter in the fluid
$d_s$	Diffraction-limited spot diameter
$d_\tau$	Particle diameter in the image
$f$	Frequency
$f^\#$	$f$ -number of lens

$f_l$	focal length
$g(\mathbf{x}, t)$	Location of all particles in the field of view at time $t$
$h_{step}$	step height
$h_w$	Weir height
$h_1$	Upstream water depth
$h_2$	Downstream water depth
$k$	Turbulent Kinetic Energy
$p$	Pressure
$u$	Instantaneous velocity
$u_{rms}$	Root-mean-square of the fluctuation velocity
$u_{str}$	deterministic structured velocity
$\mathbf{v}_p$	velocity of the particle in the field of view
$w_{ij}$	Vorticity
$\mathbf{x}_p$	position of a particle in the field of view
$x_s$	Separation point
$y_s$	Reattachment point
$z_0$	Object distance

### Greek Uppercase

$\Delta^n$	$n$ th derivatives
$\Delta z_p$	Displacement of a particle during the image time gap

### Greek Lowercase

$\gamma_f$	Fraction of time
$\delta[x]$	Dirac-delta function
$\delta_z$	depth of field
$\delta_{99}$	99% boundary layer thickness
$\delta_1$	Displacement thickness
$\delta_2$	Momentum thickness
$\varepsilon$	Image exposure
$\epsilon_{ij}$	Strain tensor
$\hat{\epsilon}_C$	Centroid subpixel estimator
$\hat{\epsilon}_G$	Gaussian subpixel estimator
$\hat{\epsilon}_P$	Parabolic subpixel estimator
$\lambda_i$	$i^{\text{th}}$ eigenvalue
$\lambda_w$	Wavelength of scattered light through a bandpass filter
$\mu$	Dynamic viscosity
$\mu_X(t)$	Ensemble mean of $X$
$\rho_f$	Density of fluid
$\rho_p$	Density of particle
$\sigma_X$	Standard deviation of $X$
$\tau$	Shear stress
$\tau_p$	Particle time constant
$\tau_{ij}$	Reynolds stress
$\nu_f$	Kinematic viscosity of the fluid

# Chapter 1. Introduction

## 1.1. Research Background

Riverine weirs are widely constructed hydraulic structures in river systems for water-level elevation, flood control, and irrigation. Among various shapes of the riverine weirs, finite-crested weirs with vertical front wall and a downstream ramp were extensively installed due to simple design and convenience for construction. The downstream ramp prevents free flow that can negatively impact on the stability of hydraulic structures and downstream soil erosion (Chanson, 2000).

The flow in the vicinity of the finite crested weirs is extremely complex because of the combined effects of flow separation, sudden contraction and expansion, and pressure change. Upstream of the finite crested weir with a vertical front, the boundary-layer separation is established by the presence of adverse pressure gradient. This separation leads to a substantial increase in wall-to-normal velocity and enlargement of the rotational-flow region (Simpson, 1989; Pearson et al., 2013). Consequently, the recirculating flow is generated at the bottom upstream of the finite crested weir, and this flow plays a vital role in sediment transport, discharge capacity, and contaminant transport at the weirs (Jackson et al. 2013). In particular, the ascending and descending momentum of the recirculating flow could yield significant damage to the weirs as it entrains sediments at the base of the structure (Lauchlan, 2004; Azimi et al., 2013). Therefore, to mitigate the disadvantages produced by recirculating flow, the investigation of the boundary layer separation and its influence on flow characteristics upstream of the weir is essential.

Considerable studies on the flow characteristics around the finite crested weirs have been examined by laboratory and numerical experiments. Most of the studies are of interest in the head-discharge relationship (Gonzalez and Chanson, 2007; Azimi & Rajaratnam, 2009; Sargison & Percy, 2009; Azimi et al., 2013; Chen et al., 2018; Mahtabi & Arvanaghi, 2018), sediment transport (Lauchlan, 2004; Guan et al., 2014, 2016, Wang et al., 2017), and downstream flow pattern (Fritz & Hager, 1998; Hakim & Azimi, 2017). The downstream flow pattern can be categorized into four regimes (Fritz & Hager, 1998). The features of the four regimes shown in Figure 1.1 are

- 1) Hydraulic jump – Subcritical flow with the hydraulic jump. Upstream water depth is not altered by downstream flow.
- 2) Plunging jet – The main flow rapidly travels along the weirs surface and the downstream bed. Reverse flow is produced at the surface.
- 3) Surface wave – The main flow goes along the surface by generating the surface wave. Reverse flow is generated at the bottom.
- 4) Surface jet – The main flow travels along the surface, but the surface profile is almost horizontal. Reverse flow is developed at the bottom.

Therefore, the upstream water depth can be altered by the downstream flow pattern in spite of the same discharge.

The researches of separation flow around the finite crested weir were mainly focused on the flow over the weir. Moss (1972) suggested a simple model derived from the Laplace equation of the irrotational flow to explain the flow separation over the broad-crested weir. Hager &

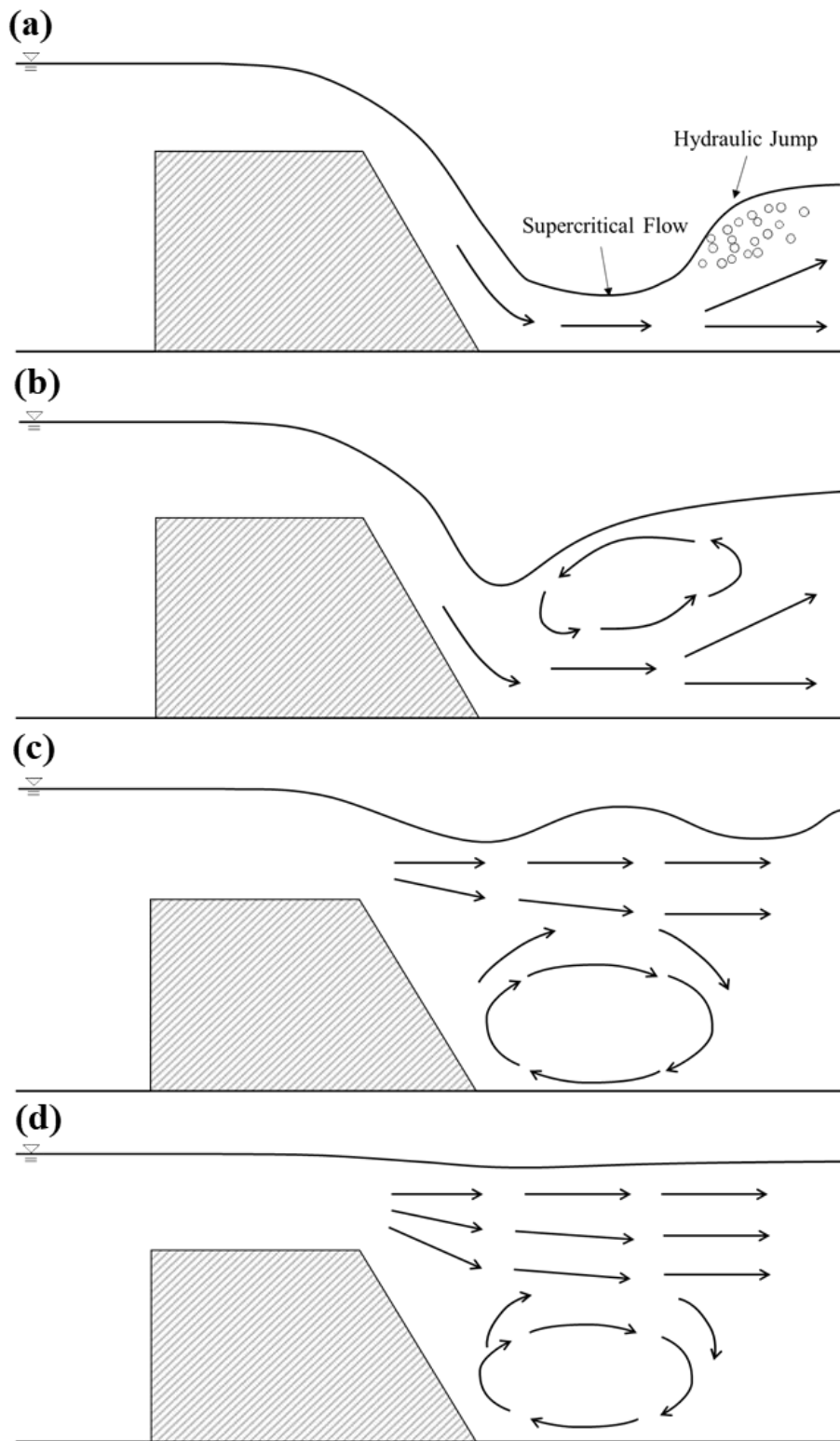


**Figure 1.1** Flow pattern around the finite crested weir with the downstream ramp: (a) Hydraulic Jump; (b) Plunging jet; (c) Surface wave; (d) Surface jet.

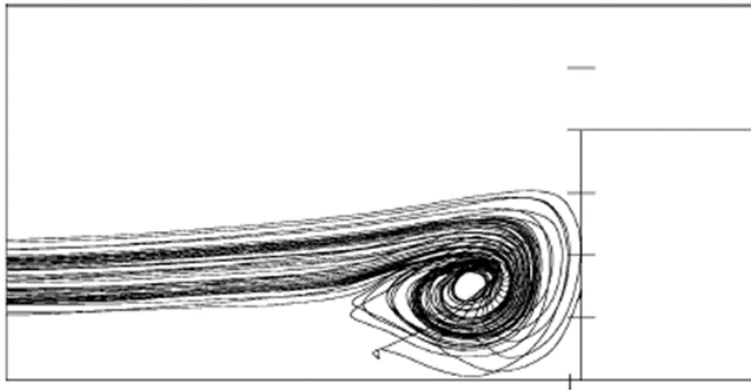
Schwalt (1994) showed the adverse pressure gradient and established separation profile over the finite crested weir by measuring the bottom pressure profile. Goodarzi et al. (2012) showed decreasing upstream slopes of the broad-crest weir induces the dissipation of the separation flow region at the upstream corner. Madadi et al. (2014) evaluated the length scale of flow separation area over the trapezoidal broad-crested weir with different upstream face slope by employing dye injection and particle tracking method. Although the previous researches demonstrated the characteristics of flow separation at the over the finite crested weir, flow separation produced upstream of the finite crested weirs has not been broadly investigated.

Similar researches on the flow separation are found at the topic of the forward facing step (FFS). FFS can be regarded as a bluff body in nature and engineering fields, and the flow separation with recirculating flow arises upstream and front edge of FFS. While studies on the flow separation around FFS have been extensively researched, a small number of published papers focus on the upstream region of FFS. Stüer et al. (1999) investigated laminar boundary layer separation upstream of FFS in an open water channel with constant water depth by implementing particle tracking velocimetry and the hydrogen bubble technique. They showed that the laminar recirculation upstream of FFS is an *open separation bubble* that the fluid is moved into a recirculating focus and then released. Furthermore, Stüer et al. found that separation flow upstream of the step is three dimensional flow due to out of plane motion shown in Figure 1.2. Leclercq (2001) demonstrated that eddies produced by upstream separation of FFS influence wall pressure field over the and create strong flow perturbations. In this experimental research conducted at the wind tunnel, the oncoming boundary layer thickness is lower than step height ( $\sim 0.7h_{step}$ ), and the location of upstream separation and vertical reattachment are approximately  $-0.8h_{step}$  and  $0.6h_{step}$ , respectively. Pearson et al. (2013) analyzed the structure and variation of the separation flow in the wind tunnel using the

conditional averaging method of the reverse flow area size. They showed that the ejections at the edge of FFS are generated by the convective motion of the upstream low-velocity regions. The location of upstream separation point lies between  $-0.8h_{step}$  to  $-1.2h_{step}$ .

Despite earlier findings upstream of FFS, however, there are a number of crucial experimental differences between flow upstream of FFS and the weir. The primary difference is the upper boundary of the system. As shown in Figure 1.2, which represents the conceptual configuration of the experimental setup upstream of FFS and the weir, the flow upstream of FFS is not bounded by the channel depth. However, the flow upstream of the weir is bounded by the upstream water depth, which is partially dependent on the downstream water depth. As a result, FFS has a region of free stream flow, which can be used to derive boundary layer thickness, but there is no apparent free stream region upstream of the weir. In addition, the boundary layer thickness of the weir is generally smaller than the height of the weir, but most of the researches upstream of FFS have larger boundary layer thickness (Pearson et al., 2013).

**(a)**



**(b)**

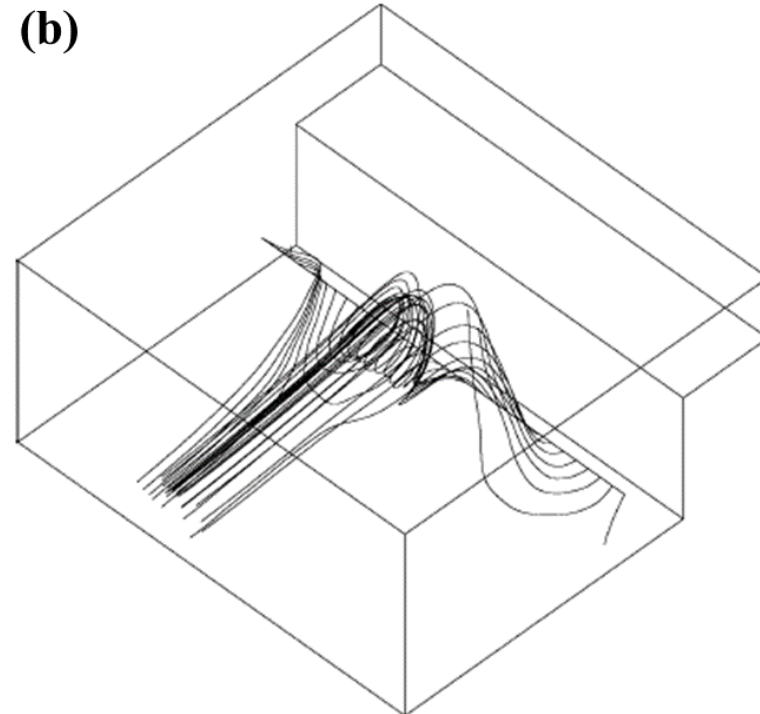


**Figure 1.2** Streamlines upstream of the step under laminar flow, (a) two dimensional (b) three dimensional diagram drawn by Stüer et al. (1999). As out of plane motion is established shown in (b), separation flow upstream of the step is three dimensional flow.

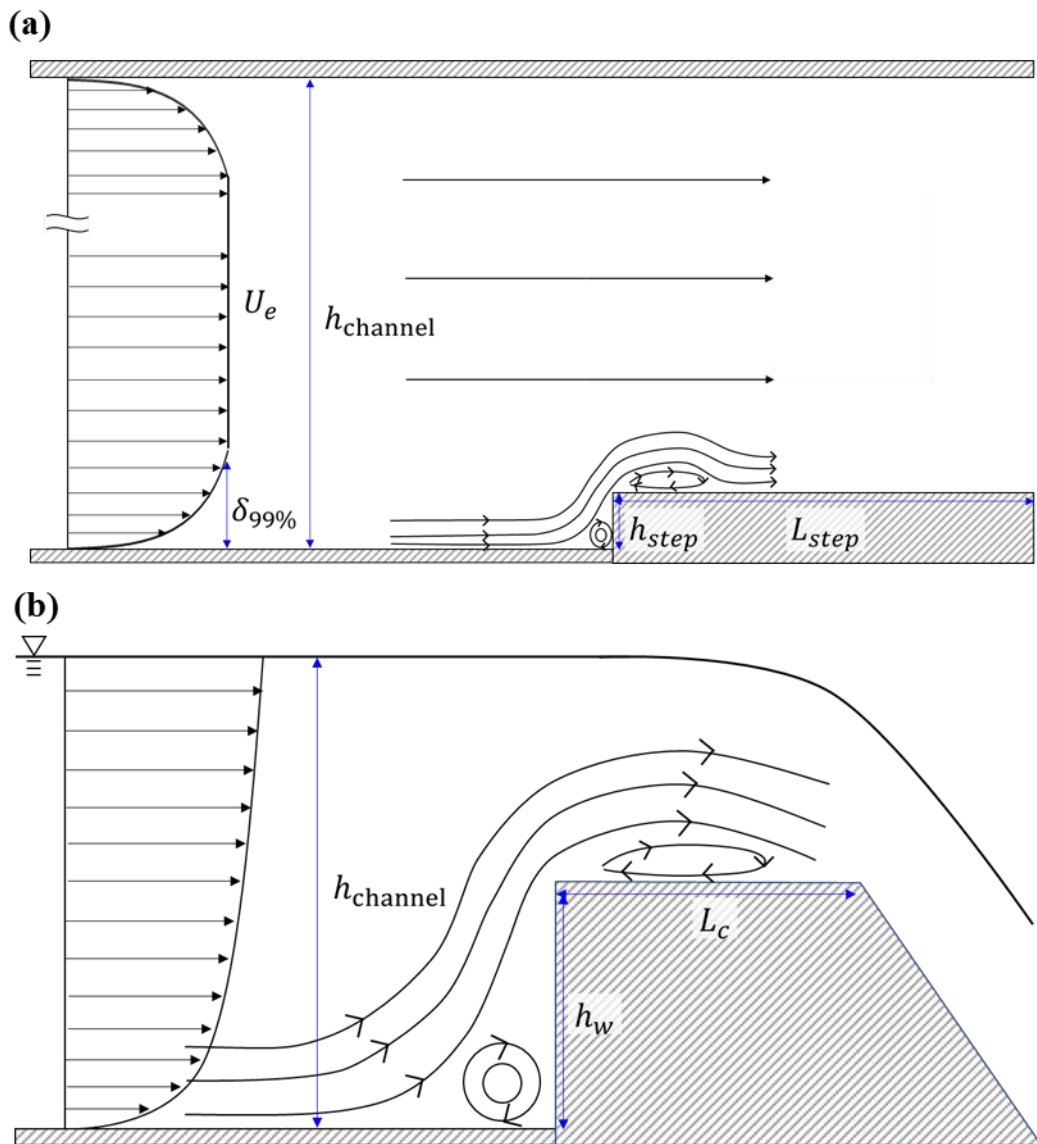


**Figure 1.3** Conceptual diagram of the experimental setup (a) upstream of FFS (b) upstream of the finite crested weir.

## 1.2. Objectives and Methodology

The main objectives of the research are to experimentally study the flow separation upstream of the finite crested weir with the downstream ramp for various upstream water depth by changing the downstream water depth. The research has two sub-objectives

### (1) **Flow structure**

To investigate the flow fields using the statistics of the temporal-spatial velocity and to estimate the deterministic flow structures.

### (2) **Separation and reattachment point**

To evaluate the separation and reattachment points using the methods of the mean zero shear stress and the fraction of time and to derive the relationship between the points and the nondimensional hydraulic parameters.

For the simulation of the flow pattern around the weir, the experimental conditions were decided taking account of the upstream-downstream water depth relationship. The two-dimensional standard Particle Image Velocimetry (PIV) was applied at the upstream bottom of the weir to calculate the instantaneous velocity fields. The image processing was carried out through the *PIVlab* in the Matlab software to evaluate temporal-spatial velocity fields.

The analysis of the size of reverse flow was conducted to estimate the intensity of the separation flow. The conditional averaging of the size was used to observe instances of similar flow fields. Streamlines and separation points with the size were investigated.

Flow characteristics and rotating motion were studied by the temporal-spatial data analysis

of velocity fields. The deterministic structures of the fluctuation velocity with corresponding energy were obtained by applying the Snapshot Proper Orthogonal Decomposition (SPOD).

The separation points were found at the location where the mean bed shear stress is zero, and the fraction of time is 50%. Furthermore, the vertical reattachment points were identified at the position where the mean vertical velocity changes its sign. The locations of separation and reattachment were researched with the nondimensional parameters.

## Chapter 2. Theoretical Background

### 2.1. Boundary Layer Separation.

Flow close to the solid boundary is explained by the boundary layer theory. The fundamental hypothesis of the theory, introduced by Ludwig Prandtl in 1905, is the forces of the minute viscous fluid are insignificant in all places except adjacent to the solid wall at which no-slip condition exists. For the outer layer where fluid viscosity is negligible, the flow is irrotational and the drag of the solid surface does not affect the flow significantly. For the boundary layer, however, the length scale of surface-to-normal direction is much smaller than other scales, including the length of the solid surface or its radius of curvature. In this layer, which can subsist only in the flow with high Reynolds number, the equation of motion can be simplified by applying the dimensional analysis. The velocity across the boundary layer alters rapidly enough for fluid viscosity to be of importance.

#### 1) Equations of motion at the boundary layer

The continuity and momentum equation of constant-viscosity constant-density fluid are:

$$\nabla \mathbf{u} = 0 \quad (2.1)$$

$$D\mathbf{u}/Dt = -(1/\rho)\nabla p + \nu\nabla^2\mathbf{u} \quad (2.2)$$

where  $\mathbf{u}$  is velocity,  $\rho$  is fluid density,  $p$  is pressure, and  $\nu$  is kinematic viscosity. For the boundary layer, the aforementioned assumptions (length scale, high Reynolds number) are satisfied and simplified equations of motion under laminar flow can be derived (details are described in chapter 9 of Kundu et al., 2012), those are:

$$\frac{\partial u}{\partial x} + \frac{\partial v}{\partial y} = 0 \quad (2.3)$$

$$u \frac{\partial u}{\partial x} + v \frac{\partial u}{\partial y} = -\frac{1}{\rho} \frac{\partial p}{\partial x} + \nu \frac{\partial^2 u}{\partial y^2} \quad (2.4)$$

$$0 = -\frac{\partial p}{\partial y} \quad (2.5)$$

Here,  $x$  and  $y$  is wall tangential and normal direction of a curvilinear coordinate system, and  $u$  and  $v$  are the corresponding directional velocity. The equation (2.5) shows that the pressure is constant across the boundary layer.

## 2) Boundary-Layer Thickness

Demarcating the exact location of the boundary layer is complicated because the boundary layer velocity profile meets the outer layer velocity profile. Therefore, several definitions of the boundary layer thickness are used to present the boundary layer's characteristics.

First of all, the boundary-layer thickness,  $\delta_{99}$ , is the distance from the wall where the streamwise velocity is  $0.99U_e$ , where  $U_e$  is the local streamwise velocity in the outer layer. Secondly, the displacement thickness,  $\delta_1$ , is the distance to the wall so that the integration of streamwise velocity from the wall to an upper limit of the outer layer is equal to that of streamwise velocity from  $\delta_1$  to the upper limit. This definition can be written by:

$$\int_0^h u(y) dy = \int_{\delta_1}^h U_e dy = U_e(h - \delta^*) \quad (2.6)$$

$$\delta_1 = \int_0^\infty \left(1 - \frac{u(y)}{U_e}\right) dy \quad (2.7)$$

In equation (2.7), the upper limit of the outer layer  $h$  goes to  $\infty$ . A third estimator is the momentum thickness  $\delta_2$ . It stems from the concept of the momentum loss produced by the presence of the boundary layer. The momentum thickness is described by:

$$\delta_2 = \int_0^\infty \frac{u(y)}{U_e} \left(1 - \frac{u(y)}{U_e}\right) dy \quad (2.8)$$

### 3) Separation

The separation, the breakdown of boundary layer flow, appears where the boundary layer moves under the adverse pressure gradients where the pressure increases following the flow direction. A fundamental explanation of the boundary-layer separation starts with the steady streamwise boundary layer flow under the pressure gradient is imposed on the boundary layer. Considering the boundary condition of solid wall where both velocity components are zero, the equation (2.4) reduces to

$$\frac{1}{\rho} \frac{\partial p}{\partial x} = \nu \left( \frac{\partial^2 u}{\partial y^2} \right)_{wall} \quad (2.9)$$

For an external decelerating flow, where  $\partial p / \partial x > 0$ , the curvature of velocity profile normal to the wall is

$$\nu \left( \frac{\partial^2 u}{\partial y^2} \right)_{wall} > 0 \quad (2.10)$$

This pressure gradient is stated as *adverse*.

As the boundary layer velocity profile smoothly meets the outer layer velocity profile, the curvature of velocity profile changes its sign inside the boundary layer. In short, a point of

inflection,  $\partial^2 u / \partial y^2 = 0$ , is found in the boundary-layer profile in the adverse pressure gradient. In the strong adverse pressure gradient, the flow close to the wall reverse its direction. When the reserve flow meets the forward flow, the local flow is stagnated, and this point is called *separation point*. In the separation point, approaching fluid elements arise from the wall, and the shear stress change sign at this point since the direction of the surface flow is changed. Therefore, the location of the separation point can be found by averaging wall shear stress;

$$\langle \tau_{wall} \rangle = \langle \mu \left( \frac{\partial u}{\partial y} \right)_{wall} \rangle = 0 \text{ (separation point)} \quad (2.11)$$

Downstream of the separation point, a region of rotational flow and the wall-to-normal velocity increase substantially.

Another method proposed by Simpson (1989) to estimate the region of separation is the *fraction of time* that the flow travels downstream,  $\gamma_f$ . There are three estimators, those are

Incipient detachment (ID):  $\gamma_f = 99\%$

Intermittent transitory detachment (ITD):  $\gamma_f = 80\%$

Transitory detachment (TD):  $\gamma_f = 50\%$ .

Practically, the positions of  $\gamma_f = 0.5$  and  $\langle \tau_{wall} \rangle = 0$  are often closely located (Na & Moin, 1998)

## 2.2. Analysis of Temporal-Spatial Velocity

### 2.2.1. Velocity Decomposition

#### **Reynolds Decomposition**

The instantaneous velocity at each point is decomposed into a temporal mean and fluctuation, that is described by

$$u(\mathbf{x}, t) = \bar{U}(\mathbf{x}) + u'(\mathbf{x}, t) \quad (2.12)$$

where  $\bar{U}$  is the temporal mean, defined by

$$\bar{U}(\mathbf{x}) = \lim_{T \rightarrow \infty} \frac{1}{T} \int_0^T u(\mathbf{x}, t) dt. \quad (2.13)$$

For discrete time-series, it can be rewritten by

$$\bar{U}(\mathbf{x}) = \lim_{N \rightarrow \infty} \frac{1}{N} \sum_{n=1}^N u[\mathbf{x}, n] \quad (2.14)$$

Turbulent characteristics, including turbulent kinetic energy (TKE), turbulence intensity (TI), and Reynolds stress, are estimated by analyzing the statistical properties of  $u'(\mathbf{x}, t)$  (details are in 2.2.2).

#### **Triple Decomposition**

If the flow has a coherent structure such as Von Karman vortex, however, the turbulent characteristics can be overestimated, when conventional Reynolds decomposition is employed. In this case, it is necessary to apply triple decomposition. The triple decomposition divides the

instantaneous velocity into the temporal mean, structured velocity, and fluctuation. It is described by

$$u(\mathbf{x}, t) = \bar{U}(\mathbf{x}) + u_{str}(\mathbf{x}, t) + u'(\mathbf{x}, t) \quad (2.15)$$

where  $u_{str}(t)$  is deterministic structured velocity component. For temporal-spatial data, the proper orthogonal decomposition is used to derive structured velocity (details are in 2.3.2).

### 2.2.2. Temporal Turbulence Properties

Temporal turbulent properties are evaluated by statistical times series investigating of the fluctuation velocity derived by the Reynolds decomposition or triple decomposition. the Turbulent Kinetic Energy (TKE),  $k$ , is defined by temporal averaging of the fluctuation velocity components, written by

$$k = \frac{1}{2} \langle u_x'^2 + u_y'^2 + u_z'^2 \rangle. \quad (2.16)$$

In addition, the turbulent intensity,  $I_t$ , which non-dimensionally presents the relative unsteadiness of the fluctuation velocity components against the mean flow, is defined as

$$I_t = \frac{u_{rms}}{U_s} \quad (2.17)$$

where  $u_{rms}$  is the root-mean-square of the fluctuation velocity, that is

$$u_{rms} = \sqrt{\langle u_x'^2 \rangle} \quad (2.18)$$

and  $U_s$  is the cross-section averaged velocity calculated from the discharge and channel area that is

$$U_s = Q/Area. \quad (2.19)$$

At last, Reynolds stress components which have the dimensions of velocity square is the temporal average of the product of two fluctuating velocities, defined by

$$\tau_{ij} = \langle u_i' u_j' \rangle \quad (2.20)$$

### 2.2.3. Spatial Velocity Properties

Two-dimensional instantaneous velocity fields are obtained from the PIV process. Consequently, it is possible to apply the aforementioned temporal analysis to the spatial data. However, the most significant merits of spatial data analysis are to acquire velocity derivatives, which cannot be inferred from the point temporal data such as time series measured by ADV.

The derivative tensor is calculated from the spatial velocity field by

$$\frac{\partial u_i}{\partial x_j} = \frac{u(i+1) - u(i-1)}{2dx_j} \quad (2.21)$$

where  $dx_j$  is the distance between adjacent spatial data. The derivatives can be divided into symmetric and antisymmetric components. The symmetric component is the strain tensor, that is

$$\epsilon_{ij} = \frac{\partial u_i}{\partial x_j} + \frac{\partial u_j}{\partial x_i}. \quad (2.22)$$

On the contrary, the antisymmetric component is the vorticity vector defined as the curl of the velocity field

$$w_{ij} = \frac{\partial u_j}{\partial x_i} - \frac{\partial u_i}{\partial x_j}. \quad (2.23)$$

Based on the Reynolds decomposition or triple decomposition, mean strain tensor and vorticity are defined by

$$\bar{\epsilon}_{ij} = \frac{\partial \bar{u}_i}{\partial x_j} + \frac{\partial \bar{u}_j}{\partial x_i} \quad (2.24)$$

$$\bar{w}_{ij} = \frac{\partial \bar{u}_j}{\partial x_i} - \frac{\partial \bar{u}_i}{\partial x_j}. \quad (2.25)$$

Fluctuation strain tensor and vorticity are also written by

$$\epsilon'_{ij} = \frac{\partial u'_i}{\partial x_j} + \frac{\partial u'_j}{\partial x_i}. \quad (2.26)$$

$$w'_{ij} = \frac{\partial u'_j}{\partial x_i} - \frac{\partial u'_i}{\partial x_j}. \quad (2.27)$$

#### 2.2.4. Classic and Snapshot Proper Orthogonal Decomposition (SPOD)

The Proper Orthogonal Decomposition (POD) is a famous mathematical procedure to break down the data into a sum of components. This approach has been used for detecting dominant structures or removing noise.

Two different forms of POD are classic POD and snapshot POD, but both share the same theoretical background (Hilberg et al. 1994). Mathematical descriptions of the POD method employed here are based on Glezer et al. (1989). Suppose  $u'$  is fluctuation velocity measured at  $M$ -points in space simultaneously and at  $N$ -times. the time series matrix  $A$  having columns  $a^{(i)}$  is defined by

$$A = u'_{ij} \quad 1 \leq i \leq M, 1 \leq j \leq N \quad (2.28)$$

$$a^{(i)} = (u'_{i1}, u'_{i2}, \dots, u'_{iN}) \quad 1 \leq i \leq M \quad (2.29)$$

Similar to the SSA method, eigenvalue decomposition is applied for the classic POD, that is

$$\Psi U_k = (A^T A) U_k = \lambda_k U_k \quad 1 \leq k \leq N. \quad (2.30)$$

where,  $\Psi$  is spatial covariance matrix,  $\lambda_k$  is  $k$ th eigenvalue, and  $U_k$  is corresponding  $k$ th eigenvector . The equivalent flow field by the classic POD is evaluated by

$$a_t^{(k)} = A U_k \quad (2.31)$$

$$(u')^{(k)} = a_t^{(k)} U_k \quad (2.32)$$

In a modified matrix, columns match to instantaneous ‘snapshot’ of the flow field.

### 2.3. Particle Image Velocimetry (PIV)

PIV is a flow-field measurement system for experimental fluid mechanics. PIV measures the instantaneous global velocity field by calculating the displacement of the particles, which precisely accompany the fluid movement, in the captured images. PIV has been widely employed in fluid mechanics because it has numerous superiorities compared to conventional measurement devices. One of the merits of PIV relies on conceptual simplicity. PIV uses the basic definition of velocity, which is calculated from displacement and time increment.

On the other hand, other devices indirectly evaluate velocity by using intermediate physics. For example, acoustic Doppler velocimetry and laser Doppler velocimetry estimate velocity from the Doppler shift that has to do with the velocity of the particle. Likewise, thermal anemometers deduce velocity from the electrical measurement of the heat transfer of the sensor located in the fluid (Bruun, 1996). Secondly, since any components of the PIV system do not intrude on the flow, the unaltered velocity field can be measured. Finally, PIV uses the particles as markers of the motion of the fluid. Particles generally do not deform or diffuse in the fluid motion. They are ubiquitous in the fluid and scatter much more light in comparison with molecules.

Although the principle of PIV is simple, factors that affect the credibility of PIV results are numerous. Therefore, understanding the factors is needed to achieve accurate and reliable results. In this subchapter, a brief but comprehensive description of the factors in standard planar PIV is represented. Further information and other PIV measurement schemes are written in Adrian and Westerweel (2011) and Raffel et al. (2018).

Standard Planar PIV is comprised of a double-pulsed laser, light-scattering optics, a single-lens camera, image digitization hardware, a computer for data storage, and particle seedings.

The double-pulsed laser is the standard in the PIV system on account of the expense in applying more than two pulsed-laser devices. The solid-state Nd: YAG lasers have been widely applied because that it can produce enough intensity of light for visualizing images of the particles. The light scattering optics have a deflecting mirror and spreading lens in general. The light beam is emitted from the pulsed laser and then deflected to the right-angle direction by the mirror. The diverted beam is scattered after it passes the lens, and the light sheet with little depth is made.

Numerous particles in the light sheet scatter the beam, and the camera synchronized with the double-pulsed laser by the synchronizer captures the scattered light. The specific wavelength bandpass filter is mounted on the camera to filter the other wavelength band. 532 nm bandpass filter is usually used with a Nd: YAG pulsed laser. The image digitization hardware produces digital images, and they are stored in the computer. Lastly, the 2-D flow-field is generated by image processing. Pre-processing, displacement estimation, and post-processing are typically implemented in this image processing.

### 2.3.1. Camera and Imaging

The configuration of the camera and the light sheet in Figure 2.5 enables one to identify the position of the  $p$ th particle in the fluid,  $\mathbf{x}_p(t)$ , with respect to its location on the camera sensor,  $\mathbf{X}_p(t)$ . The position of the  $p$ th particle in the image is determined by simple geometry between the image plane and the *field of view*, that is

$$\begin{pmatrix} X_p \\ Y_p \end{pmatrix} = M_0 \begin{pmatrix} x_p \\ y_p \end{pmatrix} \quad (2.32)$$

where

$$M_0 = Z_0/z_0 \quad (2.33)$$

is a constant magnification of the lens,  $z_0$  is the *object distance* from the lens effective center to the  $z = 0$  plane in the light sheet, and  $Z_0$  is the *image distance* from the image plane to the effective center of the lens (Adrian and Westerweel, 2011). This relationship is fit for *well-focused* condition where all other light emitting from the sheet are refracted by the lens so that they converge to corresponding points on the image plane. This condition is the *Gauss lens law*

$$\frac{1}{Z_0} + \frac{1}{z_0} = \frac{1}{f_l} \quad (2.34)$$

where  $f_l$  is the focal length of the lens.

When the laser pulses the light sheet at  $t$  and  $t + \Delta t$  with well-focused configuration, scattered light from the particles in the sheet generates in-focus points on the image plane. The displacement of the particles in the field of view is evaluated by

$$\begin{aligned} (v_x, v_y) &\cong \frac{(\Delta x, \Delta y)}{\Delta t} \\ &= \frac{(\Delta X, \Delta Y)}{M_0 \Delta t} \end{aligned} \quad (2.35)$$

where  $v_x$  and  $v_y$  are the velocity of each particle in the field of view along the direction in Figure 2.1. In this equation, the time gap,  $\Delta t$ , is small enough for the particles to accurately follow the linear relationship.

The aforementioned descriptions, though, oversimplify the actual mechanism for several reasons. At first, it neglects the volume of the particle so that it is assumed the particle is located on the  $z = 0$  plane. In reality, however, the light sheet has a thickness,  $\Delta z_0$ , and all particles located and semi-located (some portion of the particles reside) in the  $\Delta z_0$  scatter the light. Second, there are in-plane and out of plane motion in the field of view. As some particles travel out in the field of view plane (in-plane motion), or out to the normal direction to the plane (out of plane motion), a portion of the signal in the image made from scattered light is lost.

Moreover, the diameter of the image is influenced by not only the diameter of the particle,  $d_p$ , but also diffraction by lens and lens aberration. The diameter is approximately evaluated by

$$d_\tau \cong (M_0^2 d_p^2 + d_s^2 + d_a^2)^{\frac{1}{2}} \quad (2.36)$$

where

$$d_s = 2.44(1 + M_0)f^\# \lambda_w \quad (2.37)$$

is the *diffraction-limited spot diameter*, and  $f^\#$  is  $f$ -number of the lens defined by

$$f^\# = f/D_a \quad (2.38)$$

$D_a$  is the diameter of the lens aperture,  $\lambda_w$  is the wavelength of the scattered light passing through the bandpass filter, and  $d_a$  is the diameter of the aberrant image of a point source (Adrian and Westerweel, 2011). The Diffraction-limited spot diameter stems from the point response function of a diffraction-limited lens, which is estimated by the first dark ring of the

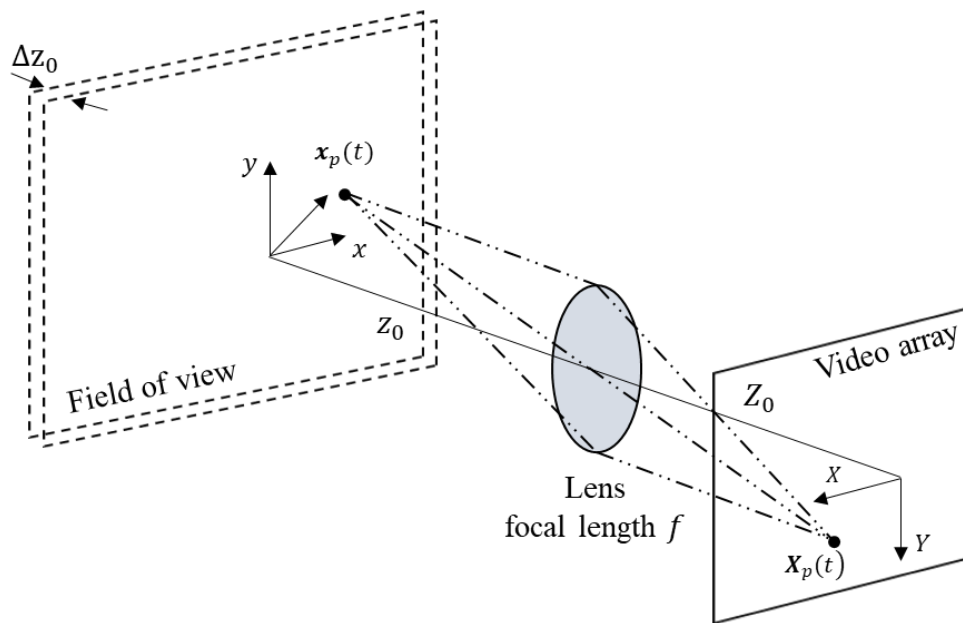


**Figure 2.1** Configuration of the field of view, a particle, lens, and video array on camera modified from Adrian (1991).

Airy disk intensity distribution (Adrian and Yao, 1985). Hence, even a tiny portion of the particles in the field of view plane can create a finite-diameter spot in the image owing to diffraction. In other words, the diameter of the particle in the image is almost independent of the  $z$  direction of the field of view when the diameter is predominated by the diffraction. This is fulfilled if the particles in the field of view are located in the range of  $z$  direction called *depth of field*, which is defined by

$$\delta_z \cong 4 \left(1 + \frac{1}{M_0}\right) f^{\#2} \lambda. \quad (2.39)$$

By choosing the appropriate value of  $M_0$  and  $f^\#$ , all particles inside the light sheet form the focused image. As a result, the equation (11) is altered by

$$\begin{pmatrix} \Delta X \\ \Delta Y \end{pmatrix} = M(z_p) \begin{pmatrix} \Delta x \\ \Delta y \end{pmatrix} + M(z_p) \begin{pmatrix} x/z_0 \\ y/z_0 \end{pmatrix} \Delta z_p \quad (2.40)$$

where  $M(z_p)$  is the modified magnification described as

$$M(z_p) = Z_0 / (z_0 - z_p), \quad (2.41)$$

$z_p$  is the particle location in the thickness of the field of view, and  $\Delta z_p$  is the displacement of particle during  $\Delta t$ . One solution to this issue in the planar PIV system is measuring the flows that have insignificant  $z$ -directional velocity. Therefore, for the experiments which measure the weak out-of-plane flows, one can approximate the equation (2.40) to (2.32).

## Particle Imaging

The recording left on the image pixel is fixed by the *exposure* of the image, that is defined by the integral of the light intensity over the time that the surface of the image sensor is exposed to the scattered light. If the position of the particle is explained by  $\mathbf{X} = \mathbf{F}(\mathbf{x})$ .

The image exposure,  $\varepsilon$ , from the scattered light of the particle is

$$\varepsilon = \int I(\mathbf{X}, t) dt = \psi(z) \delta t \tau_0 [\mathbf{X} - \mathbf{F}(\mathbf{x})] \quad (2.42)$$

where  $I(\mathbf{X}, t)$  is the image intensity of the particle,  $\tau_0(\mathbf{X})$  is the spatial-intensity distribution of a particle image per unit of illuminating intensity  $\psi(z)$ , and  $\delta t$  is the width of the light pulse (Adrian & Yao, 1985).

For the multiple well-focused particles which are a uniform size, the entire intensity is

$$I(\mathbf{X}, t) = \int \psi(z) \tau_0[\mathbf{X} - \mathbf{F}(\mathbf{x})] g(\mathbf{x}, t) d\mathbf{x} \quad (2.43)$$

where

$$g(\mathbf{x}, t) = \sum_{\forall p} \delta[\mathbf{x} - \mathbf{x}_p(t)] \quad (2.44)$$

presents the location of all particles in the field of view by the Dirac-delta function.

### 2.3.2. Particles

For visualizing the flow precisely, the suitable particles are seeded in the fluid. One of the merits of using the particles is that they function as markers of the fluid at many points, since they produce stronger optical images, follow the fluid movement, and do not diffuse or deform during the experiments. To correctly measure the flow motion, the size of the particles needs to be small to follow the fluid motion, but large to scatter the light from the laser to make bright images.

Nevertheless, the disadvantage of using the particles as markers is that they practically do not follow the fluid movement. Furthermore, there is a discrepancy since the velocity of the volume is derived from that of particles in the volume (Adrian 1991). The simple particle dynamics equation is

$$\dot{\mathbf{v}}_p \approx [\mathbf{u} - \mathbf{v}_p]/\tau_p + \mathbf{g} \quad (2.45)$$

where  $\mathbf{v}_p$  is the velocity of the particle in the volume,  $\mathbf{u}$  is volumetric velocity,  $\mathbf{g}$  is gravity, and  $\tau_p$  is the particle time constant given by

$$\tau_p = (\rho_p - \rho_f)d_p^2/18\rho_f\nu_f\phi_{Re}. \quad (2.46)$$

Where  $\rho_p$  and  $\rho_f$  is the density of particle and fluid, respectively,  $\nu_f$  is the kinematic viscosity of the fluid, and  $\phi_{Re}$  is the function determine by particle Reynolds number  $Re_p = |\mathbf{u} - \mathbf{v}_p|d_p/\nu_f$

The aforementioned complex equations can be ignored when the particles are neutrally buoyant ( $\rho_p \approx \rho_f$ ). 5-30  $\mu\text{m}$  hollow glass spheres or aluminum oxide, which have high-refractive-index, are typically used in water experiments.

### 2.3.3. Image Enhancement and Displacement Interrogation

Before estimating displacement, images are preprocessed to improve their quality. The ideal image has bright particles on the entirely dark background, and statistical properties of the particle intensity are uniform. However, due to several reasons, ideal images cannot be obtained. For example, light reflected by the wall of the flume or by the obstacle located in the flume can be captured in the image. Furthermore, the statistical properties of the particle intensity can be irregular when illumination is non-uniform. As a result, removing undesired effects on the image is required. In order to solve this problem, image filtering techniques are used. This process is generally called as *image enhancement*. The aim of the image enhancement is to visualize the particles more clearly and to diminish unwanted background image. Though there are a considerable number of image enhancement processes, the minimum time series filter in each pixel is described.

At first, the minimum valued image on each pixel is made by

$$I_m[x, y] = \min_{\forall t} I[x, y, t] \quad (2.47)$$

where  $I_m[x, y]$  is the minimum valued image on the specific position, and  $I[x, y, t]$  presents the intensity of the image on  $[x, y]$  position at time  $t$ . After the minimum valued image is obtained, a filtered image at the time  $t$ ,  $I_{filt}[x, y, t]$ , is composed by

$$I_{filt}[x, y, t] = I[x, y, t] - I_m[x, y]. \quad (2.48)$$

The minimum time series filter can advance the image quality by cutting out the unwanted images (e.g., wall reflection, dirt), which have relatively uniform intensity distribution during the measurement time.

The displacement interrogation is the image analysis step that automatically quantifies image displacement  $\Delta X$  over the entire field of view. The process depends on the density of the particles. It is determined by the source density  $N_s$  given by

$$N_s = C\Delta z_0 \frac{\pi d_p^2}{4M_0^2} \quad (2.49)$$

where  $C$  is the average number of particles per unit volume ( $\text{m}^3$ ). For the low particle density flows ( $N_s \ll 1$ ), Particle Tracking Velocimetry (PTV) is used where the displacement is measured by tracking individual particles. Since PTV efficiently operates when the particle is sparse, the number of PTV vectors is usually scant. Moreover, the displacement vectors related to the individual particles randomly reside. To solve this problem, therefore, more particles are added in the field of view.

For the high particle density flows without displaying speckle pattern, Particle Image Velocimetry (PIV) is used. The speckle pattern is the overlapped image produced by the mutual interference of scattered light from the particles. Particle image patterns in the two subsequent interrogation windows, which is a unit area of the image for the displacement interrogation, are matched to detect the image displacement. The *image density*,  $N_I$ , in the interrogation window is defined by

$$N_I \equiv CA_I\Delta z_0/M_0^2 \quad (2.50)$$

where  $A_I (= D_{Ix} \times D_{Iy})$  is the size of the interrogation window. It represents the number of particle image on the interrogation window. For the adequate application of PIV scheme, enough number of particle images are needed, that is  $N_I \gg 1$ .

The most general procedure is to execute Spatial-time cross-correlation of the images in the two ensuing interrogation windows. Assume that the images at time  $t$  and  $t + \Delta t$  are recorded from the scattered light of the particles in the field of view. They are written by

$$I_1(\mathbf{X}) = I(\mathbf{X}, t) = \int \psi(z) \tau_0[\mathbf{X} - \mathbf{F}(\mathbf{x})]g(\mathbf{x} - \mathbf{x}(t))d\mathbf{x}, \quad (2.51)$$

and

$$I_2(\mathbf{X}) = I(\mathbf{X}, t + \Delta t) = \int \psi(z) \tau_0[\mathbf{X} - \mathbf{F}(\mathbf{x})]g(\mathbf{x} - \mathbf{x}(t + \Delta t))d\mathbf{x}. \quad (2.52)$$

This is called *double-pulsed, double-frame recording*, which is two separate images are captured individually from double-pulsed light. The Spatial-time cross-correlation method is to find the location where maximum cross-correlation value exists, that is

$$\mathbf{x} = \arg \max R(\mathbf{s}) \quad (2.53)$$

where  $R(\mathbf{s})$  is cross-correlation estimator for an interrogation window,  $W$ , given by

$$R(\mathbf{s}) = \int_W I_1(\mathbf{X})I_2(\mathbf{X} + \mathbf{s})d\mathbf{X}. \quad (2.54)$$

Several factors can deteriorate the performance of the cross-correlation estimator. To begin with, unfiltered images can impair the performance of the estimator. Assuming that the captured image is comprised of the actual signal and noise, the cross-correlation is split into

$$R(\mathbf{s}) = R_C(\mathbf{s}) + R_D(\mathbf{s}) + R_F(\mathbf{s}) \quad (2.55)$$

where  $R_C$  is the convolution of the mean intensities,  $R_F$  is the noise component, and  $R_D$  is the displacement correlation. To improve the quality of the estimator, Therefore, the image enhancement is employed prior to the displacement interrogation.

Secondly, loss of the particle by in-plane and/or out-of-plane motion leads to the signal lose since each particle image has a unique pattern, i.e., a portion of the particle in  $I_1(\mathbf{X})$  does not

locate in  $I_2(\mathbf{X})$ . One method to solve the issue from the out-of-plane motion is to choose suitable  $\Delta t$ . If the flow has an out-of-plane velocity  $w$ , the probability of one particle remaining in the light sheet  $F_o$  is

$$F_o \left( \frac{w\Delta t}{\Delta z_0} \right) = \begin{cases} 1 - \left| \frac{w\Delta t}{\Delta z_0} \right| & |w\Delta t| < \Delta z_0 \\ 0 & \text{elsewhere} \end{cases} \quad (2.56)$$

A general guideline proposed by Adrian and Yao (1984), called “*one-quarter rule*”, is to restrict  $\Delta t$  by

$$|w|_{max} \Delta t / \Delta z_0 < 0.25 \quad (2.57)$$

whereby ensuring that less than one-quarter of the particles are unable to generate two images.

Similar criteria can be implemented to the solution of the in-plane loss  $F_I$ , that is

$$1 - F_I < 0.25. \quad (2.58)$$

In contrast to the solution of the out-of-plane loss, the in-plane loss can be mitigated by moving the second window to capture the entire particles in the first window.

## PIV Performance Validation

one of the most critical non-dimensional parameters for successful PIV measurement is the product

$$N_I F_I \left( \frac{|\Delta \mathbf{X}|}{D_I} \right) F_o \left( \frac{w\Delta t}{\Delta z_0} \right)$$

which expresses the average number of paired particles in the interrogation windows at  $t$  and  $t + \Delta t$ . If the size of the two windows is relatively large compared to the image displacement, that is  $D_I \gg \Delta \mathbf{X}$  and the second window is adequately shifted to enclose all the particles in the

first window,  $F_I$  is approximately assumed 1. Figure 2.6 shows the probability of valid detection depending on in-plane and out-of-plane motion, interrogation window size, and image density. It is the results of Monte Carlo simulations of random particles performed by Keane and Adrian (1992). The probability approaches 1 when the  $N_I F_I F_O$  is between 5 and 10.

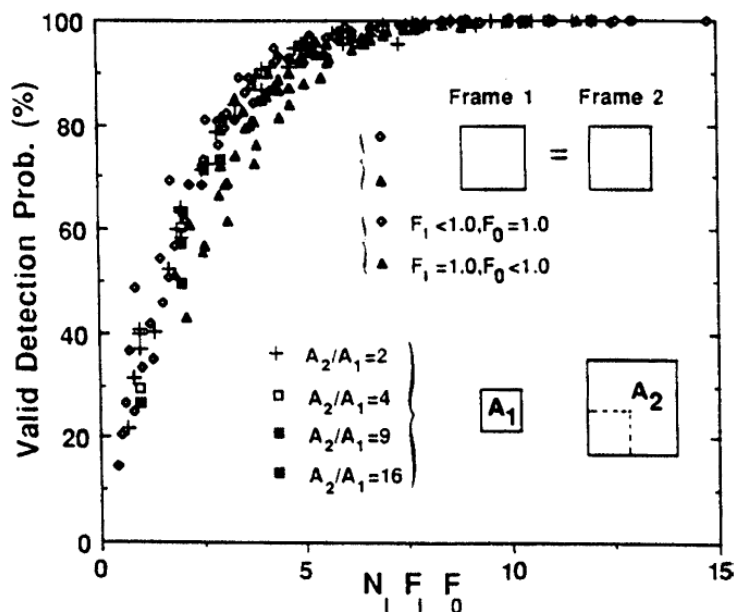


**Figure 2.2.** Valid detection of image displacement (Keane and Adrian, 1992).

## Subpixel Interpolation

The displacement estimated by the location of the correlation peak between the two windows is an integer. The actual image displacement can be described by

$$\mathbf{s}_D = \begin{pmatrix} m_0 + \epsilon_x \\ n_0 + \epsilon_y \end{pmatrix} \quad -\frac{1}{2} < \epsilon_x, \epsilon_y \leq \frac{1}{2} \quad (2.59)$$

where  $m_0$  and  $n_0$  are the *nearest-integer displacement* derived from the location of the correlation peak, and  $\epsilon_x$  and  $\epsilon_y$  are the fractional displacements. *Three-point estimators* are

used for assessing the fractional displacements. The theoretical background of the three-point estimators relies on the fact that the location of the actual peak is inferred from the correlation values around the integer location of the tallest peak. The simplified notation is applied

$$R_m^* = R_D^*[m_0 + m, n_0] \quad (2.60)$$

where  $m = -1, 0, 1$ , and  $R_D^*[m_0, n_0] = R_m^*$  is the location of the tallest correlation peak. Three different widely used methods are introduced here

### Centroid

$$\hat{\epsilon}_C = \frac{R_{+1}^* - R_{-1}^*}{R_{+1}^* + R_0^* + R_{-1}^*} \quad (2.61)$$

### Parabolic

$$\hat{\epsilon}_P = \frac{R_{-1}^* - R_{+1}^*}{2(R_{-1}^* + R_{+1}^* - 2R_0^*)} \quad (2.62)$$

### Gaussian

$$\hat{\epsilon}_G = \frac{\ln R_{-1}^* - \ln R_{+1}^*}{2(\ln R_{-1}^* + \ln R_{+1}^* - 2 \ln R_0^*)} \quad (2.63)$$

Among them, Gaussian estimator is widely used since it takes into account the concept of the correlation peak, and the shape of the displacement correlation peak. Hence, it can be assumed that the Gaussian fit yields the best results and shows smallest random and biased errors (Adrian and Westerweel, 2011).

### 2.3.4. Data Validation and Replacement

Raw PIV results have numerous vectors which are not similar to neighbor vectors. These vectors are called a *spurious vector*. It is because the actual peak is not equal to global peak so that random correlation peak yields the displacement. This phenomenon is dominant when the high turbulent flow is made where strong in-plane and out-of-plane motion exist. Although the intensity of turbulence is weak, it is difficult to prevent the spurious vectors. Therefore, suitable methods to detect the spurious vectors and to replace them are essential.

One of the approaches to reduce the number of the spurious vectors is to optimize the interrogation window, for instance, by increasing seeding concentration or the size of the interrogation window. Nevertheless, these methods produce undesired effects. Seeding more particles may change the fluid transparency or generate speckle pattern. Furthermore, the spatial resolution decreases when the interrogation window size increases. Alternatively, a different process is used where a small fraction of the spurious vectors is allowable. Generally, 5% of spurious data is regarded as “small fraction”.

#### **Peak Detectability**

This method is to compare the tallest correlation peak to the second tallest correlation peak. It is defined by the *peak detectability*, that is

$$D_0 = \frac{\text{tallest correlation peak}}{\text{second tallest correlation peak}}. \quad (2.64)$$

$D_0 \gg 1$  reflects that the correlation peak is significantly taller than the other peaks. This indicates that two subsequent interrogation windows are well-matched. Using the peak

detectability is reliable when the image density is large, but it fails to make credible results when the image density is low.

### Median Test

It is based on a local statistical approach that each vector is contrasted with the local median displacement of adjacent displacement vectors. The residual, or absolute deviation, of a calculated displacement  $\mathbf{s}_0$  with regard to the local median and standard deviation of adjoining vectors is described by

$$r = |\mathbf{s}_0 - \mathbf{s}_m|/\sigma_s \quad (2.65)$$

where  $\mathbf{s}_m$  is the local median displacement, and  $\sigma_s$  is the local standard deviation.  $3 \times 3$  or  $5 \times 5$  neighbor vectors are used to compute  $\mathbf{s}_m$  and  $\sigma_s$ . In conclusion, if the vectors are considered as *spurious* by means of the peak detectability or median test, they are replaced.

The simplest method of the replacement is to employ a linear interpolation of the adjoining vectors, that is

$$u_{i,j} = \frac{1}{2}(u_{i+1,j} + u_{i-1,j}) \quad v_{i,j} = \frac{1}{2}(v_{i,j-1} + v_{i,j+1}). \quad (2.66)$$

Since this method satisfies the continuity equation, it is physically valid.

## Chapter 3. Experimental Setup

### 3.1. Laboratory Flume

The experiments were conducted in the channel at Hydraulic and Coastal Engineering Laboratory of Seoul National University, Seoul, South Korea. The channel is a straight rectangular flume with a recirculating pump system and a tilting device. It is 17.5 m long, 0.6 m wide, and 0.8 m high. Top-view and side-view of the flume are represented in Figure 3.1. Entire frames of the flume are made by reinforced steel, and the bottom is uniformly painted. 10mm reinforced glasses are mounted at the side of the steel frames. Head tank with flow stabilizers is located at the front of the flume to stabilize water supply and straighten the flow. Two storage tanks are placed under the channel. The pump can supply water up to 40L/s. The discharge is measured by ultrasonic flowmeter located on the side of the pipe. The discharge is controlled by the control panel, which shows the discharge with real time. Dimensions of the head tank are 2.9 m long, 1.2 m wide, and 1.5 m high. For downstream water-level control, a tailgate is installed at the end of the flume.

The test section is located 7 m far from the head tank. Side-view, top-view of the test section are depicted in Figure 3.2. The bottom of the test section is replaced from the steel frame to 20 mm reinforced glass 0.8 m long and 0.5 m wide. The finite crested weir with the downstream ramp is situated in the middle of the mirror. The configuration of the weir is shown in Figure 3.3. The height of the weir ( $h_w$ ) is 10.4 cm, crest length ( $L_c$ ) is 10 cm, and the bottom length is ( $L_b$ ) is 16 cm. The configuration of the weir is based on the *Korean river design standard*. The 2-D (y-z) auto-traverse is mounted on the channel top-rail and controlled by PC software.

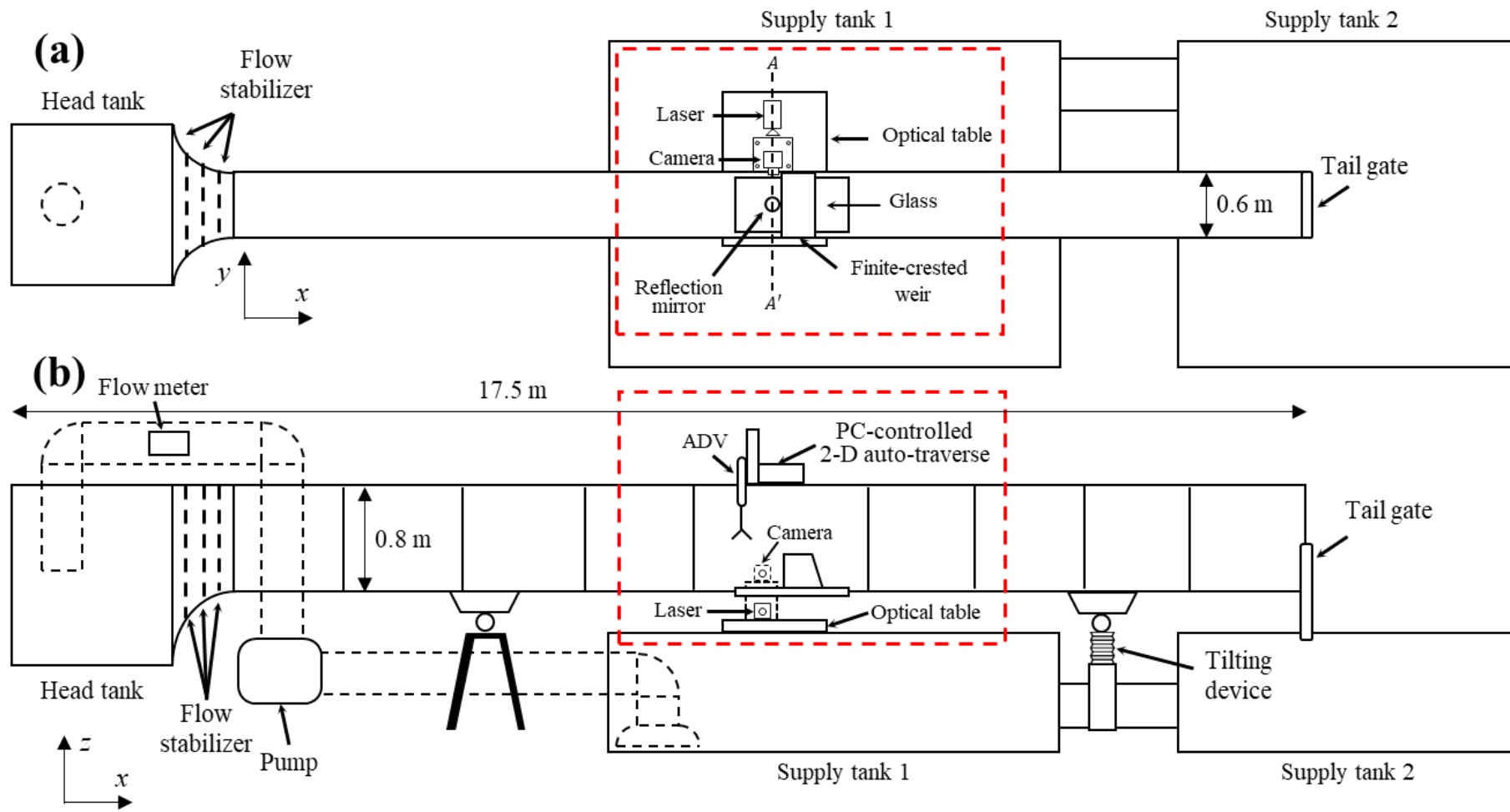


**Figure 3.1** (a) Top-view and (b) side view of the flume.

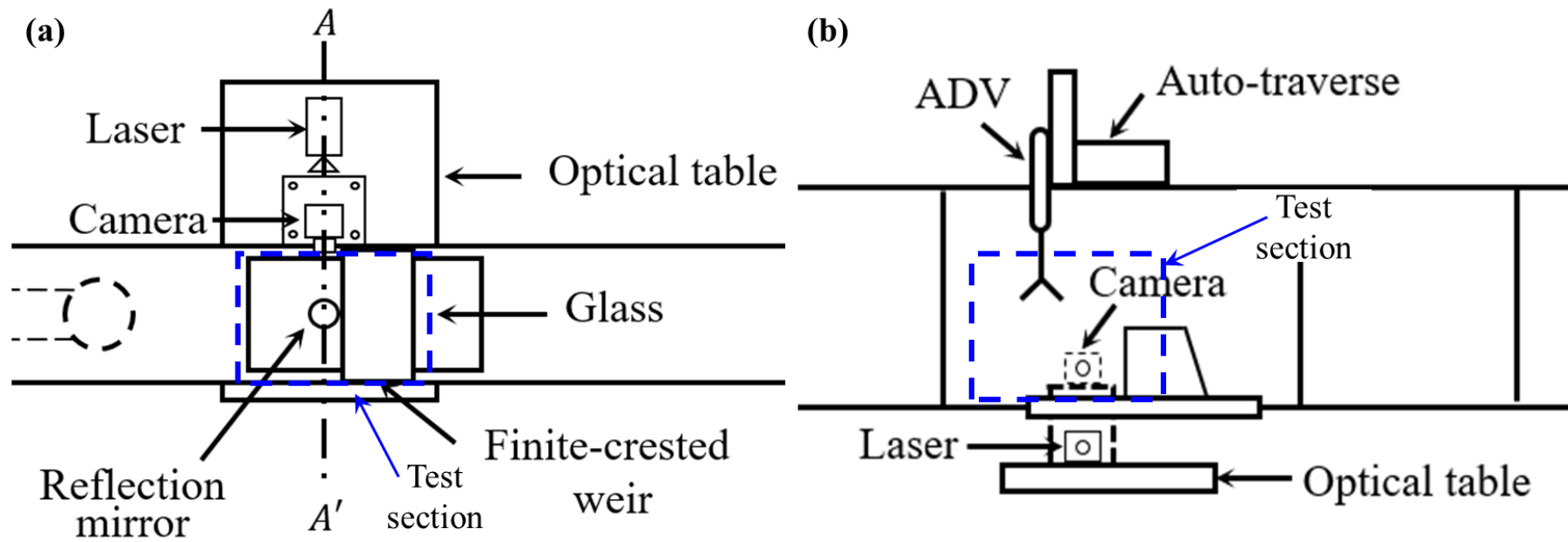


**Figure 3.2** (a) Top-view and (b) side view of the test section.

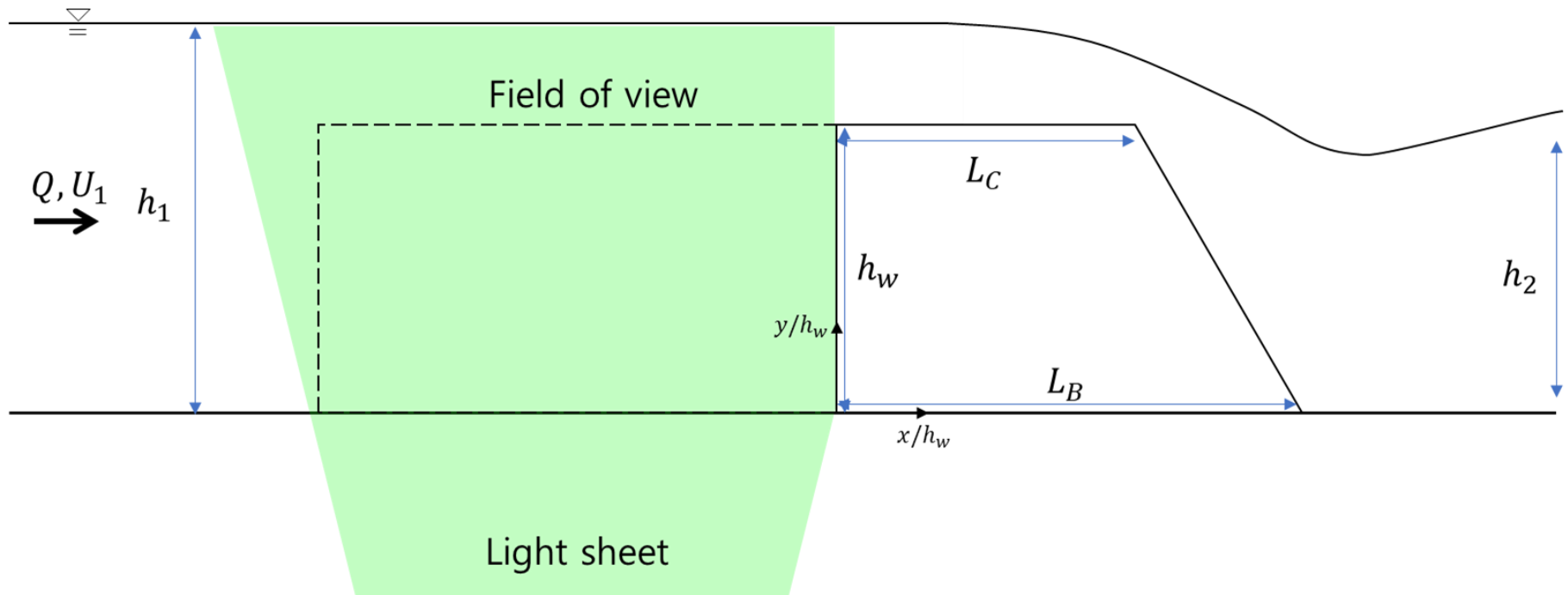


**Figure 3.3** Conceptual diagram of the experimental setup with field of view and coordination

### 3.2. Velocity Measurement

Two-dimensional standard Particle Image Velocimetry were used in the bed-normal plane at the spanwise centerline. Figure 3.4 depicts PIV arrangement and the cross-section view at the middle of channel ( $AA'$ ). An optical table is positioned between the bottom glass and the supply tank 2, which have 6 mm perforated holes in every 2.5 cm, to fix the other devices. The solid-state Nd:YAG laser on the aluminum plate 1 (AL1) is fixed on the table. Underneath the test section, a reflection mirror is installed to convert the direction of the beam to make the light sheet. Real images of the PIV system are presented in Figure 3.5 and 3.6.

The average thickness of the laser sheet is 2mm. TSI powerview 25MP-72  $5120 \times 5120$  pixel resolution CMOS camera with 50mm Nikon F1.8 lens is mounted on the top of a support jack fixed by aluminum plate 2. This support jack can lift its body from 105 mm to 107 mm. The camera and PIV laser are linked to synchronizer and computer software, which can match the laser and image capturing system. Two-paired 0.001s time increment images are captured at a 15 Hz sampling rate.

The field of view shown in Figure 3.3 covers  $1.8h_w$  in a streamwise direction upstream of the weir and  $1.05h_w$  in a vertical direction. Due to the limitation of the memory capacity, 450 paired images (= 30 sec) are captured in this field of view. The temporal-spatial vector fields were processed by using PIVLAB software in Matlab (Thielicke & Stamhuis, 2014). The window size is  $64 \times 64$  pixels with 50% overlap. This size is equivalent to  $2.66 \times 2.66$  ( $\approx h_w/39$ ) mm fluid volume and reasonable since the maximum displacement of the entire experiment within the time increment is 0.2mm.

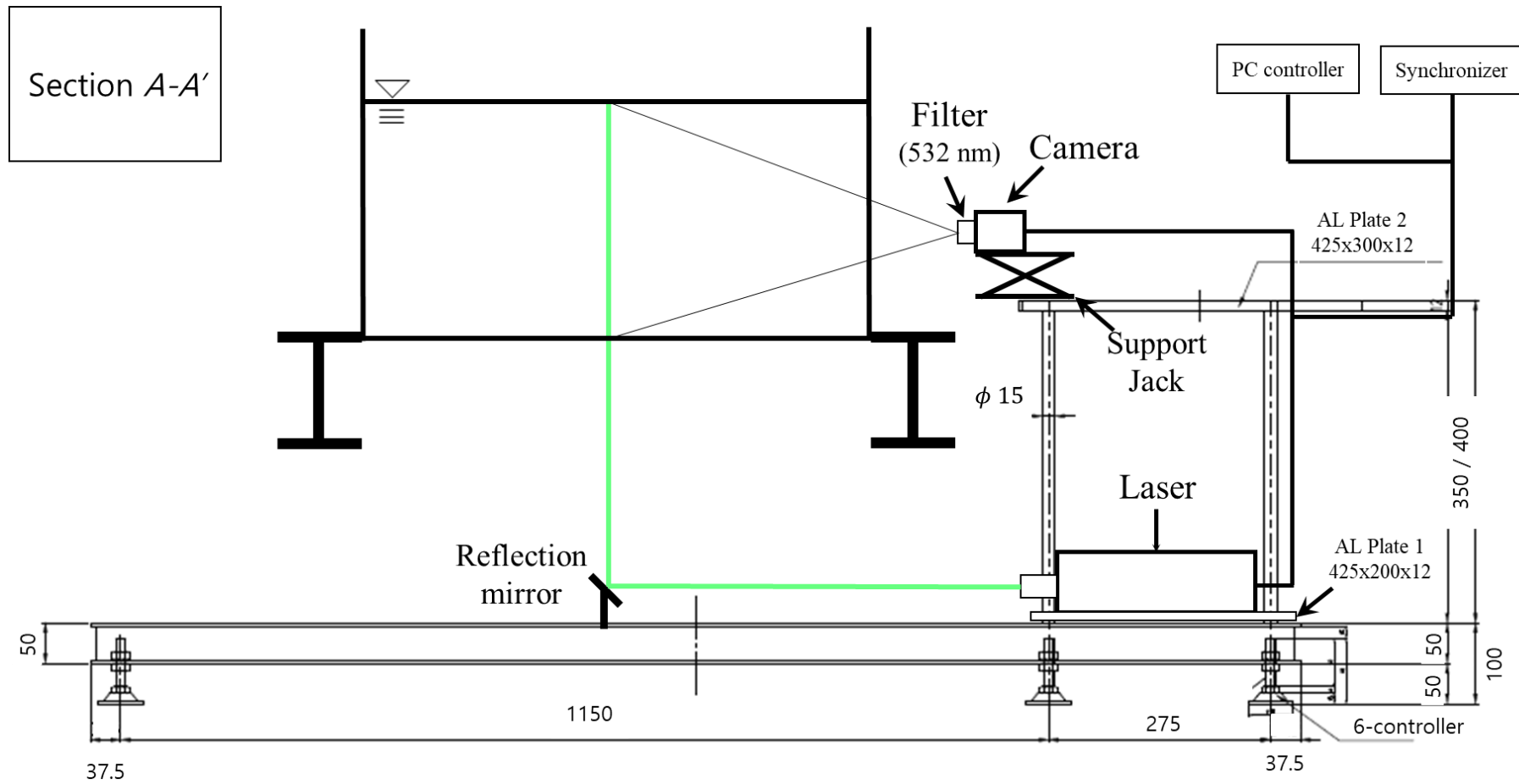


**Figure 3.4** Cross-section view of the test section (AA')

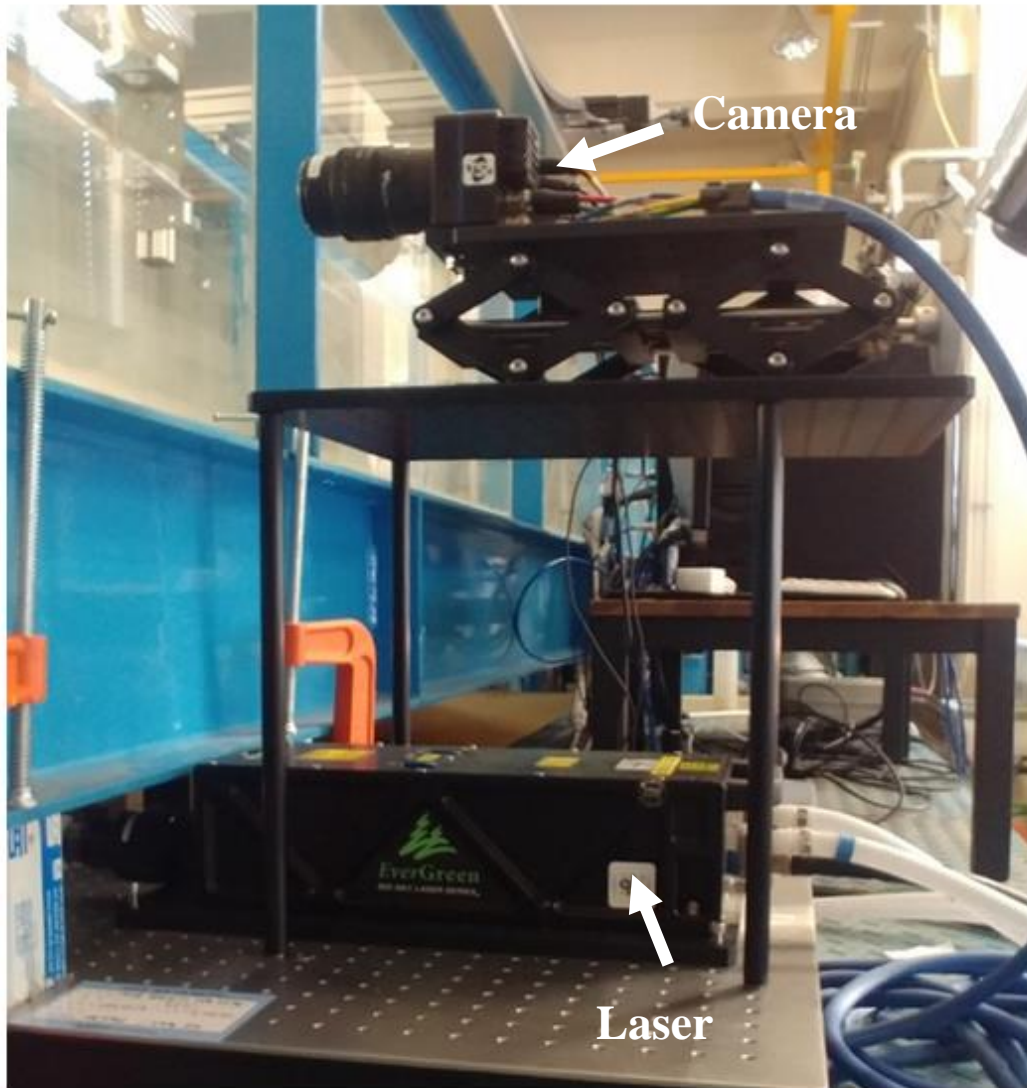


**Figure 3.5** PIV setup – Laser, optical table and platform, and synchronized camera

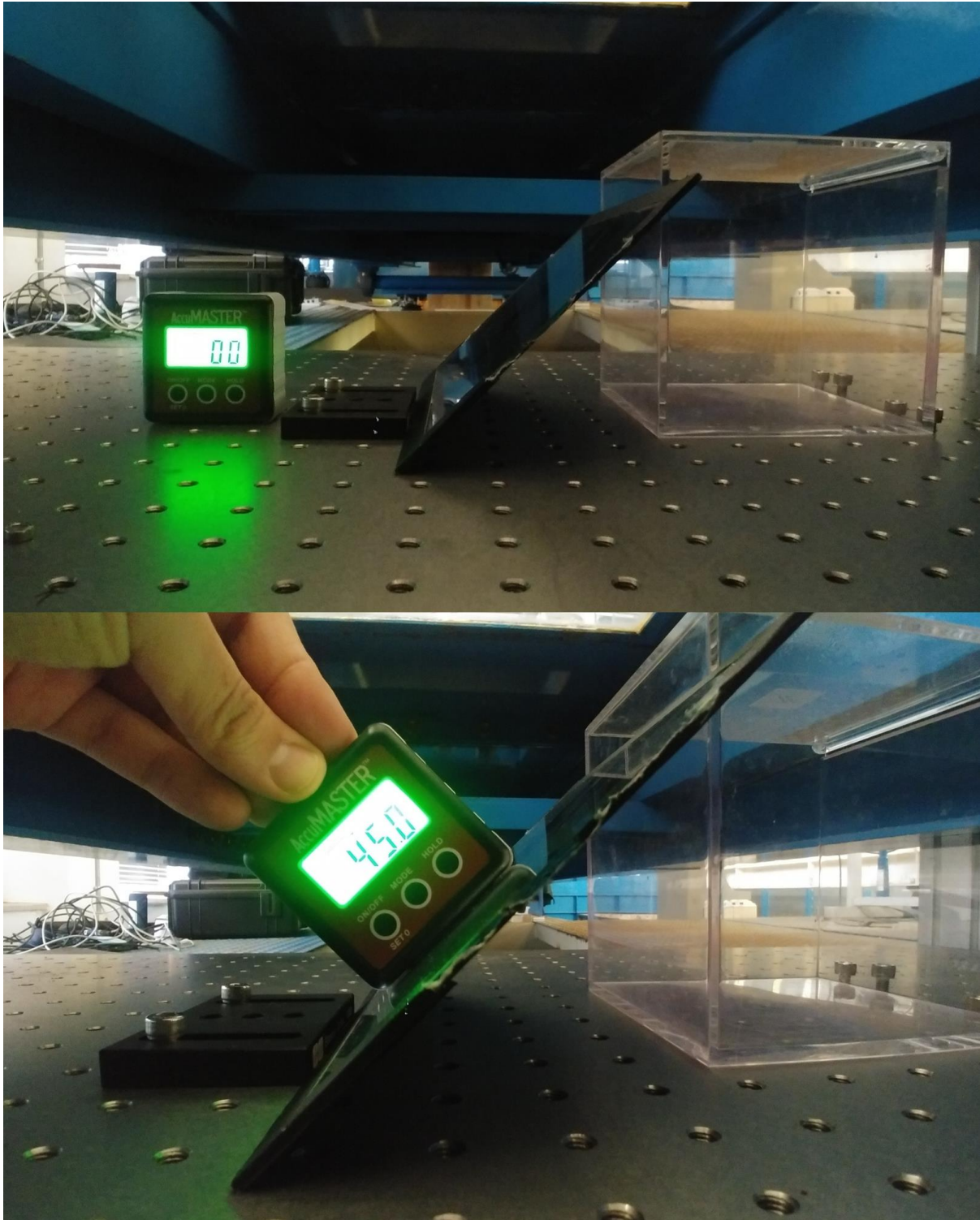


**Figure 3.6** PIV reflection mirror. To obtain proper field of view, the mirror is fixed with  $45^\circ$  angle.

### 3.3. Dimensional Analysis and Experimental Conditions

For deducing flow characteristics and separation and reattachment points in front of the finite crested weir with the downstream ramp, Buckingham  $\Pi$  theory of dimensional analysis was used. The first step of the investigation is to develop the variables that affect the phenomenon. The flow characteristics in Figure 3.4 can be depicted by the function relationship, that is

$$\Phi(h_1, h_2, U_1, h_w, L_C, L_B, \delta_1, \delta_2, x_s, y_s, Q, B, \rho, g, \mu, \sigma_w, s) = 0 \quad (3.1)$$

where  $Q$  is the discharge of the flow,  $B$  is the width of the channel,  $\rho_w$  is the water density,  $\mu_w$  is the water viscosity,  $\sigma_w$  is the water surface tension, and  $s$  is the channel slope.

From the Buckingham  $\Pi$  theory, the following form of function can be deduced.

$$f(h_2/h_1, h_1/L_C, h_1/h_w, P/L_C, \delta_1/h_w, \delta_2/h_w, Re, Re_w, Fr, s) = 0 \quad (3.2)$$

where  $h_2/h_1$  is the ratio between upstream and downstream depth,  $Re$  is Reynolds number based on water depth defined by  $Q/\nu B$ ,  $Re_w$  is weir height based Reynolds number written by  $Qh_w/\nu Bh_1$ ,  $Fr$  is Froude number written by  $Q/B\sqrt{gh_1^3}$ . The relationship between  $Re_w$  and  $Re$  is described by  $Re_w = Re \cdot (h_w/h_1)$ . Based on the previous researches about the weir mention in the *Introduction*, the range of  $Re$  and  $Fr$  is approximately

$$Re = 10,000 \sim 200,000$$

$$Fr = 0.04 \sim 0.34$$

The prime parameter that determines experimental conditions is the water depth upstream of the weir ( $h_1$ ), which is partially dependent on that downstream of the weir ( $h_2$ ). To represent the typical flow pattern at the weir, five experiments were conducted for given two discharges; one experiment for each flow pattern (hydraulic jump, plunging jet, and surface jet flow), and two for surface wave flow. The water surface profile upstream of the weir is measured by the

temporal mean of PIV raw images. One example of the temporal mean of PIV raw images is presented in Figure 3.5. 10 second (=150 image pairs) PIV raw images of entire flow field were used to make the temporal mean image. The measurement error is 5pixels, which are equivalent to 0.2 mm. Water depth over the weir is measured by electrical point gauge. Water depth profile of the entire fields is shown in Figure 3.6. A summary of the experimental setup with parameters is in Table 3.1. In this study, the ranges of  $Re$  and  $Fr$  are bounded in that of the previous researches.

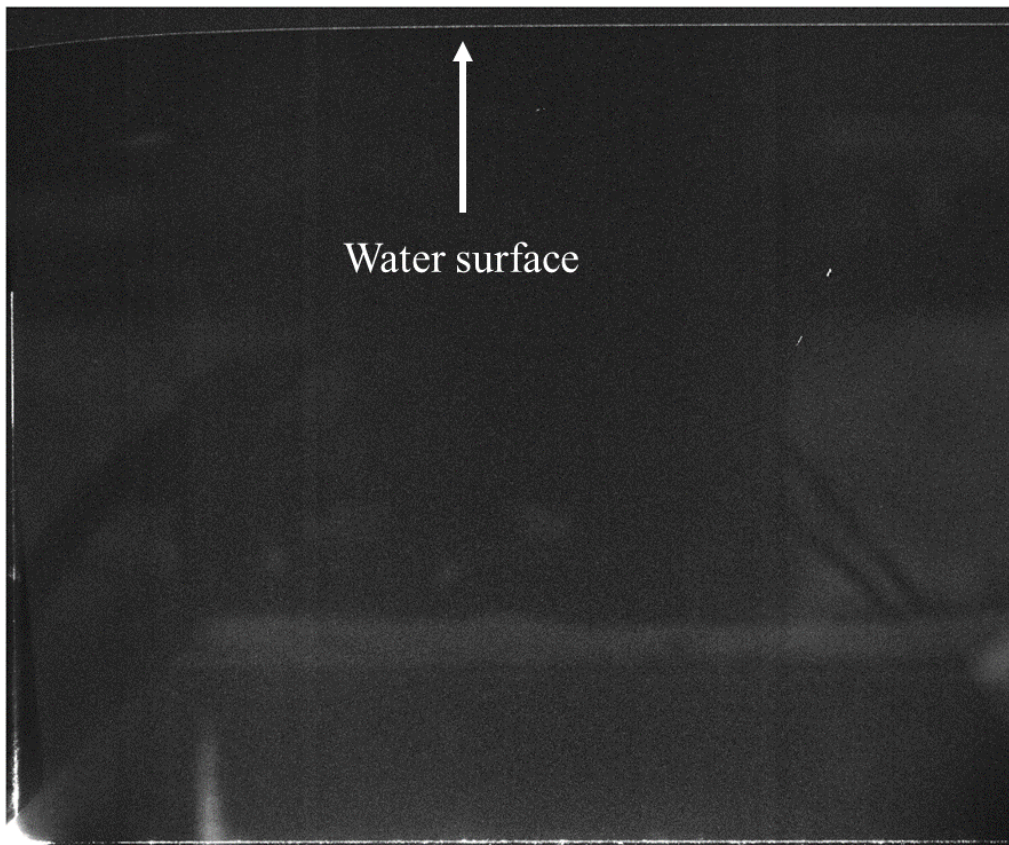


**Figure 3.7** Temporal mean of raw PIV images upstream of the weir

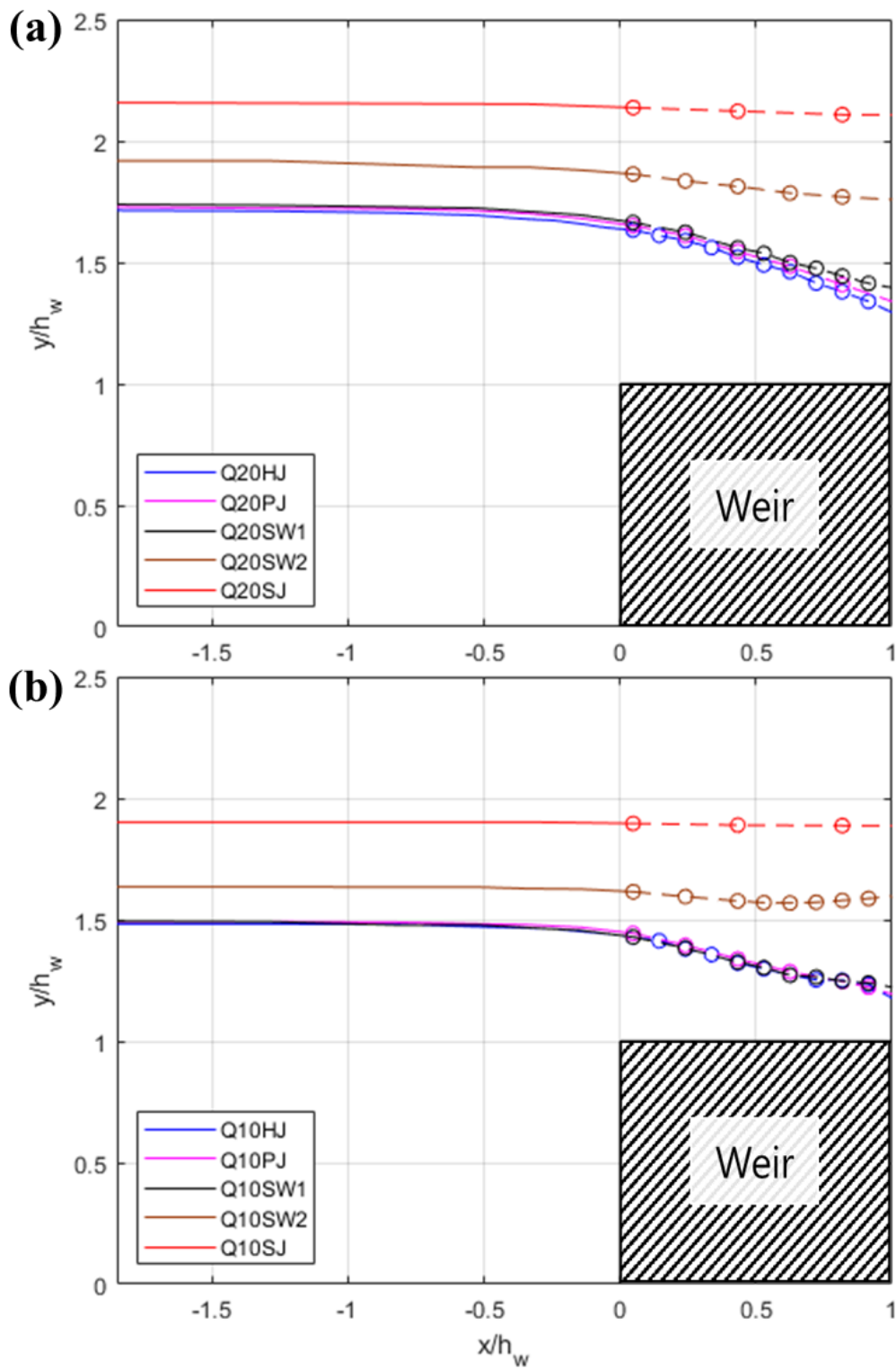


**Figure 3.8** Water surface profile for the experiments; (a):  $Q=20$  L/s (b):  $Q=10$  L/s. The line is drawn by mean PIV image, and the circle points are point measured data. The dot line over the weir is linearly interpolated between points.

**Table 3.1** Experimental Conditions upstream of the finite crested weir with a downstream ramp

Case	Flow condition	$Q$ (l/s)	$h_1$ (m)	$U_1$ (m/s)	$Re$	$Re_w$	$Fr$	$h_w/h_1$
Q20-HJ	Hydraulic jump	20	0.179	0.187	33,333	19,420	0.141	0.583
Q20-PJ	Plunging jet		0.180	0.185	33,333	19,252	0.139	0.578
Q20-SW1	Surface wave		0.181	0.184	33,333	19,145	0.138	0.574
Q20-SW2	Surface wave		0.200	0.167	33,333	17,375	0.119	0.521
Q20-SJ	Surface jet		0.225	0.148	33,333	15,438	0.100	0.463
Q10-HJ	Hydraulic jump	10	0.154	0.108	16,667	11,242	0.088	0.674
Q10-PJ	Plunging jet		0.155	0.107	16,667	11,176	0.087	0.670
Q10-SW1	Surface wave		0.155	0.107	16,667	11,153	0.087	0.669
Q10-SW2	Surface wave		0.170	0.098	16,667	10,195	0.076	0.612
Q10-SJ	Surface jet		0.198	0.084	16,667	8,763	0.060	0.526

The boundary layer thickness of each experiment was estimated by the streamwise velocity profile obtained from the acoustic Doppler velocimeter. As there is no external free stream layer, however, it is challenging to derive 99% boundary layer thickness. Hence, the displacement thickness and momentum thickness were evaluated for the alternative estimators. Figure 3.6 (a) shows the boundary layer profile of the case *Q20-PJ* measured at  $x/h_w = 30$  where the velocity profile is not changed due to the presence of the weir. The quantities were normalized by the skin-friction velocity,  $u_\tau$ , and kinematic viscosity with the log-law constant ( $\kappa = 0.41$  and  $C = 5.5$ ), and the skin-friction velocity is 5.9 mm/s. Figure 3.6 (b) displays the estimated velocity profile using the skin-friction velocity calculated by the log-law fitting shown in Figure 3.6 (a). To estimate the displacement thickness and momentum thickness under no external free stream condition, it is assumed that the velocity profile follows the log-law profile and the maximum velocity located at the surface. As a result, the oncoming boundary layer of this experimental case has the displacement thickness of  $\delta_1 = 1.60$  cm, and the momentum thickness of  $\delta_2 = 1.28$  cm. The contribution of extrapolated velocity for estimating the displacement and momentum thickness is approximately 10 ~ 20%. Therefore, it is found that the oncoming boundary layer is lower than the weir height.

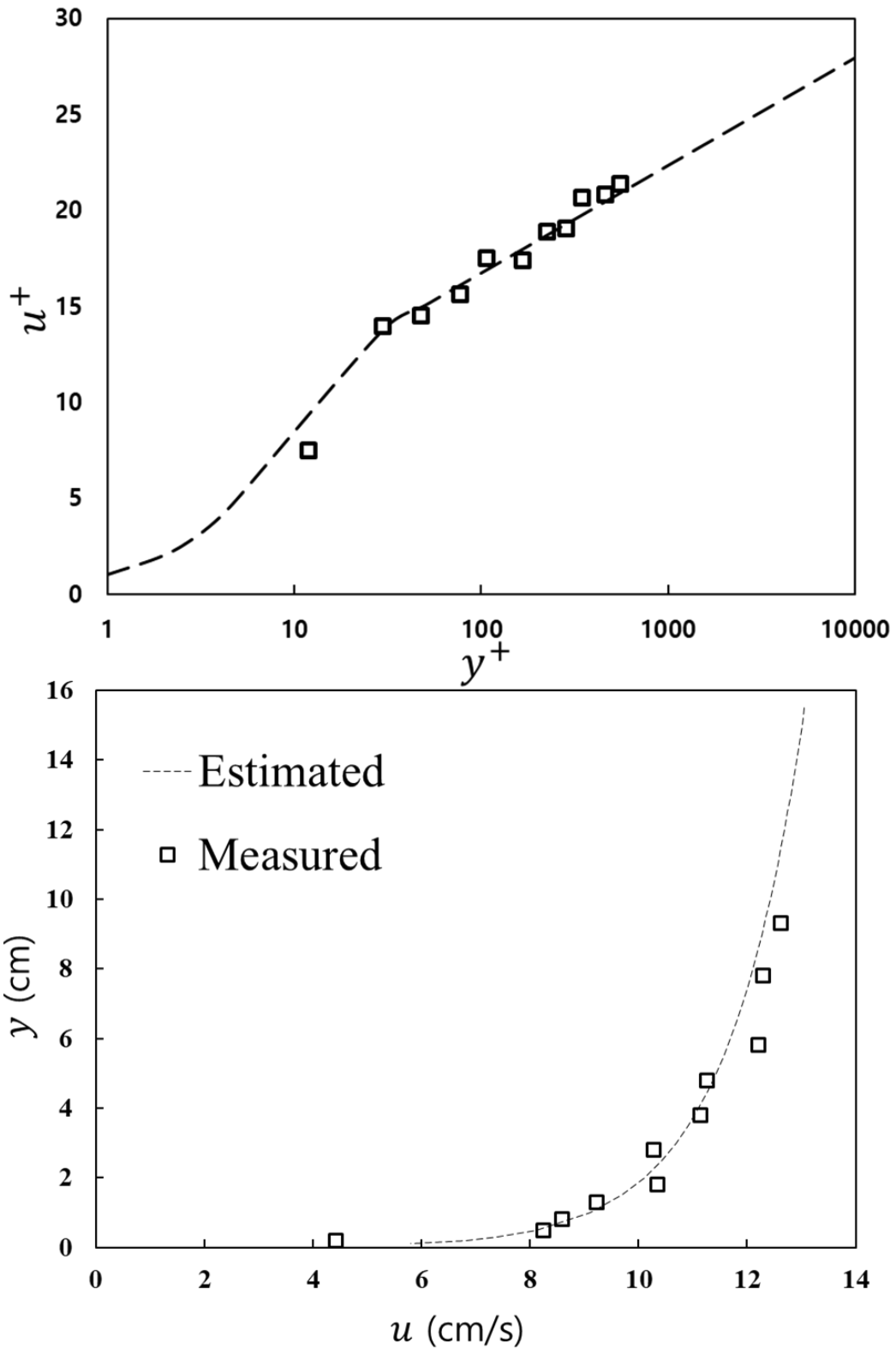


**Figure 3.9** Log-law fitting of measured velocity profile and estimated velocity profile to estimate boundary layer thickness

## 4. Results and Discussion

### 4.1. Flow Field Analysis

#### 4.1.1. Velocity Statistics

Fields of the velocity statistics were studied to identify the effects of separation. Examples of the instantaneous streamwise velocity acquired from the case *Q20-HJ* are shown in Figure 4.1. Three subsequent velocity fields (15-17th frame) and  $u = 0$  line (white line) are presented in the figure. As  $x$  approaches the weir, the boundary layer widens, and the large inclined structures, which divide the outer flow region and boundary layer, are clearly revealed. Furthermore, the area of reverse flow is rapidly changed within short period of time (2 frames  $\approx 0.133 \text{ sec}$ ). This demonstrates the substantial unsteadiness was developed at the bottom of the weir front.

Figure 4.2 shows the mean streamwise and vertical velocity field with the streamlines estimated from the mean velocity at *Q20-HJ*. The flow goes from left to right, and all velocity values were normalized by the oncoming cross-section averaged velocity,  $U_1$ . The mean streamwise velocity decelerates near the channel bed as the flow approaches the weir, and the reverse flow is developed at the bottom in front of the weir. In the region of  $y/h_W > 1$ , however, the mean streamwise velocity accelerates when the flow approaches the weir. The maximum mean streamwise velocity locates at the weir's upstream edge. In the vertical direction, the velocity is not changed significantly far from the weir, but the ascending velocity is developed near the upstream edge of the weir. The magnitude of the maximum ascending velocity near the edge is more than two times of the oncoming averaged velocity. similar to the

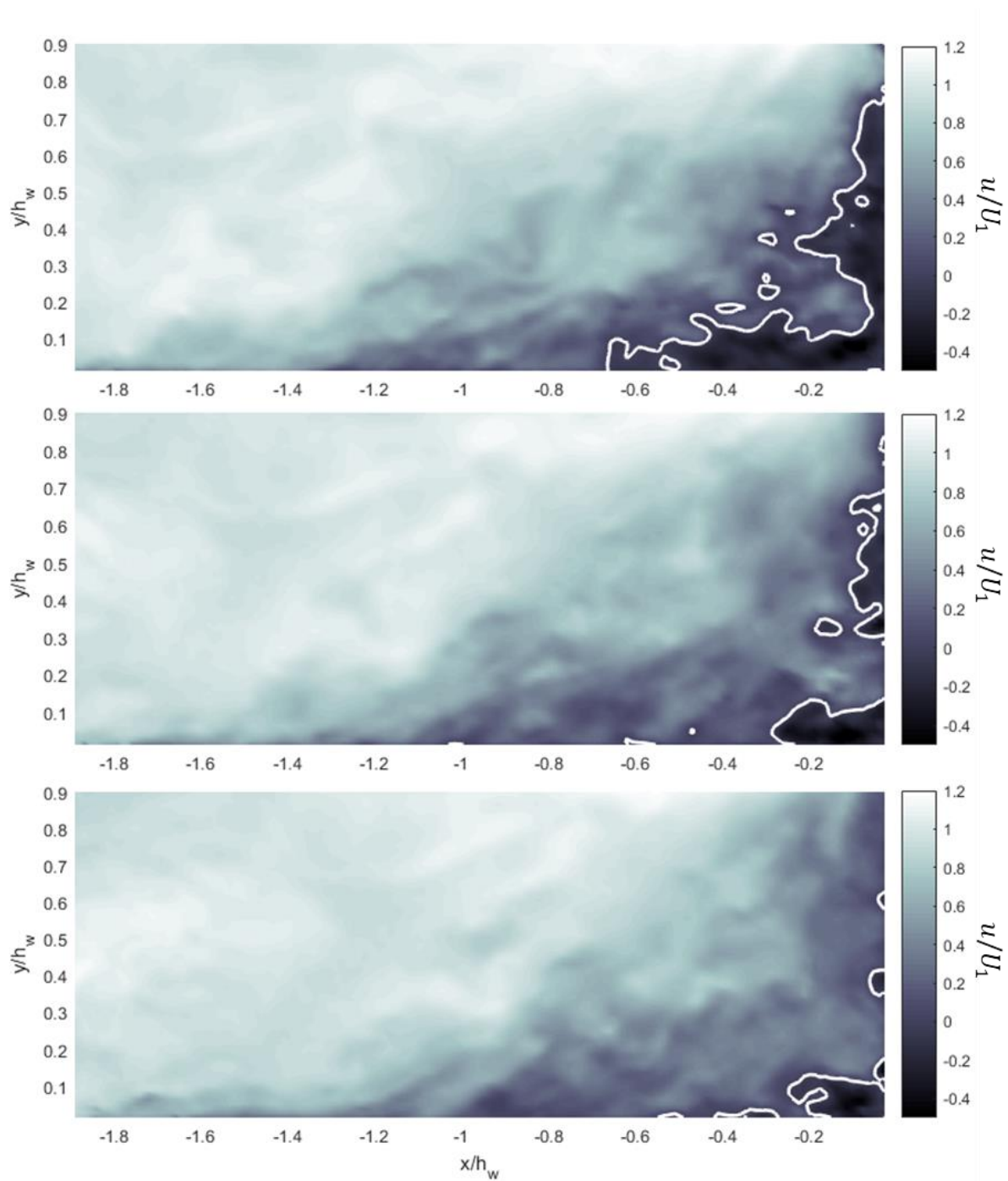


**Figure 4.1** Instantaneous streamwise velocity at 15-17th frame and white line is  $u = 0$ .

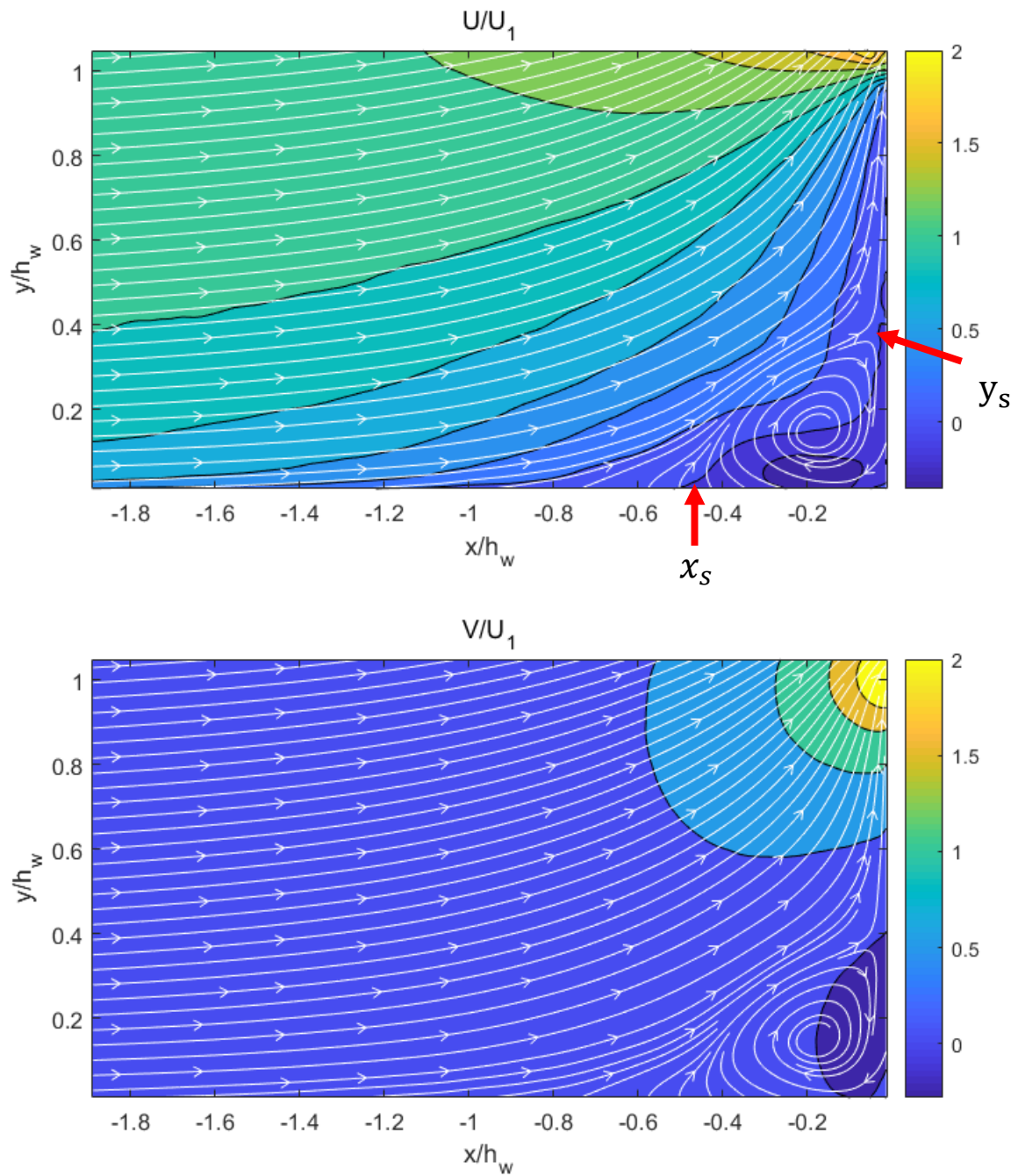


**Figure 4.2** Mean streamwise and vertical velocity field upstream of the weir normalized by the cross-section averaged velocity,  $U_1$ , with the streamlines calculated from mean velocity (case: *Q20-HJ*).

mean streamwise velocity, the descending flow is formed at the bottom upstream of the weir. The streamlines clearly show the region of the recirculation at the bottom upstream of the weir. The outer streamlines bound the rotating flow in this region. The separation and reattachment points can be recognized from the streamlines, and their estimated locations are illustrated.

The variation of the mean velocity fields and streamlines regarding the different hydraulic conditions are presented in Figures 4.3 and 4.4. For all cases, the maximum streamwise and vertical velocity are situated at the edge of the weir, and the recirculation zone and reverse flow are formed at the bottom in front of the weir. The rotating streamlines are bounded by the outer streamline. The separation and reattachment points are approximately identified. In spite of the discharge change, little variation exists in the mean flow fields at the same flow pattern. However, prominent changes are noticed when the upstream water depth increases. In the *HJ*, *PJ*, and *SW1* cases, similar mean flow fields and streamlines are displayed. It is because the upstream water depth is not substantially changed in these cases. When the water depth increases (*HJ*·*PJ*·*SW1* → *SW2* → *SJ*), the magnitude of the maximum streamwise velocity decreases and the region of the reverse flow enlarges. For the vertical velocity, the maximum ascending velocity located at the upstream edge is more than  $2U_1$  regardless of the flow pattern and upstream water depth. The reverse flow of the vertical velocity widens in the vertical direction as the water depth increases. Hence, it can be inferred that the separation and reattachment points are relatively more dependent on the upstream water depth than on the discharge.

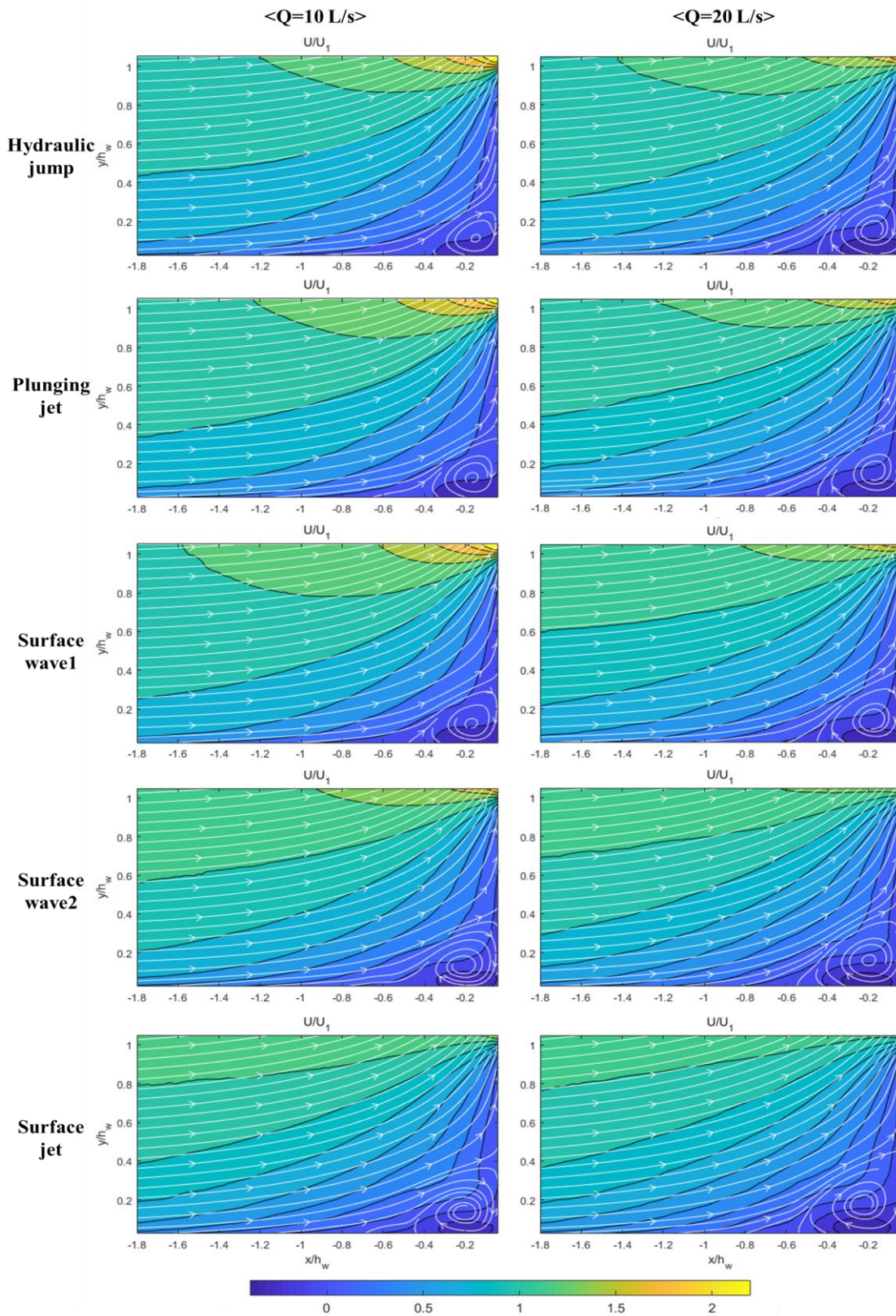


**Figure 4.3** Mean streamwise velocity normalized by the cross-section averaged velocity,  $U_1$ , with the streamlines calculated from mean velocity field.

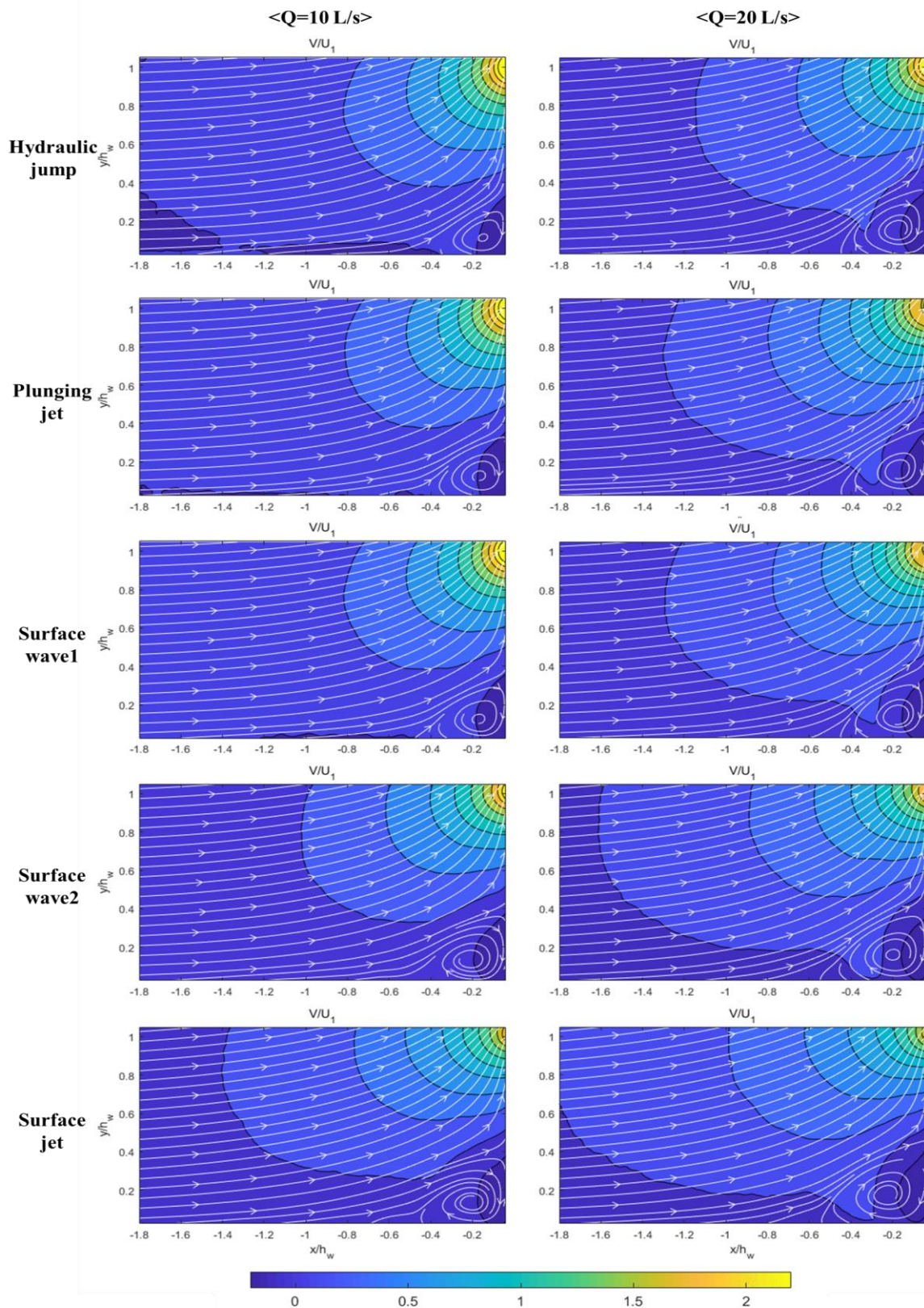


**Figure 4.4** Mean vertical velocity normalized by the cross-section averaged velocity,  $U_1$ , with the streamlines calculated from mean velocity field.

Normalized root-mean-square (RMS) velocity of streamwise and vertical direction with the streamlines were presented in Figure 4.5 and 4.6 respectively to show the spatial distribution of the velocity fluctuation. The vertical length of the intense fluctuation region (e.g.  $u_{rms}/U_1 > 0.1$ ) widens as the flow approaches the weir. High levels of the streamwise velocity fluctuation are found at the recirculation zone and accelerating zone near the upstream edge. However, the streamwise fluctuation level decreases at the lower part of the recirculation zone, where  $-0.2 < x/h_w < 0$  and  $0 < y/h_w < 0.1$ . For the vertical velocity, the strong fluctuation occurs at the center of the rotating streamlines. The maximum magnitude of the RMS streamwise and vertical velocity are approximately  $0.25U_1$  and  $0.15U_1$ , respectively. Similar to the mean flow fields, the area of the intense streamwise fluctuation region expands to the upstream when the upstream water depth increase, but the spatial distributions of the vertical fluctuation are relatively consistent in all cases.

Lastly, the spatial distributions of the normalized Reynolds stress are shown in Figure 4.7. At  $-0.2 < x/h_w < 0$  and  $0 < y/h_w < 0.5$  where oncoming streamlines split into the ascending streamlines and recirculating streamlines, the maximum negative Reynolds stress are developed. On the other hand, Reynolds stress at the ascending region of the rotating streamlines ( $-0.4 < x/h_w < -0.2$  and  $0 < y/h_w < 0.2$ ) has positive values. Moreover, maximum positive Reynolds stress is found at the upstream edge of the weir.

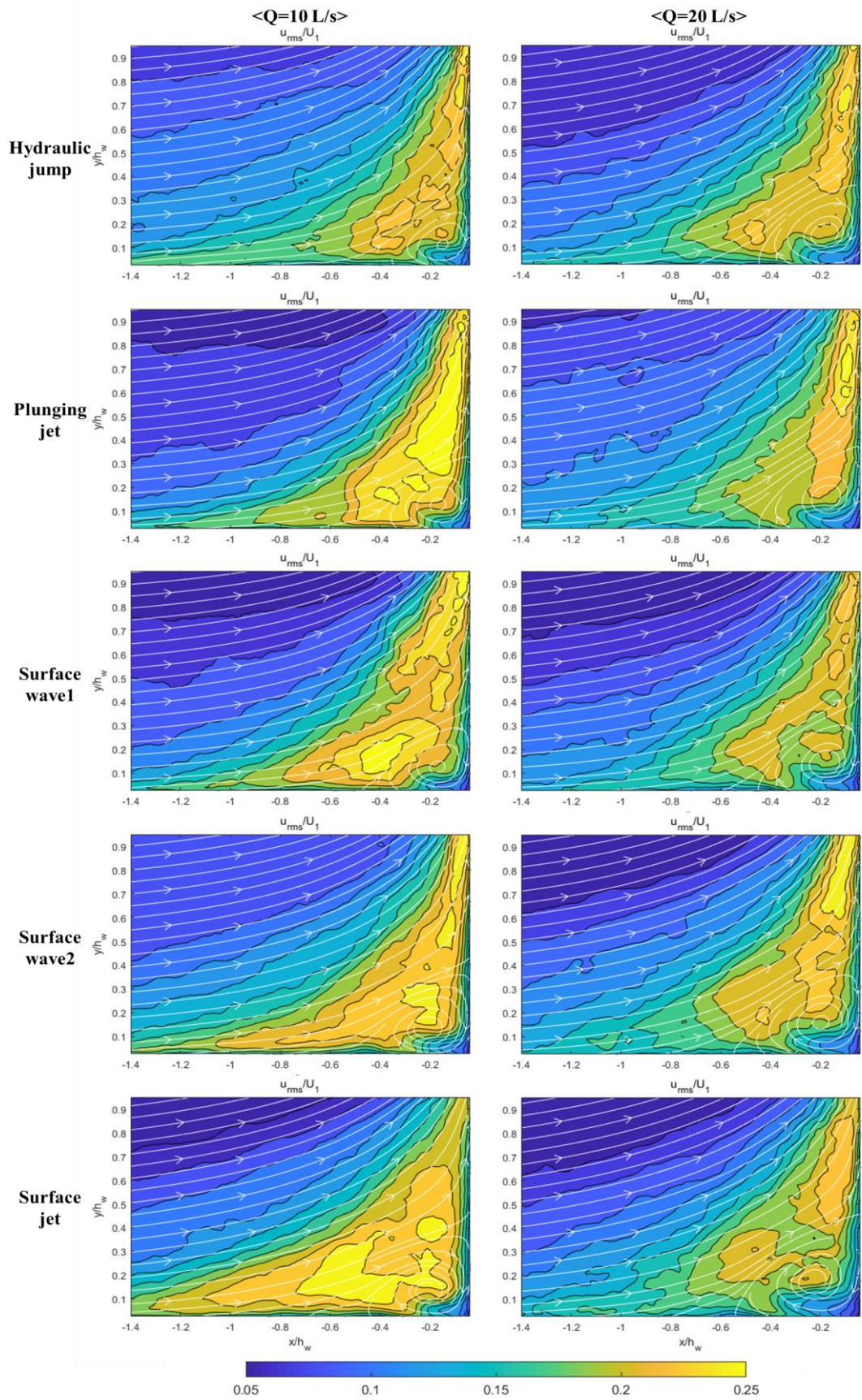


**Figure 4.5** Normalized RMS streamwise velocity

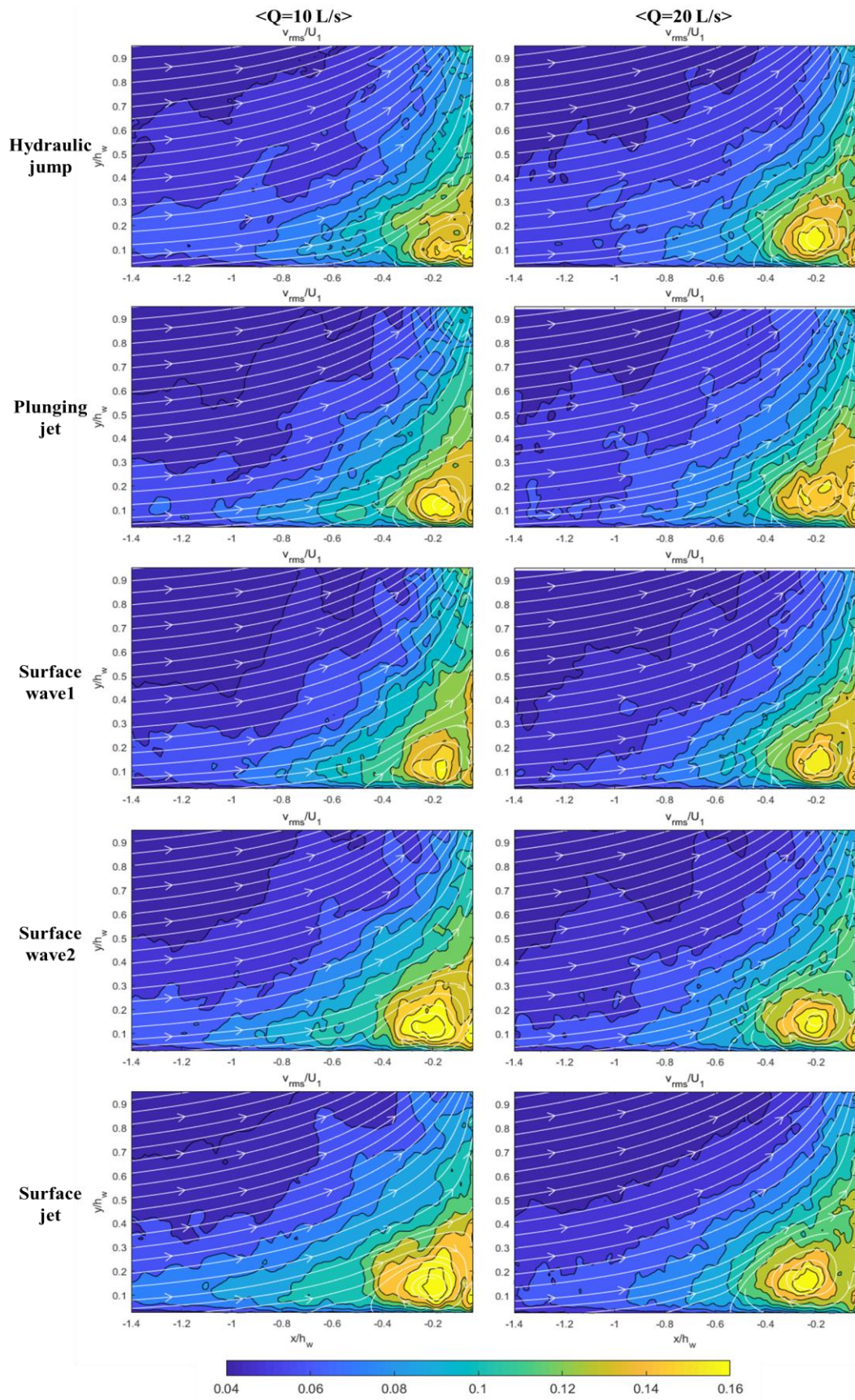


Figure 4.6 Normalized RMS vertical velocity

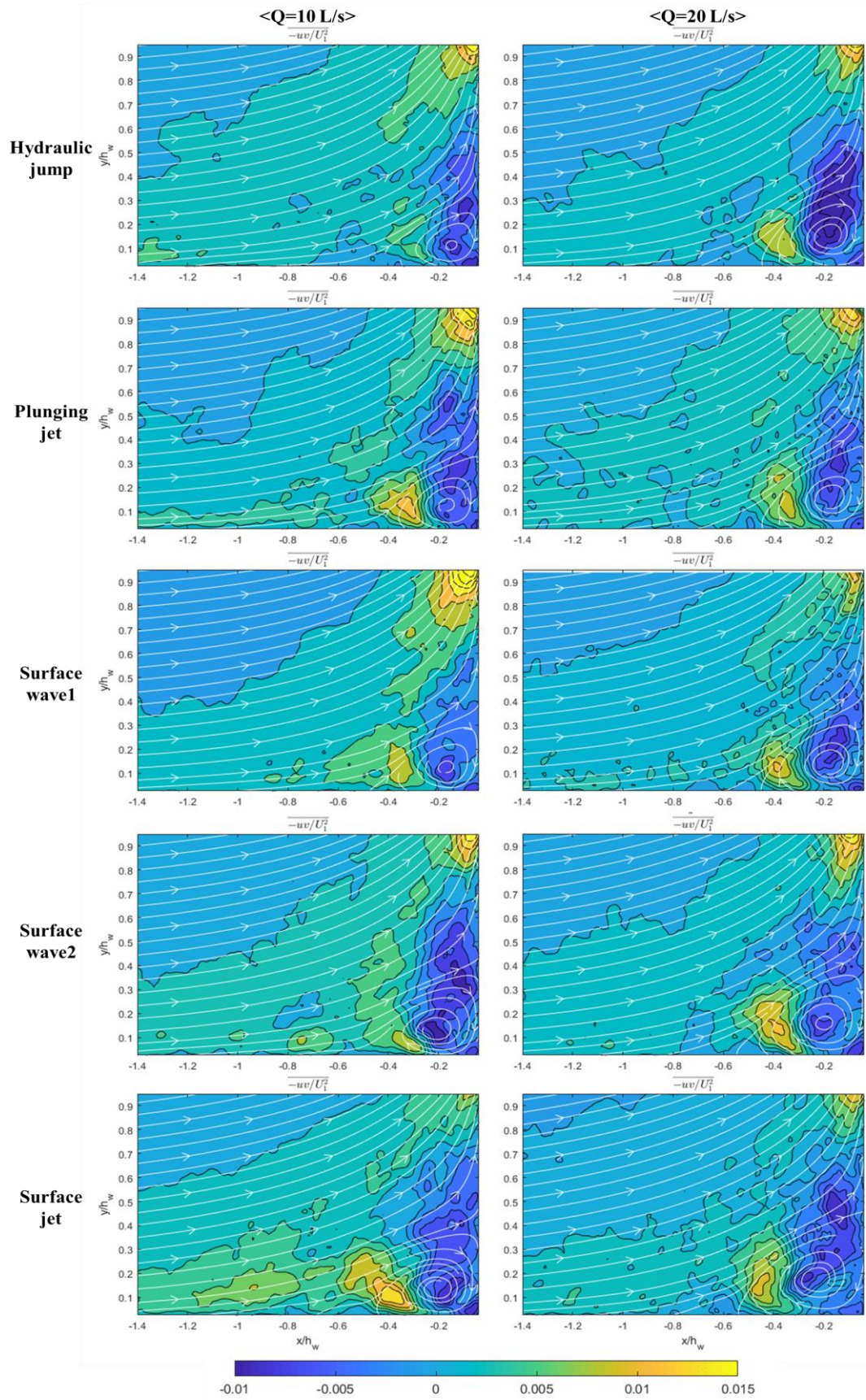


Figure 4.7 Normalized Reynolds stress

### 4.1.2. Conditional Averaging

The best way to analyze the shape of the flow separation and the location of the separation and reattachment points is to inspect the streamline patterns. However, it is difficult for the turbulent flows to precisely assess the separation size as a time function, because of unsteadiness and meandering at any instant (Pearson et al., 2013). Therefore, the entire area of the reverse flow ( $u < 0$ ) was applied to estimate the level of flow separation at an instantaneous velocity field, since the reverse flow occurs within the flow separation region. As the reverse flow might be spread and disjointed, all disjoint regions were taken for the integration. In this study's experimental cases, the reverse flow was found  $-1.4 < x/h_w < 0$ . The conditional averaging method is used to observe instances of similar flow fields. This method is the best nonlinear estimate for a quantity in terms of certain event criteria (Adrian & Moin, 1988). The reverse flow area is chosen for the event.

For the instantaneous velocity field at  $t = t_k$  over PIV field of view  $S$ , the entire area of the reverse flow is defined as

$$A_0(t_k) = \int_S \varphi(u(x, y, t_k)) dS$$

$$\varphi(u) = \begin{cases} 0 & u \geq 0 \\ 1 & u < 0 \end{cases}$$

The set of the entire time instants  $T$  where the normalized reverse flow area has a value within the limits  $[a, b]$  is written by

$$T_{[a,b]} = \{t_k | a \leq A_0(t_k)/h_w^2 \leq b\}$$

The conditional averaged field of all  $t_k \in T_{[a,b]}$  is

$$\langle u(t_k) \rangle_{t_k \in T_{[a,b]}}$$

where  $\langle \cdot \rangle$  is the ensemble averaged of the entire PIF field of view.

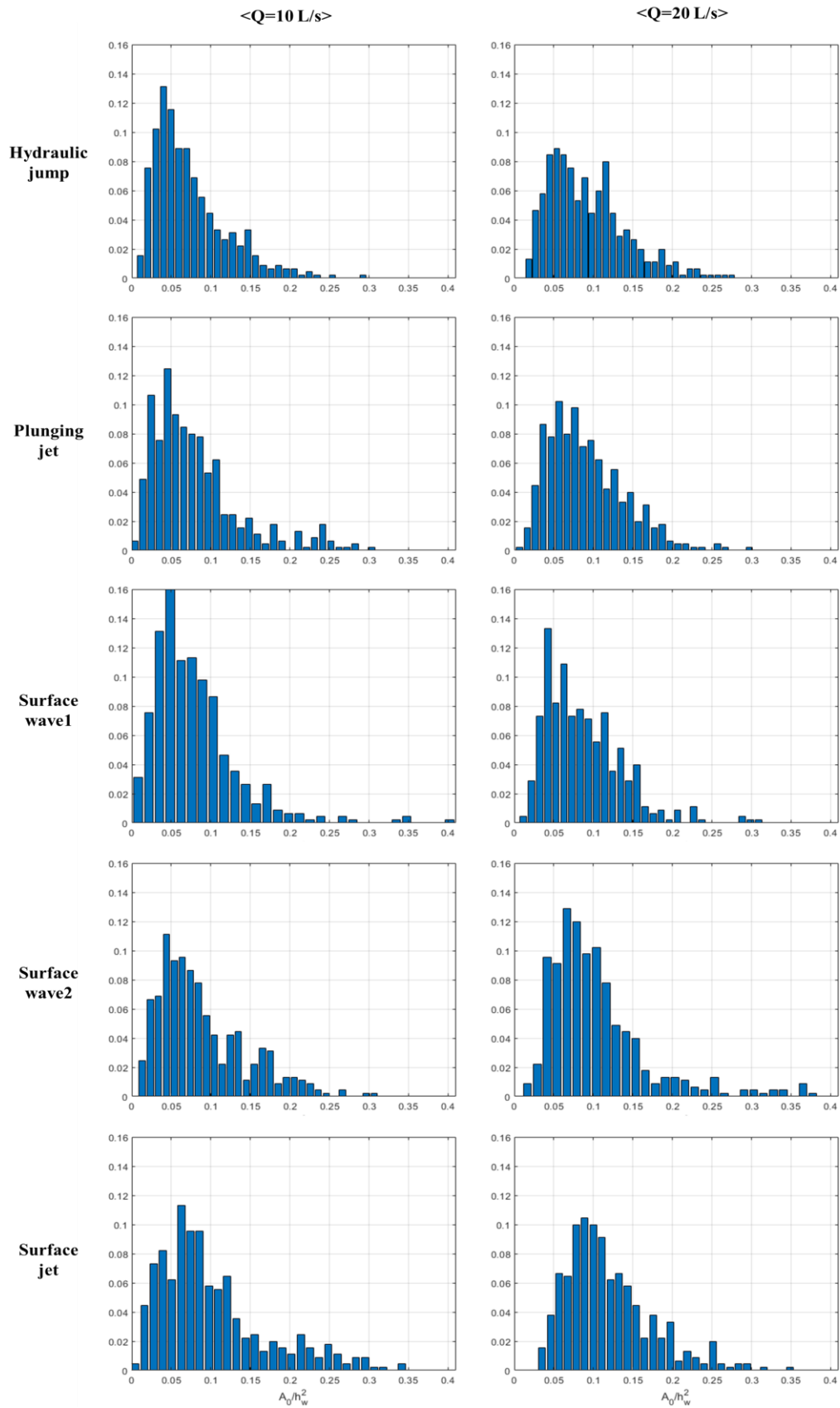
The statistics, probability density function (PDF) and cumulative distribution function (CDF) of  $A_0/h_w^2$  are shown in Table 4.1, and Figure 4.8 and 4.9. The PDF of all experimental cases is positively skewed. The minimum size of the reverse flow is always larger than 0, which means that reverse flow exists at any time instants. The maximum size of the reverse flow is more than three times the median of the reverse flow. This represent a massive separation flow at the upstream of the weir.

Figure 4.10 and 4.11 show the streamlines calculated at the conditional averaged field of the first and last 10% of the reverse flow region. The separation points estimated by mean zero shear ( $\circ$ ) and fraction of time method ( $\blacktriangle$ ) are depicted in both figures. The conditional averaged streamlines of the 0 ~ 10% of the reverse flow create the recirculation zone at the weir corner. Few streamlines in the recirculation zone stem from the boundary layer upstream of the recirculation. This separation is ‘open’ meaning that there is direct in-plane fluid entrainment from the oncoming boundary layer.

For the last 90 ~ 100% of the reverse flow region in Figure 4.11, large structure generated from the separation point is revealed. The separation is ‘closed’ and in-plane entering does not exist. However, the closed separation has out-of-plane motion which travels along the weir’s front corner in spanwise direction. The out-of-plane motion shown by Stüer et al. (1999) play a vital role in shape change of the separation flow. Moreover, few streamlines in the separation flow extend up and over the weir. This means that mass from the separation flow region ejects over the edge of the weir. It was demonstrated by Stüer et al. (1999), Lanzerstorfer & Kuhlmann (2012), and Pearson et al. (2013). These researches showed that the recirculating vortex rolls up, moves spanwise adjacent to the corner, and extends its size until it finally leaks into the downstream flow. These results were analyzed at FFS in both laminar (Stüer et al.,

**Table 4.1** Statistics of the size of reverse flow.

	Case	mean	median	Standard deviation	min	max	Q1	Q3	90 percentile	1st leak
Q=20 l/s Re=33,333	Q20-HJ	0.0925	0.0840	0.0495	0.0183	0.2775	0.0547	0.1189	0.1589	0.0741
	Q20-PJ	0.0909	0.0816	0.0485	0.0065	0.2979	0.0551	0.1206	0.1591	0.0767
	Q20-SW1	0.0869	0.0779	0.0486	0.0123	0.3089	0.0484	0.1157	0.1498	0.0810
	Q20-SW2	0.1041	0.0889	0.0630	0.0167	0.3812	0.0644	0.1230	0.1799	0.0926
	Q20-SJ	0.1185	0.1067	0.0540	0.0352	0.3489	0.0801	0.1448	0.1940	0.1149
Q=10 l/s Re=16,667	Q10-HJ	0.0732	0.0618	0.0461	0.0110	0.2935	0.0393	0.0945	0.1420	0.0618
	Q10-PJ	0.0798	0.0649	0.0567	0.0037	0.3051	0.0406	0.1015	0.1540	0.0747
	Q10-SW1	0.0792	0.0677	0.0541	0.0079	0.4103	0.0434	0.1000	0.1394	0.0784
	Q10-SW2	0.0882	0.0732	0.0553	0.0134	0.3077	0.0461	0.1207	0.1710	0.0834
	Q10-SJ	0.1011	0.0826	0.0683	0.0044	0.3415	0.0537	0.1271	0.2108	0.1044



**Figure 4.8** PDF of the reverse flow area at instantaneous streamwise velocity

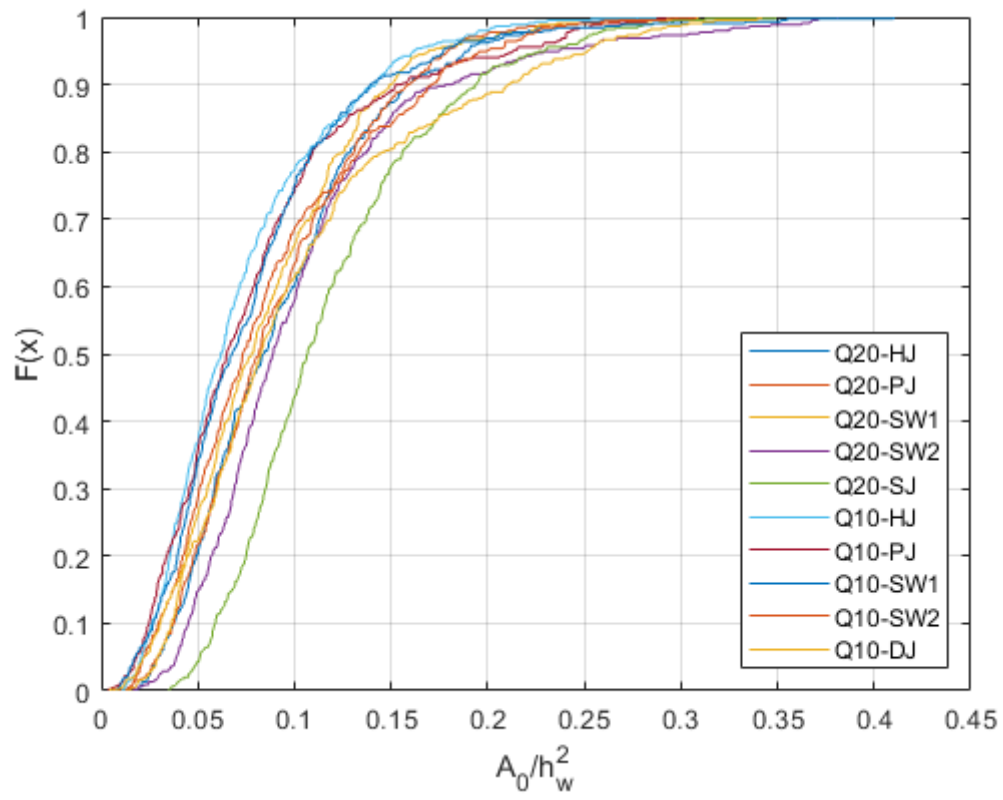


**Figure 4.9** CDF of the reverse flow area at instantaneous streamwise velocity

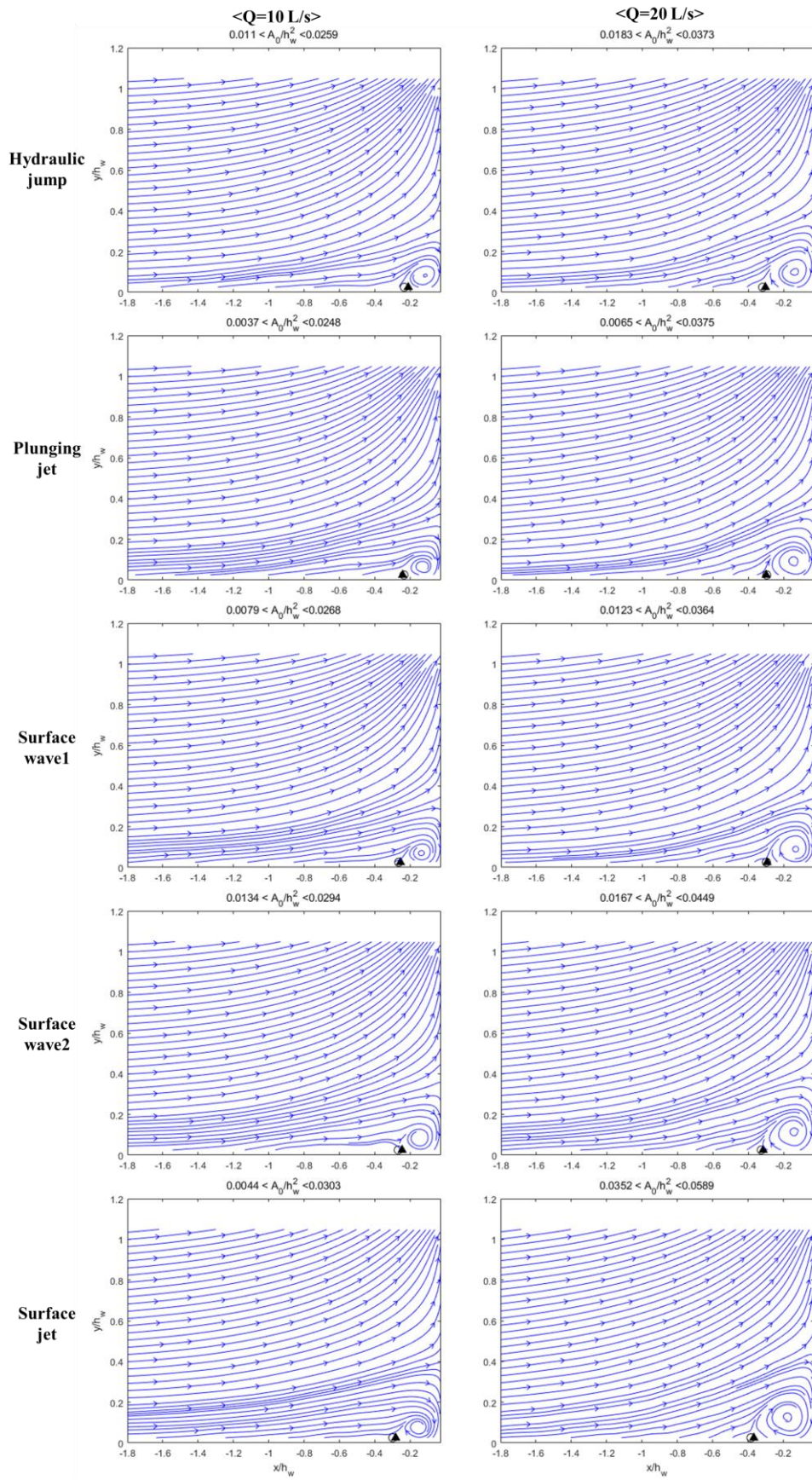


**Figure 4.10** Streamlines of 0 ~ 10 % reverse flow fields

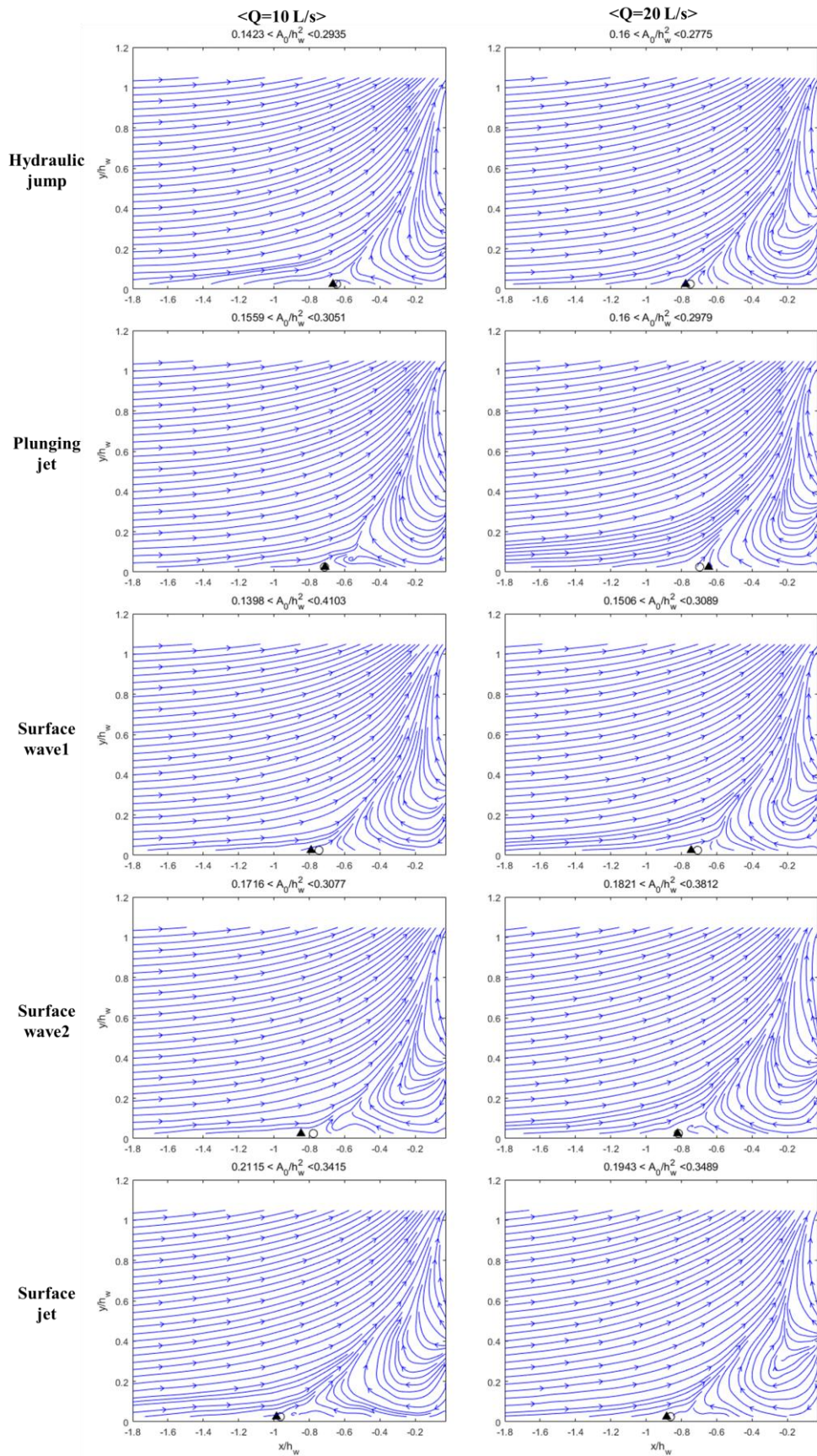


Figure 4.11 Streamlines of 90 ~ 100 % reverse flow fields

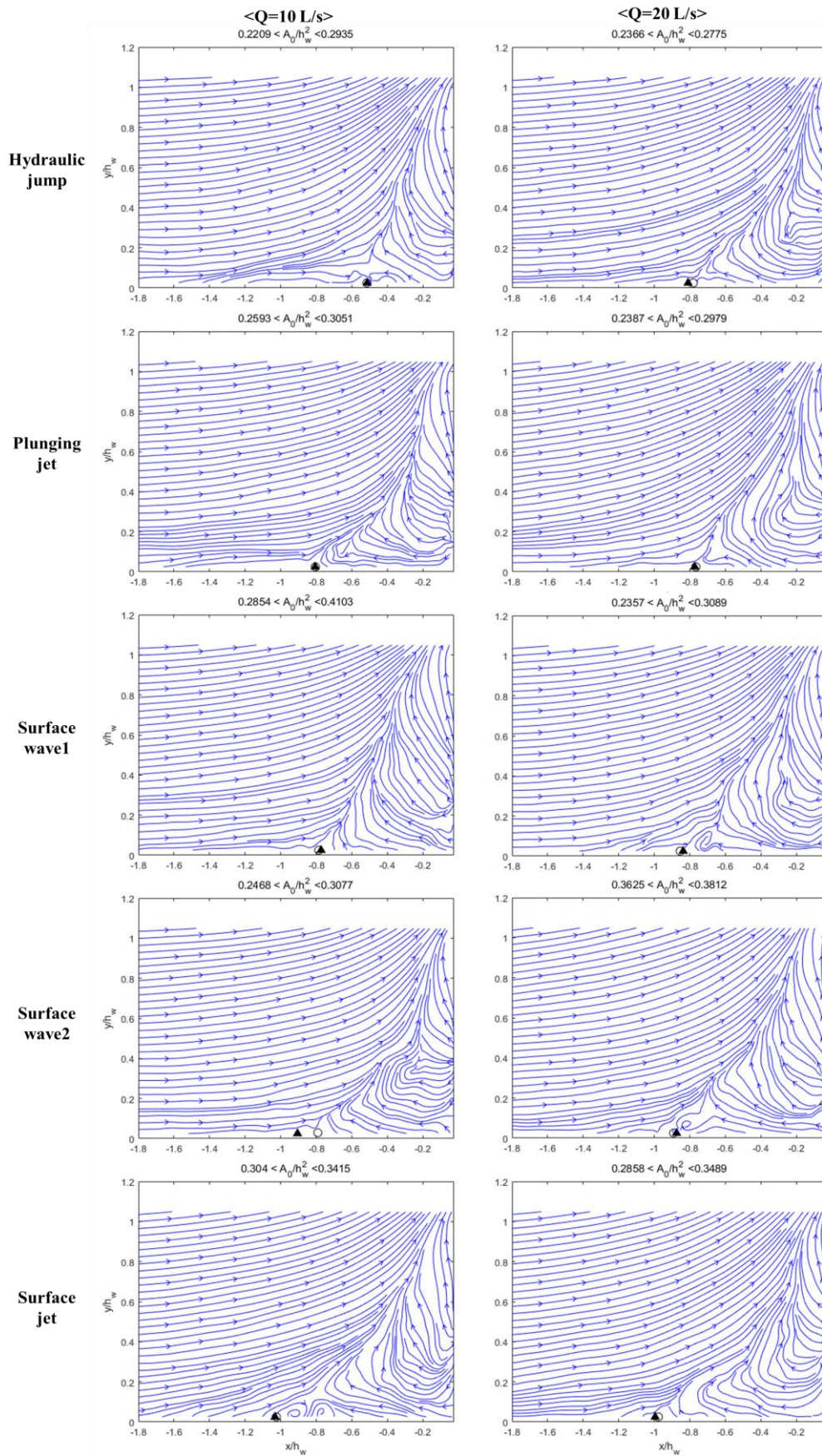
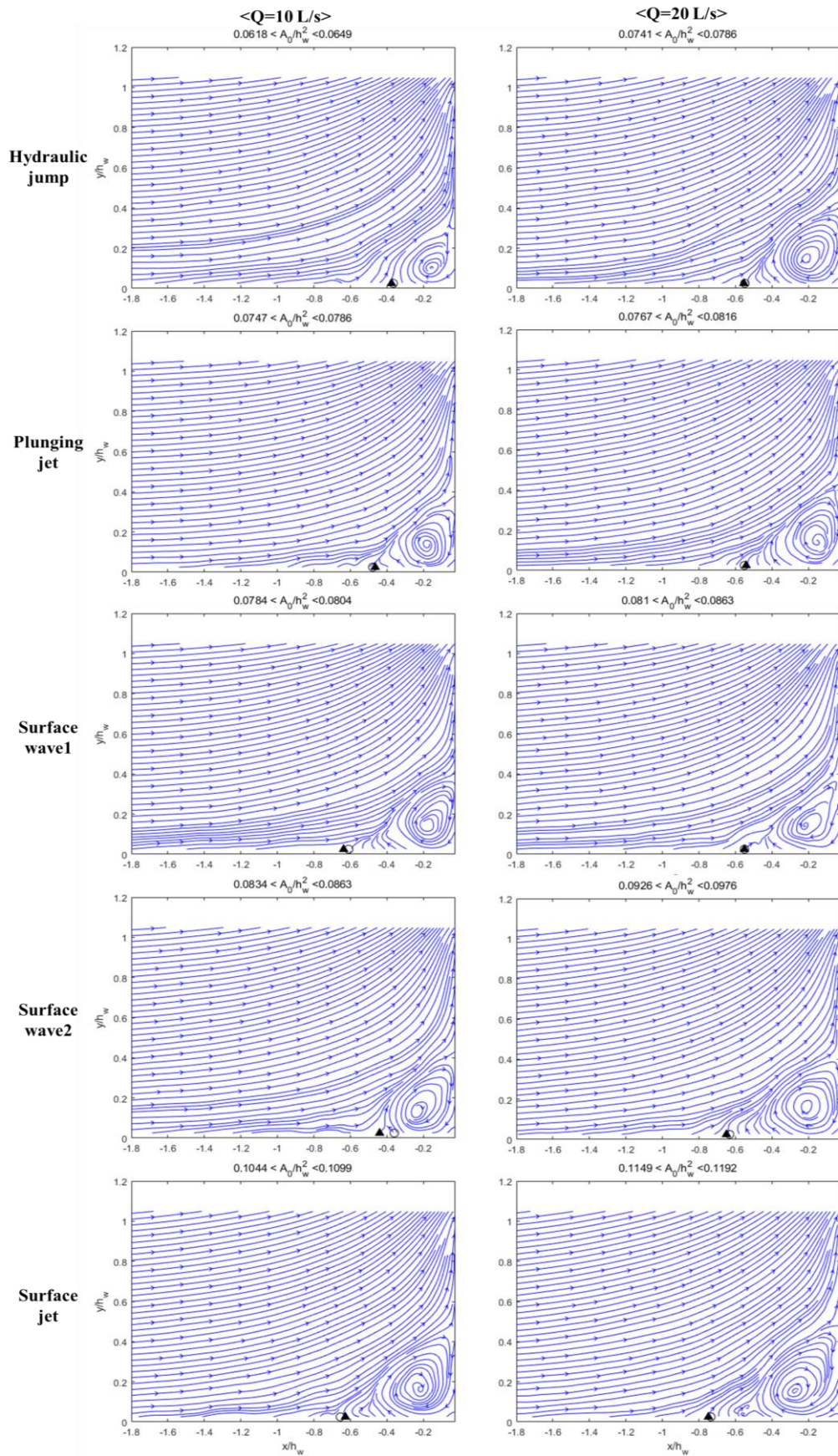


Figure 4.12 Streamlines of the maximum five flow fields

1999; Lanzerstorfer & Kuhlmann, 2012) and turbulent flow (Pearson et al., 2013) when the oncoming boundary is larger than step height,  $\delta/h_s > 1$ . From the streamlines of the extreme events shown in Figure 4.12, a huge separation flow covers the whole weir front and evacuates over the edge. This mechanism referred as a streak is enhanced at the weir in the river with  $\delta/h_w < 1$ .

To examine the portion of closed form in entire velocity fields, the streamlines of the first closed separation flow with separation points were estimated and depicted in Figure 4.13. The conditional averaging of 25 subsets is used to make 18 series. The streamlines from the boundary layer pass the recirculating vortex and travels to the upstream edge. The size of the reverse flow at the first closed form is in the Table 4.1, and it is found that the first case exceeds median of the reverse flow at all cases. Therefore, approximately 40% of the separation flow formed bottom in front of the weir is closed.

Figure 4.14 shows the size of the reverse flow of each subset with corresponding separation points estimated by the mean zero shear method. The majority of the spatial region of the reverse flow is less than  $0.15h_w^2$ , and few are located far from this region. This is well agreed with the right-skewed distribution in Figure 4.8 where most of the reverse flow located at the small  $A_0$  and only few are large. The separation points have a linear relationship with the size of the reverse flow in this major region, but they remain relatively unvarying for the large infrequent event. It is because the separation region overflows the weir into the downstream flow, which is identical to the results of FFS from Pearson et al. (2013).



**Figure 4.13** Streamlines of the first closed separation flow

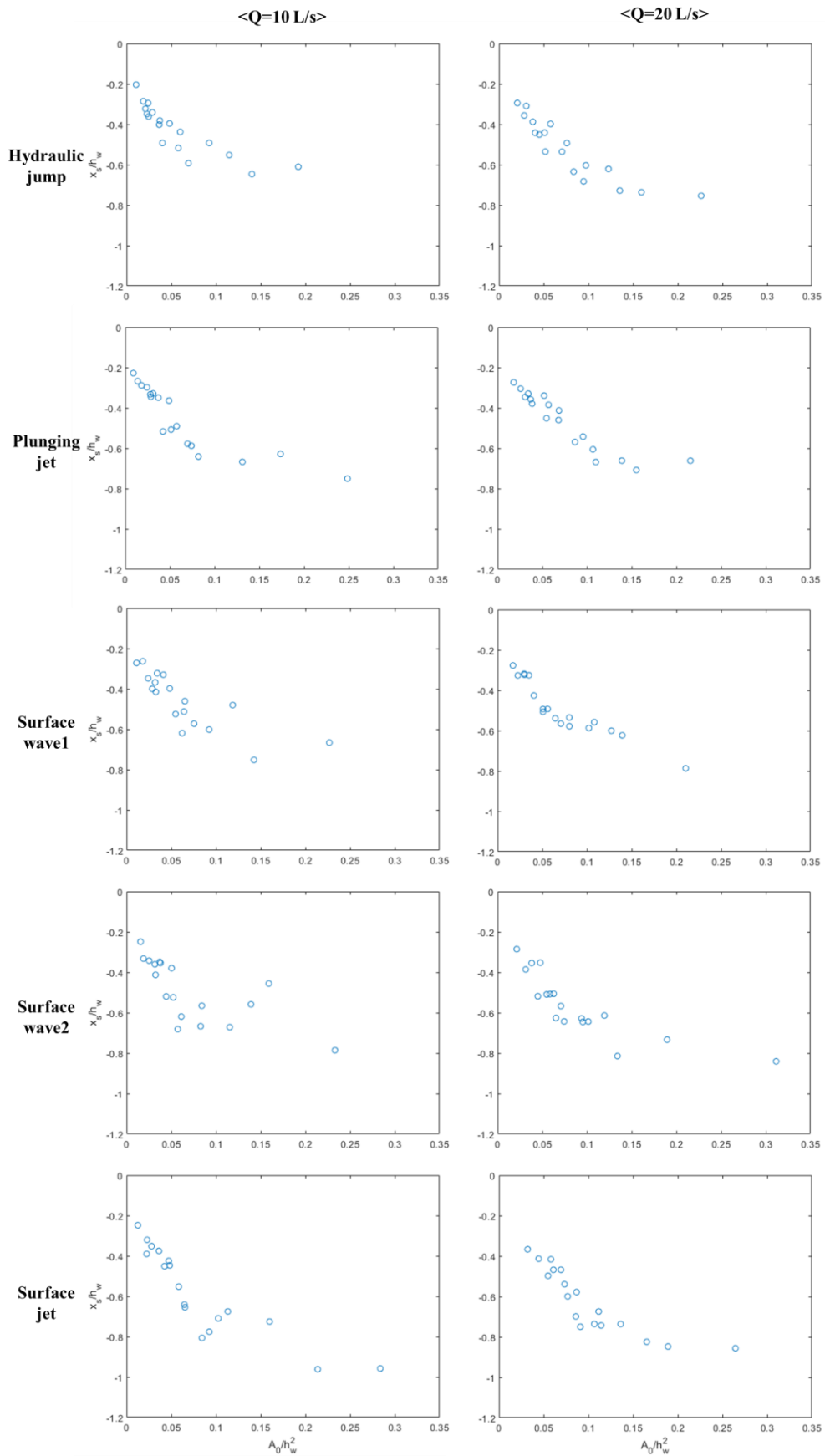


**Figure 4.14** Comparison of the separation points with area of reverse flow

### 4.1.3. Snapshot Proper Orthogonal Decomposition

The flow was analyzed to estimate the deterministic velocity components from the fluctuation velocity by means of the snapshot proper orthogonal decomposition (SPOD). POD is useful procedure to identify primary features in experimental and numerical velocity fields. The merit of POD is that it produces an empirical optimal orthogonal functions within a given flow. POD has been successfully employed to other researches in the flow around bluff body (Kostas et al., 2005; Mathis et al., 2009; van Oudheusden et al., 2005; and Sherry et al., 2010). To be specific, Huang (1994) and Kostas et al. (2005) used POD at the backward facing step and found dominant fluctuating motion. In this study the SPOD was implemented to the instantaneous velocity fields and the field of view is  $x/h_w = -1.5$  and is  $y/h_w = 0.9$ . The size of the field of view in the vertical direction was reduced to focus on the flow at the bottom upstream of the weir.

Figure 4.15 shows the energy level of each mode in the first 15 modes. The first and second modes respectively represent 18 ~ 27% and 7 ~ 12 % of the fluctuation velocity. The energy rapidly decays as the mode number increases and goes below 1% after 15th mode. About 80% of the energy located in the first 50 modes. Although the energy level poorly distributed compared to the flow of large coherent motion including Von-Karman vortex street, this agrees with the POD results of the flow separation at the backward facing step (Huang, 1994; and Kostas et al., 2005).

Figure 4.16 to 4.19 represent the first and second mode of the streamwise and vertical fluctuation velocity. the energy level and magnitude of each SPOD mode are depicted in the Figures. The color-bars of these Figures are not unified to maintain the orthogonality of the SPOD modes. The spatial distribution of the first two SPOD modes are similar regardless of the different hydraulic conditions.

The strong coherent structure from the first mode of the streamwise fluctuation velocity is developed above the rotating streamlines to the upstream edge. This structure is anti-correlated to the lower part of the rotating streamlines. For the second mode of the streamwise fluctuation velocity, the strong coherent structure is created closed to the position of the structure in the first mode. This structure is anti-correlated to the upstream flow structure. For the SPOD mode of the vertical fluctuation velocity, anti-correlated coherent structures are developed at the area of the ascending and descending streamlines of the recirculation zone.

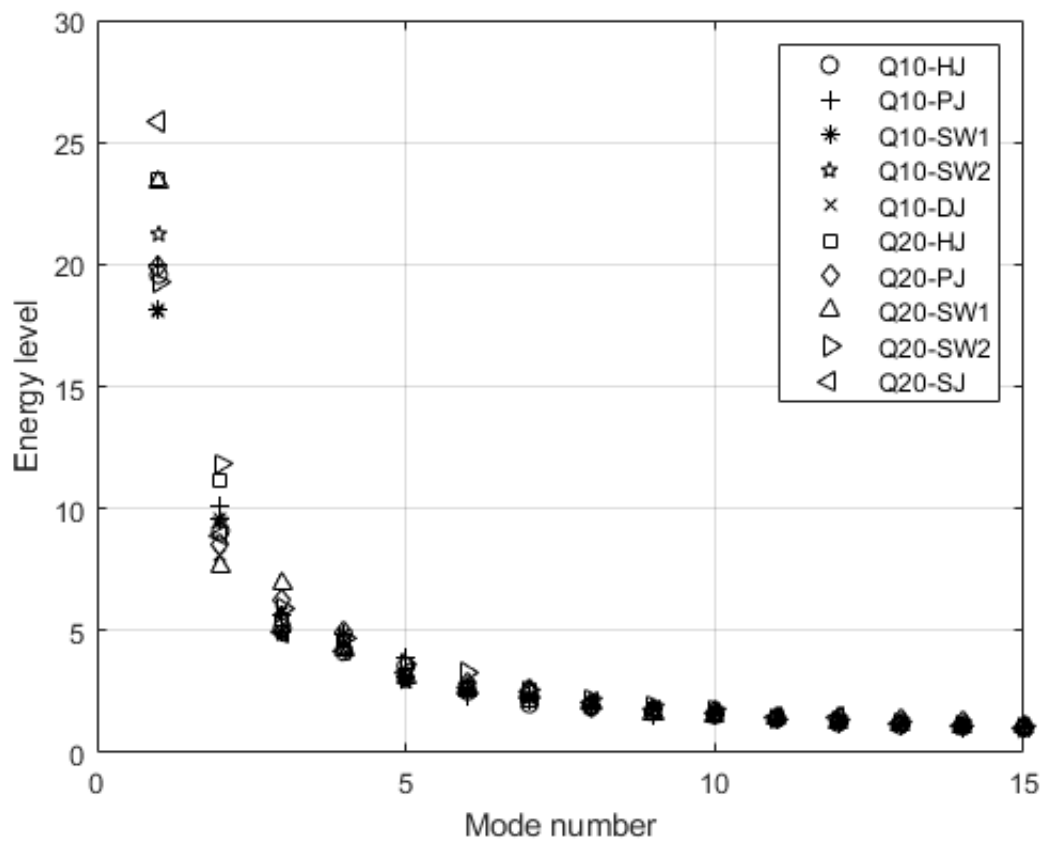


**Figure 4.15** Energy level of the POD modes

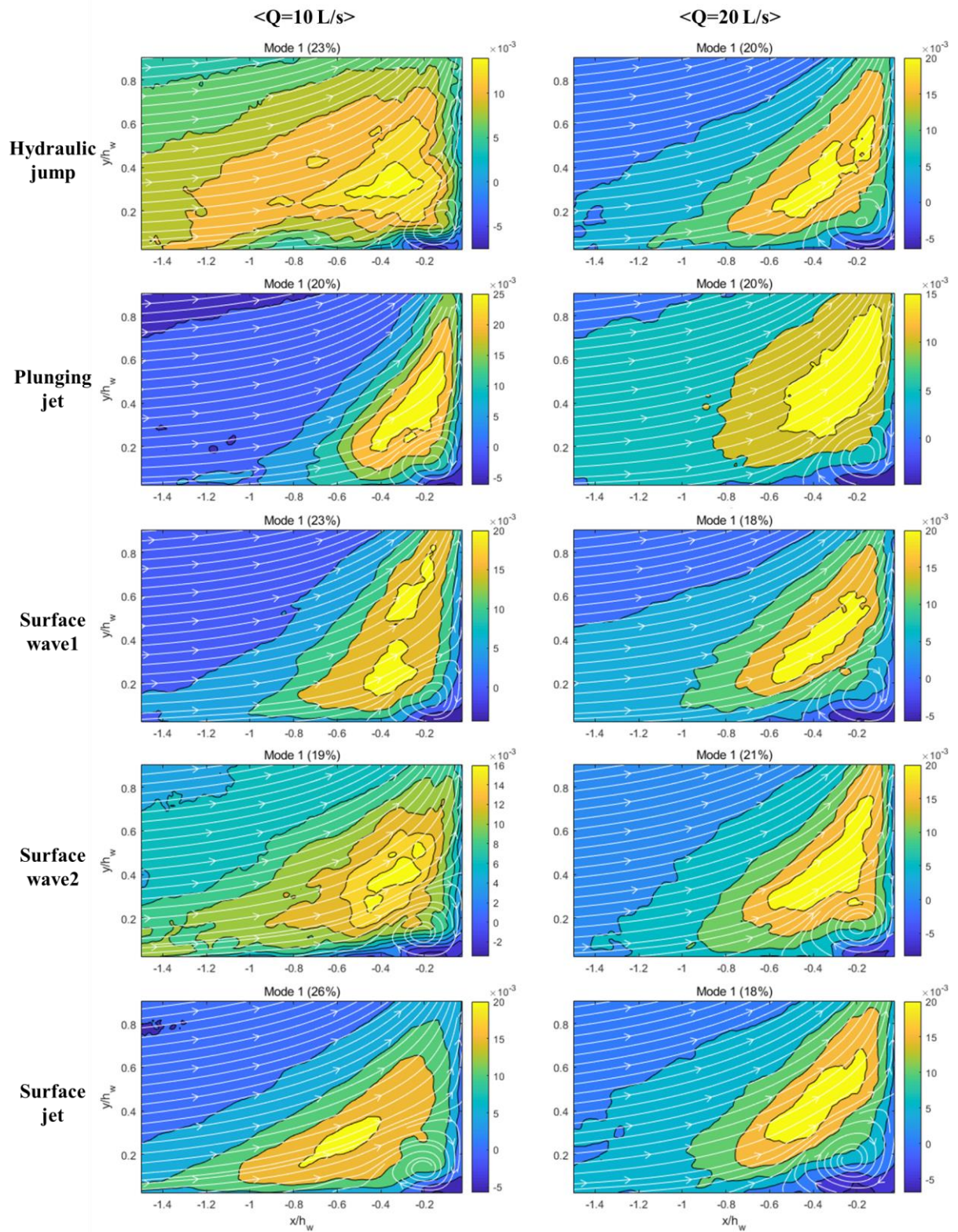


Figure 4.16 First SPOD mode of the streamwise fluctuation velocity.

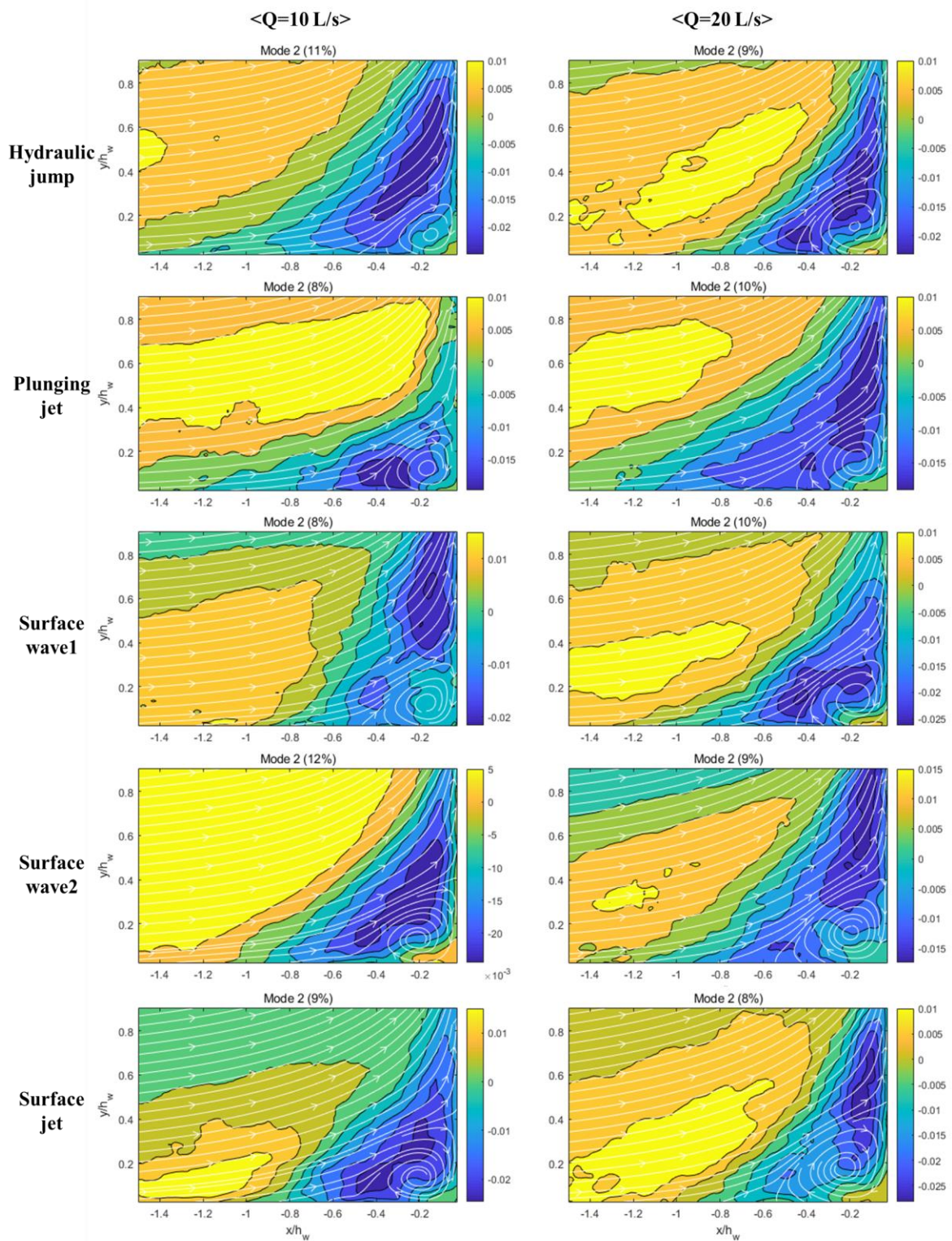


Figure 4.17 Second SPOD mode of the streamwise fluctuation velocity.

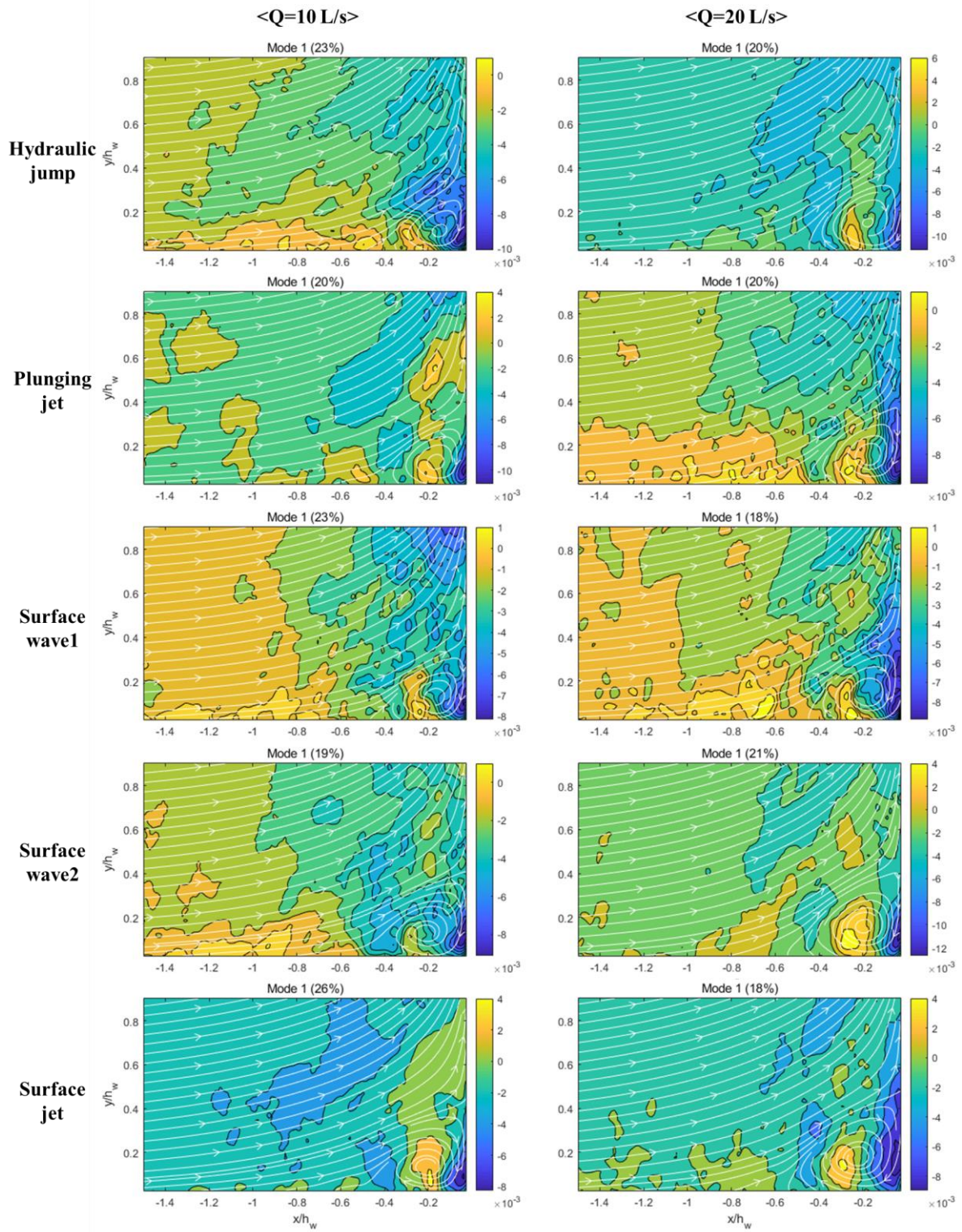


Figure 4.18 First SPOD mode of the vertical fluctuation velocity.

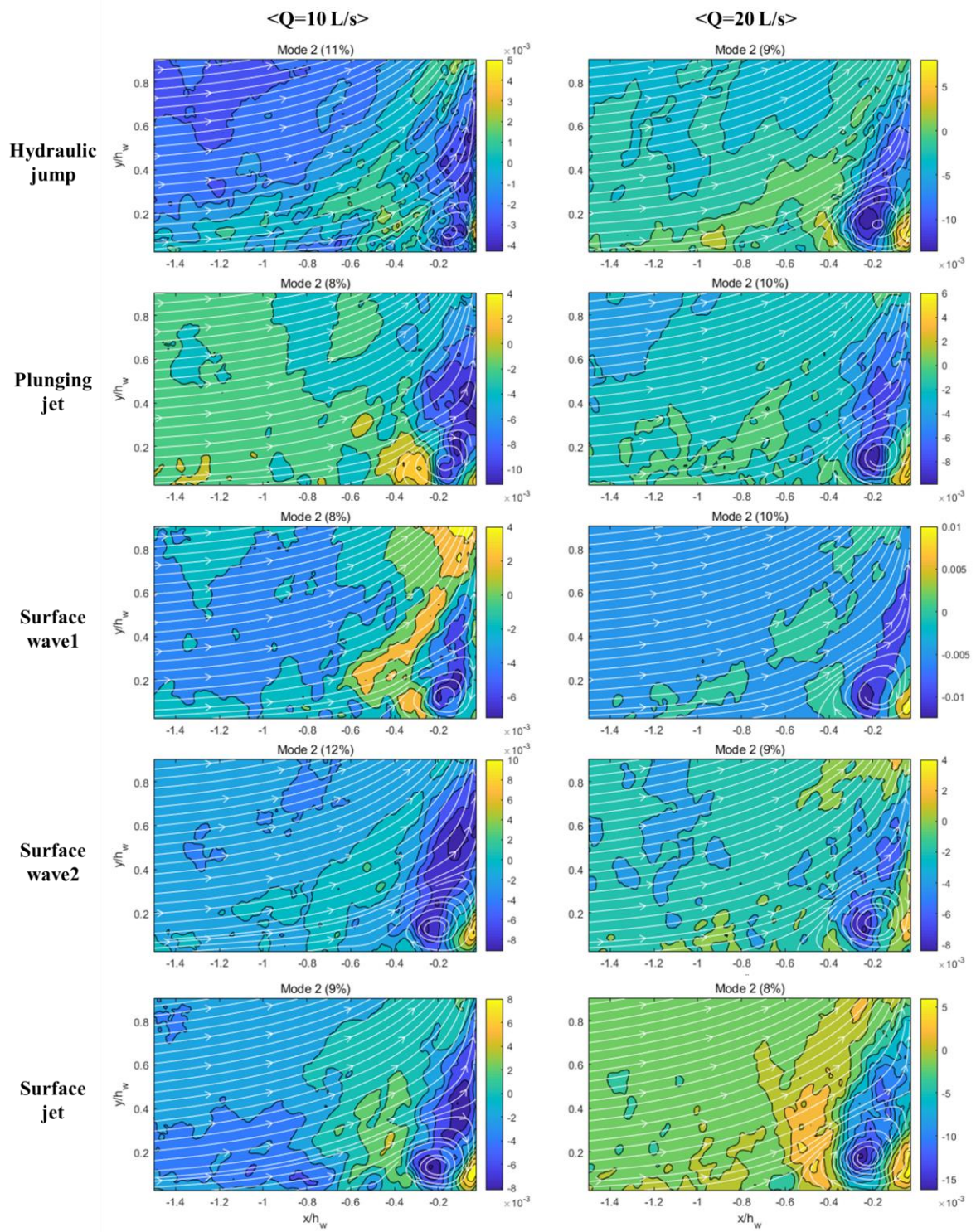
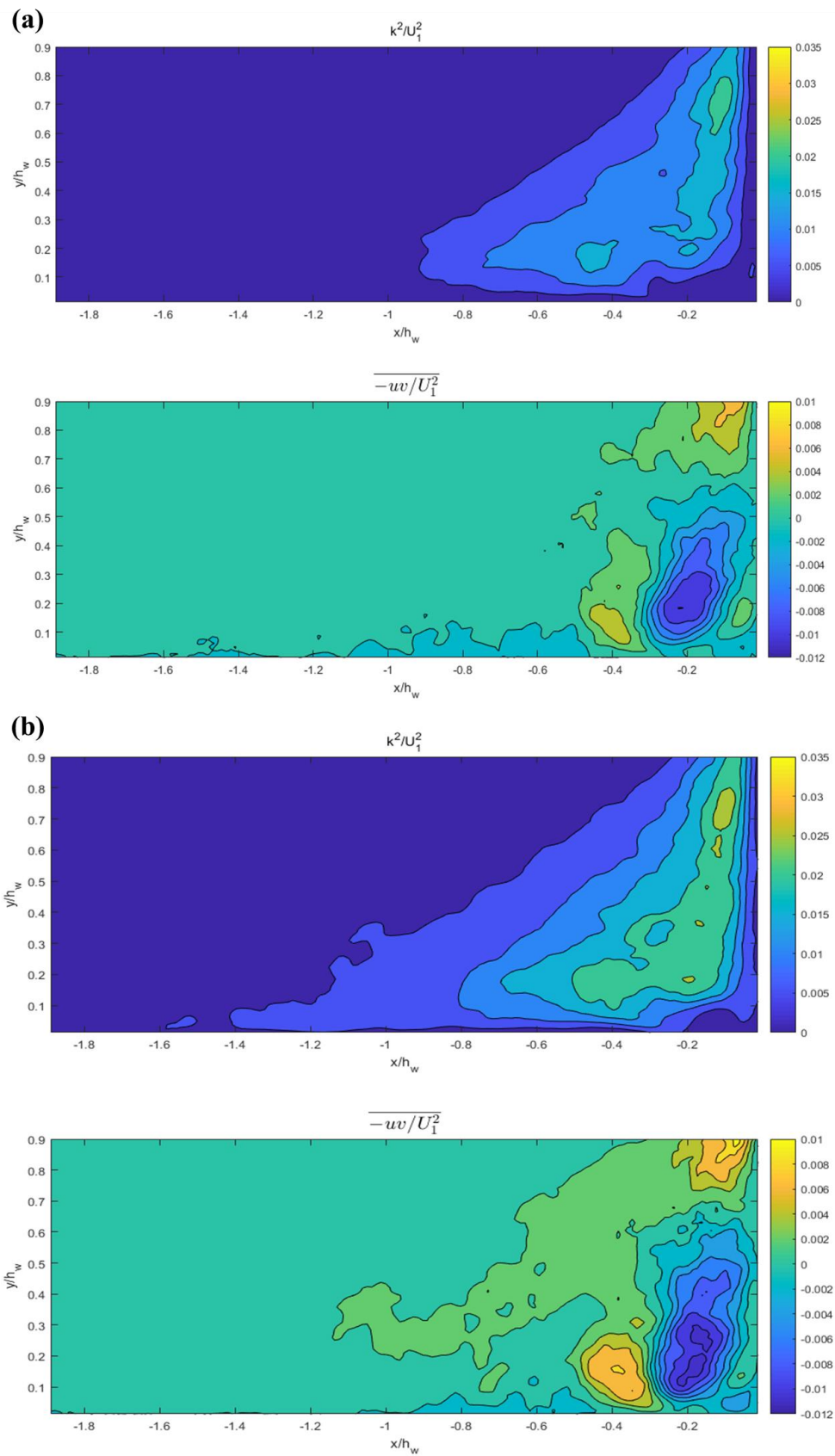


Figure 4.19 Second SPOD mode of the vertical fluctuation velocity.

The TKE and Reynolds stress fields were estimated from the first 10 and 50 modes in the *Q20-HJ* case shown in Figure 4.20. To compare the magnitude of TKE and Reynolds stress from the fluctuation velocity, the color-bar was matched presented in the Figure 4.6. The structures of the TKE fields and Reynolds stress fields generated by SPOD modes were comparable to the original fields at the bottom upstream of the weir. However, the fields of first 5 and 20 mode do not represent fluctuation after  $x/h_w = -1$ . It is because the front modes mainly represent large motion before  $x/h_w = -1$ . The magnitude at the maximum TKE is approximately 60 % ( $N = 10$ ) and 80% ( $N = 50$ ) of the maximum value of the original fluctuation in the same location of TKE field. However, choosing large number of modes for velocity reconstruction can deteriorate estimation of the turbulence properties since indeterministic motion were derived at the higher mode in the SPOD. Compared to the flow with strong deterministic motion, such as Von-Karman street behind a circular cylinder, the flow upstream of the weir does not have strong deterministic motion except the first few modes.



**Figure 4.20** TKE and Reynolds stress of the (a)  $N = 5$  and (b)  $N = 20$

## 4.2. Analysis of Separation and Reattachment Point

Flow structure and the region of separation can be inspected from the streamline pattern. However, it is difficult to precisely identify the exact location of separation point. This difficulty arises due to the combination of the unsteadiness in large turbulent structure and the unsteadiness related to the fluctuating motion of separation point. (Simpson, 1989). Therefore, to learn more about the exact location of separation, the positions of zero mean shear and 50% fraction of time were investigated.

Displacement estimation of PIV process was recalculated at the bottom and side wall region to estimate separation and reattachment point. It is because images at the wall have noise produced by surface glare or deflection light from sediment particles, which is normally larger than seeding particles. To be specific, if the sediment particles stay at the bottom, true displacement vector may not be found since the signal generated by the sediment is larger than that of mobile seeding particles. This effect increase when the size of interrogation is small. Therefore, the first pixels next to the wall were deleted, and the separation points were estimated from the distribution of the streamwise velocity at the second pixels. This means that the separation points were estimated 2mm far from the wall. The separation points derived from the zero mean shear and fraction of time method and the reattachment points are summarized in Table 4.1.

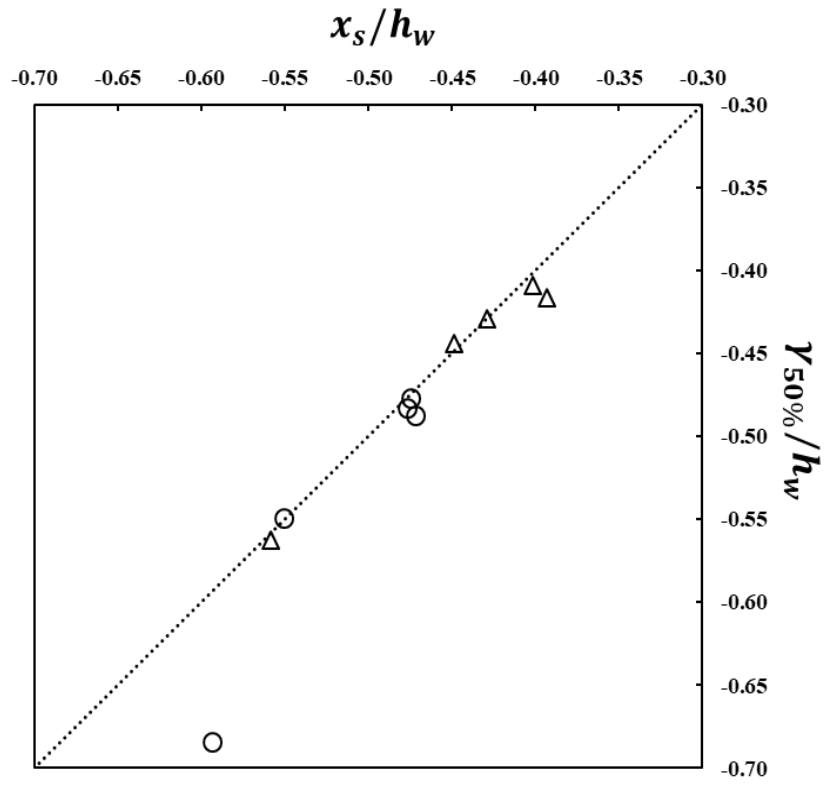
**Table 4.2** Normalized separation and reattachment points with experimental hydraulic parameters.

	Case	$h_1$ (m)	$u_1$ (m)	$Re_w$	Fr	$h_1/h_w$	$x_s/h_w$	$y_s/h_w$	$\gamma_{50\%}/h_w$	$\gamma_{80\%}/h_w$	$\gamma_{99\%}/h_w$
Q=20 l/s Re=33,333	Q20-HJ	0.179	0.187	19,420	0.141	1.716	-0.477	0.391	-0.483	-0.761	-1.300
	Q20-PJ	0.180	0.185	19,252	0.139	1.731	-0.474	0.394	-0.477	-0.751	-1.134
	Q20-SW1	0.181	0.184	19,145	0.138	1.741	-0.472	0.390	-0.487	-0.732	-1.214
	Q20-SW2	0.200	0.167	17,375	0.119	1.918	-0.551	0.427	-0.549	-0.824	-1.279
	Q20-SJ	0.225	0.148	15,438	0.100	2.159	-0.593	0.479	-0.684	-0.891	-1.387
Q=10 l/s Re=16,667	Q10-HJ	0.154	0.108	11,242	0.088	1.483	-0.402	0.321	-0.409	-0.799	-1.344
	Q10-PJ	0.155	0.107	11,176	0.087	1.491	-0.393	0.358	-0.416	-0.770	-1.220
	Q10-SW1	0.155	0.107	11,153	0.087	1.494	-0.429	0.361	-0.429	-0.784	-1.250
	Q10-SW2	0.170	0.098	10,195	0.076	1.635	-0.449	0.413	-0.444	-0.887	-1.442
	Q10-SJ	0.198	0.084	8,763	0.060	1.902	-0.558	0.428	-0.563	-1.019	-1.542

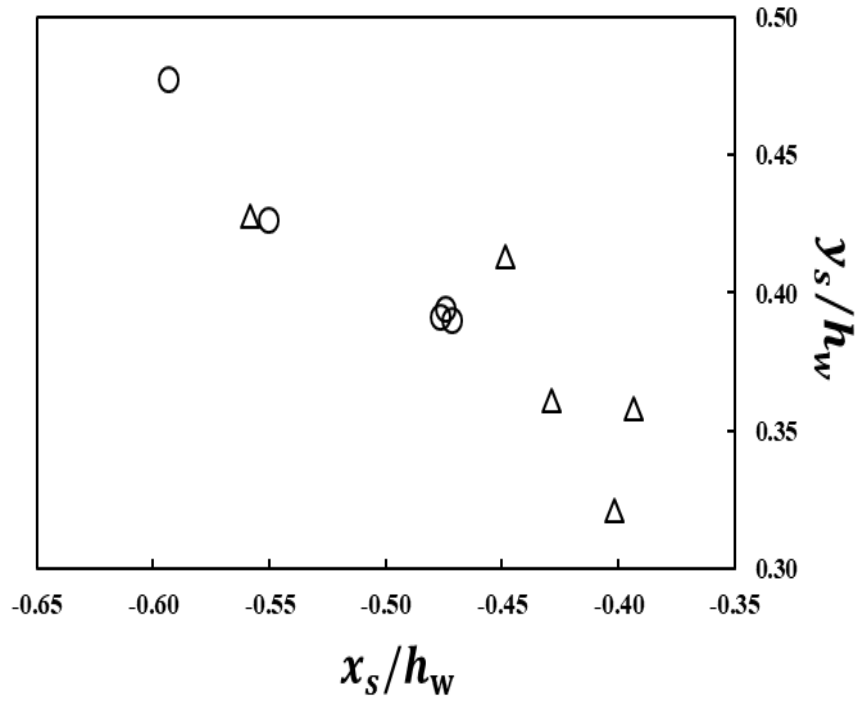
The locations of the separation points estimated by the method on mean zero shear stress and 50% fraction of time are shown in Figure 4.21. The circular points and the triangle points are  $Q = 20$  L/s and  $Q = 10$  L/s cases. Most of the separation points estimated by both methods locate closely, and it is consistent to the previous studies of FFS. The relationship between separation and reattachment points are displayed in Figure 4.22. The reattachment points tend to increase when the separation point moves far away from the weir wall.

Figure 4.23 and 4.24 reveal the distance variation of the separation and reattachment points with regard to the weir Reynolds and Froude number. When the weir Reynolds and Froude number decrease at the given discharge, the distance of the separation and reattachment points rise.

Figure 4.25 shows the distance variation of the separation and reattachment points to the upstream water depth normalized by the weir height. It can be deduced that there is a In particular, the separation and reattachment points of  $Q20-SW2$  and  $Q10-SJ$  cases are placed nearby, although the discharge,  $Re$ ,  $Re_w$ , and  $Fr$  of  $Q20-SW2$  are two times larger than those of  $Q10-SJ$ . Therefore, it can be inferred that the separation and reattachment points upstream of the weir are highly dependent on the upstream water depth.

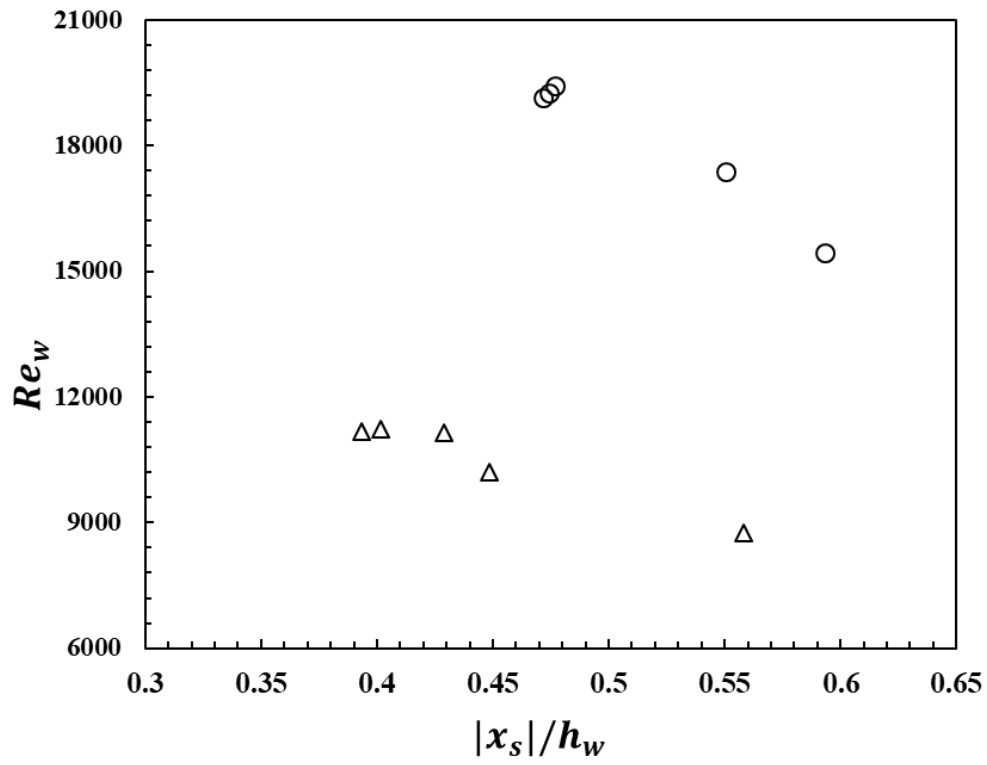


**Figure 4.21** Comparison of separation point derived by the mean zero shear stress and 50% fraction of time.



**Figure 4.22** Relationship between separation and reattachment points.

(a)



(b)

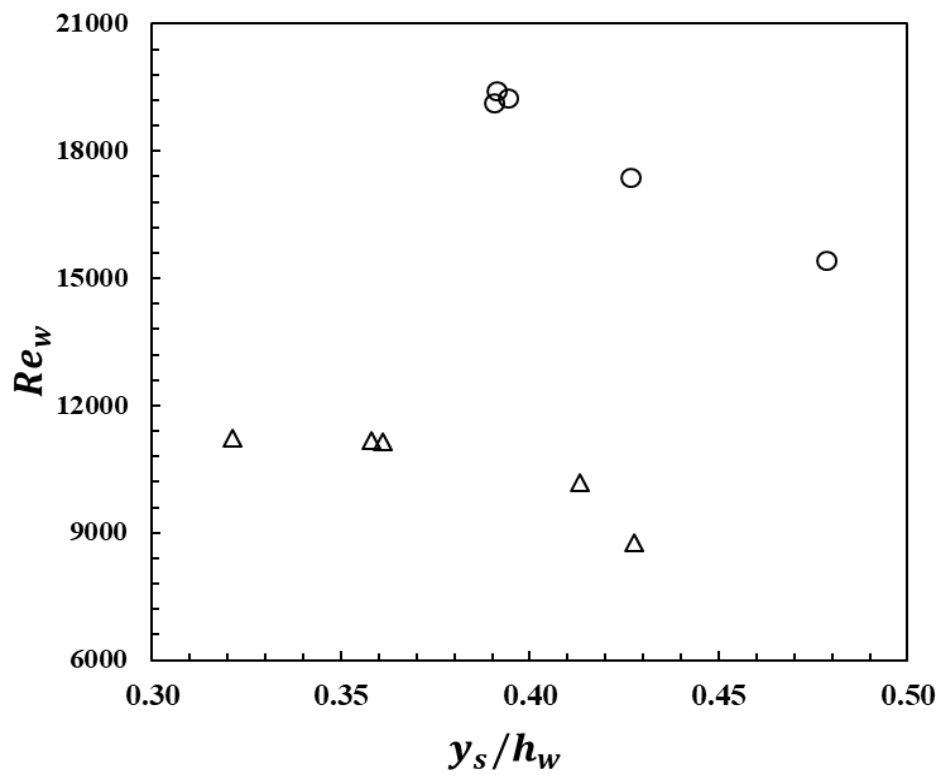
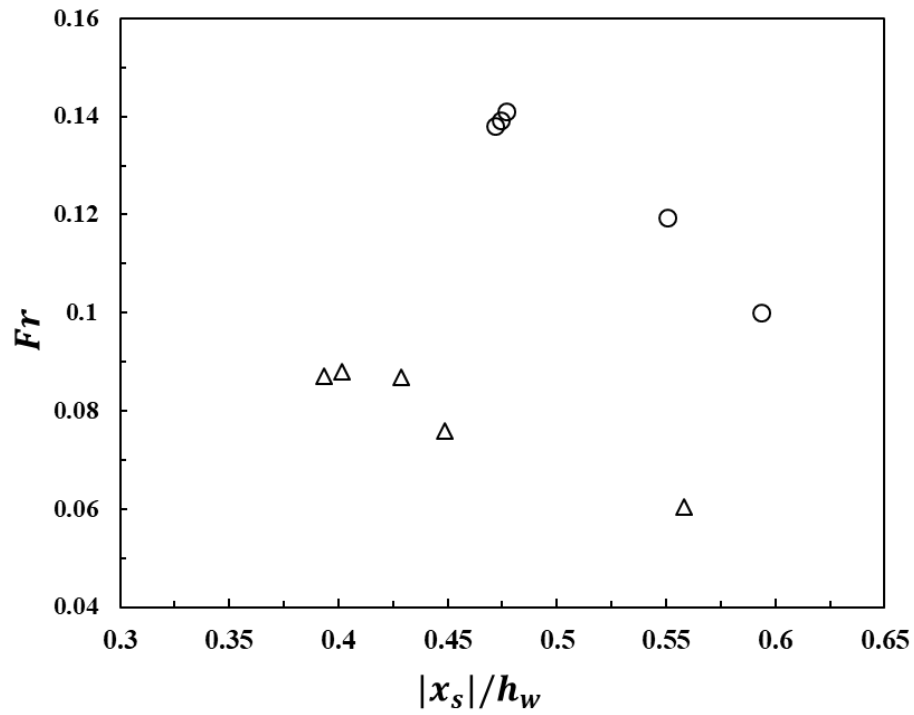


**Figure 4.23** Variation of the separation (a) and reattachment points (b) with  $Re_w$

(a)



(b)

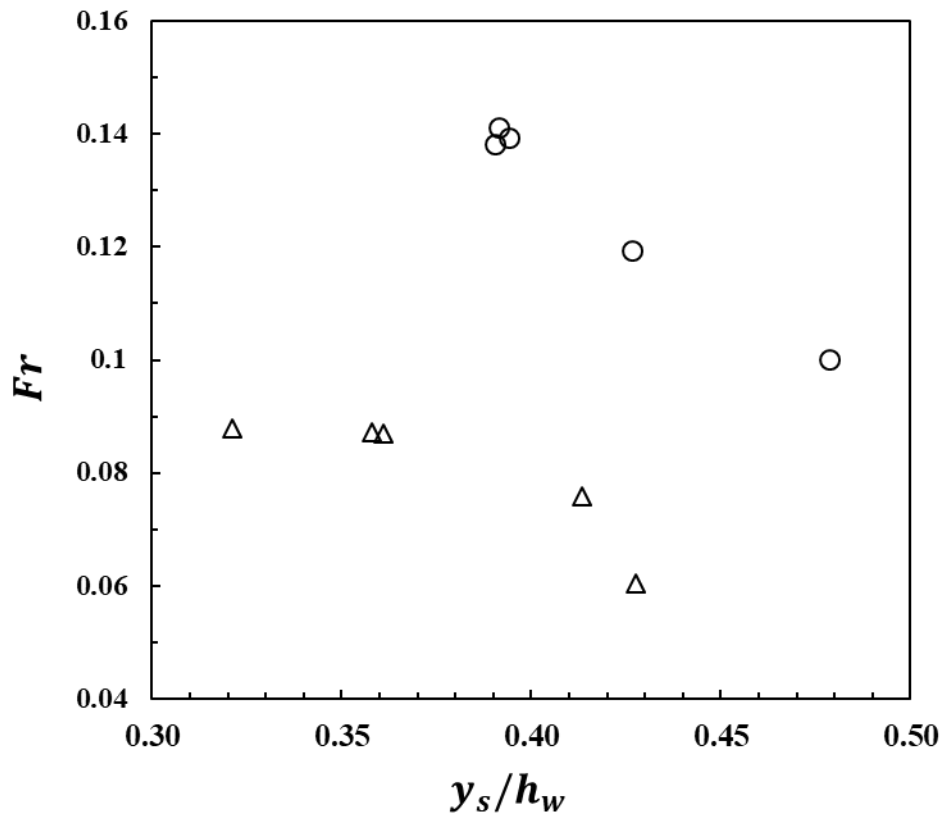
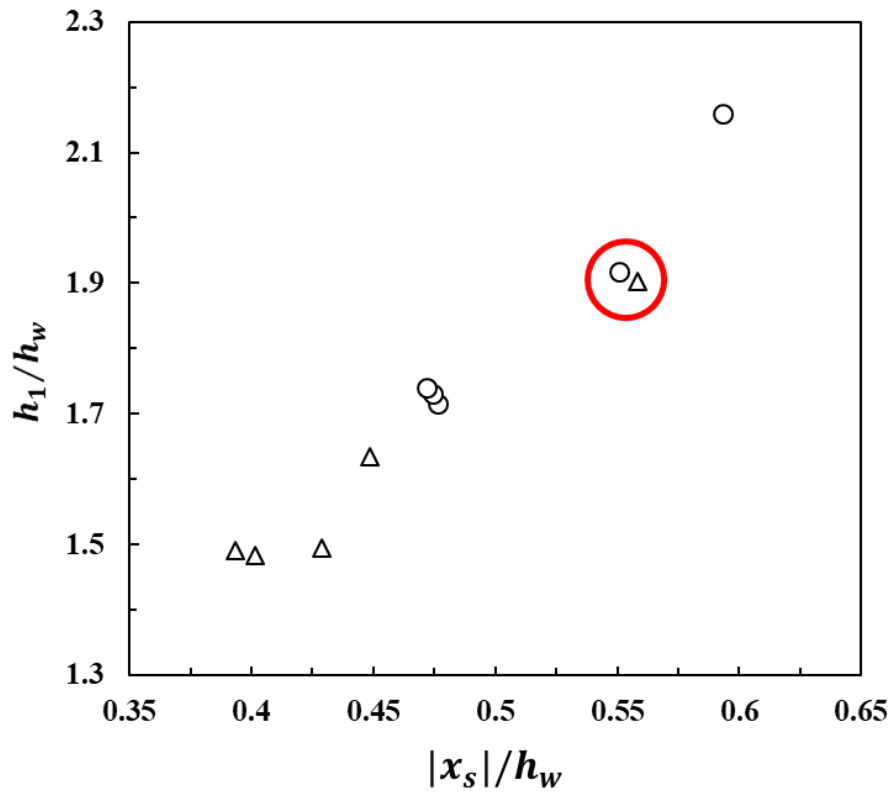


**Figure 4.24** Variation of the separation (a) and reattachment points (b) with  $Fr$

(a)



(b)

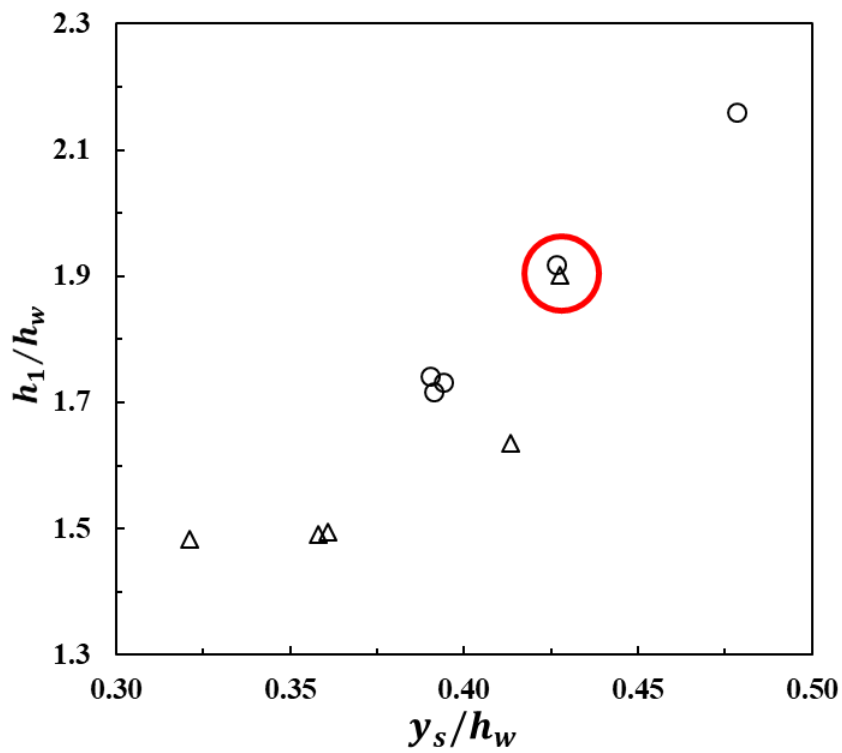


**Figure 4.25** Variation of the separation (a) and reattachment points (b) with  $h_1/h_w$

## 5. Conclusion

### 5.1. Summary

Complex flows are developed around the riverine weir. In this study, widely constructed finite crested weir with the vertical front and the downstream ramp was used for surrogate of the riverine weir. The recirculating flow generated upstream of the weir has a significant influence on the sediment entrainment, pollutant transport, and the discharge capacity. Particularly, sediment erosion due to recirculation flow could lead to critical damage to the structure. Although extensive researches on the weirs have been carried out, the flow upstream of the weir has not been studied widely.

The similar flow was developed upstream of the FFS, and it has been broadly investigated. However, the flow at FFS and the weir are different in that the step is fully submerged at the flow, whereas the flow at the weir is bounded by the upstream water depth, which has comparable scale to the weir height in general. The upstream water depth can be altered by the downstream water depth in the same discharge. Furthermore, the oncoming boundary layer is usually lower than the weir height, while that of FFS experiments is larger than the step height.

In this study, the flow separation upstream of the finite crested weir with the downstream ramp has been investigated. The laboratory experiments were carried out considering various water surface profiles around the weir. Two-dimensional standard planar PIV was used to get the instantaneous velocity fields.

The region of recirculation was detected from the streamlines calculated by the mean streamwise and vertical velocity. The mean flow fields reveal the acceleration at the front edge of the weir, and the deceleration at the channel bottom when the flow approaches. The

magnitude of the RMS velocity and Reynolds stress increases in the vicinity of the recirculation center.

To estimate the intensity of the separation flow, the conditional averaging of the total area of the reverse streamwise flow was applied. The region of reverse flow has right-skewed distribution and always larger than 0 meaning reverse flow always exists. About 40% of the separation flow is the closed-form, which is no longer in-plane entrainment exists from the oncoming boundary layer. For the extreme events of the reverse flow, the separation region upstream of the weir ejects over the weir. This indicates that the separation over the weir is partially affected by upstream separation flow. Finally, the relationship between the separation points and the area of reverse flow was analyzed. For the small size of reverse flow, both are linearly increased. However, the separation points are changed small amount, whereas the area increases a lot at the significant, infrequent events. This means that the separation points are bounded from the oncoming flow, but the area increases since the reverse flow climbs the weir front.

Snapshot Proper Orthogonal Decomposition was employed to derive the deterministic flow structure in the fluctuation velocity fields. The first few modes of the streamwise and vertical velocity under different hydraulic conditions have similar shapes. About 80% of the energy level was detected in the first 50 modes. Coherent structure at the first mode of streamwise velocity is located close to the center of rotating vortex and upstream edge. For the flow fields of the first mode of vertical fluctuation velocity has strong anti-correlated motion around the center of the recirculation.

The separation and reattachment points were evaluated employing zero mean shear and fraction of time method. As the Froude and weir Reynolds number decreases, the separation

and reattachment points extend. However, the separation and reattachment points are strongly dependent on the upstream water depth.

## Reference

- Adrian, R. J. (1991). Particle-imaging techniques for experimental fluid mechanics. *Annual review of fluid mechanics*, 23(1), 261-304.
- Adrian, R. J. & Moin, P. 1988 Stochastic estimation of organized turbulent structure: homogeneous shear flow. *J. Fluid Mech.* 190, 531–559.
- Adrian, R. J., & Westerweel, J. (2011). *Particle image velocimetry* (No. 30). Cambridge University Press.
- Adrian, R., & Yao, C. S. (1984). DEVELOPMENT OF PULSED LASER VELOCIMETRY (PLV) FOR MEASUREMENT OF TURBULENT FLOW. In Unknown Host Publication Title (pp. 170-186). Univ of Missouri-Rolla.
- Adrian, R. J., & Yao, C. S. (1985). Pulsed laser technique application to liquid and gaseous flows and the scattering power of seed materials. *Applied optics*, 24(1), 44-52.
- Azimi, A. H., & Rajaratnam, N. (2009). Discharge characteristics of weirs of finite crested. *Journal of hydraulic engineering*, 135(12), 1081-1085.
- Azimi, A. H., Rajaratnam, N., & Zhu, D. Z. (2012). Discharge characteristics of weirs of finite crest length with upstream and downstream ramps. *Journal of Irrigation and Drainage Engineering*, 139(1), 75-83.
- Bruun, H. H. (1996). *Hot-wire anemometry: principles and signal analysis*.
- Chanson, H. (2000, December). A review of accidents and failures of stepped spillways and weirs. In *Proceedings of the Institution of Civil Engineers, Water and Maritime Engineering* (Vol. 142, No. December, pp. 177-188). Thomas Telford Services Ltd.
- Chen, Y., Fu, Z., Chen, Q., & Cui, Z. (2018). Discharge Coefficient of Rectangular Short-Crested Weir with Varying Slope Coefficients. *Water*, 10(2), 204.a
- Cowen, E. A., & Monismith, S. G. (1997). A hybrid digital particle tracking velocimetry technique. *Experiments in fluids*, 22(3), 199-211.
- Fritz, H. M., & Hager, W. H. (1998). Hydraulics of embankment weirs. *Journal of Hydraulic Engineering*, 124(9), 963-971.

- Guan, D., Melville, B. W., & Friedrich, H. (2014). Live-bed scour at submerged weirs. *Journal of Hydraulic Engineering*, 141(2), 04014071.
- Guan, D., Melville, B., & Friedrich, H. (2016). Local scour at submerged weirs in sand-bed channels. *Journal of Hydraulic Research*, 54(2), 172-184.
- Glezer, A., Kadioglu, Z., & Pearlstein, A. J. (1989). Development of an extended proper orthogonal decomposition and its application to a time periodically forced plane mixing layer. *Physics of Fluids A: Fluid Dynamics*, 1(8), 1363-1373.
- Gonzalez, C. A., & Chanson, H. (2007). Experimental measurements of velocity and pressure distributions on a large broad-crested weir. *Flow Measurement and Instrumentation*, 18(3-4), 107-113.
- Goodarzi, E., Farhoudi, J., & Shokri, N. (2012). Flow characteristics of rectangular broad-crested weirs with sloped upstream face. *Journal of Hydrology and Hydromechanics*, 60(2), 87-100.
- Hilberg, D., Lazik, W., & Fiedler, H. E. (1994). The application of classical POD and snapshot POD in a turbulent shear layer with periodic structures. *Applied Scientific Research*, 53(3-4), 283-290.
- Huang, H. (1994). Limitations of and improvements to PIV and its application to a backward-facing step flow. Verlag Köster.
- Jackson, T. R., Haggerty, R., & Apte, S. V. (2013). A fluid-mechanics based classification scheme for surface transient storage in riverine environments: quantitatively separating surface from hyporheic transient storage. *Hydrology and Earth System Sciences*, 17(7), 2747-2779.
- Kumar, S., Ahmad, Z., & Mansoor, T. (2011). A new approach to improve the discharging capacity of sharp-crested triangular plan form weirs. *Flow Measurement and Instrumentation*, 22(3), 175-180.
- Kundu, P. K., Cohen, I. M., & Dowling, D. R. (2012). *Fluid Mechanics*.
- Keane, R. D., & Adrian, R. J. (1992). Theory of cross-correlation analysis of PIV images. *Applied scientific research*, 49(3), 191-215.
- Kostas, J., Soria, J., & Chong, M. S. (2005). A comparison between snapshot POD analysis of PIV velocity and vorticity data. *Experiments in Fluids*, 38(2), 146-160.
- Lanzerstorfer, D., & Kuhlmann, H. C. (2012). Three-dimensional instability of the flow over a forward-facing

step. *Journal of Fluid Mechanics*, 695, 390-404.

Lauchlan, C. (2004). Experimental investigation of bed-load and suspended-load transport over weirs. *Journal of Hydraulic Research*, 42(5), 551-558.

Leclercq, D., Jacob, M., Louisot, A., & Talotte, C. (2001). Forward-backward facing step pair-Aerodynamic flow, wall pressure and acoustic characterisation. In 7th AIAA/CEAS Aeroacoustics Conference and Exhibit (p. 2249).

Lin, Y. K. (1967). Probabilistic theory of structural dynamics (Book on probabilistic theory of structural dynamics, analyzing responses of structures to random vibrations). NEW YORK, MCGRAW-HILL BOOK CO., 1967. 366

Madadi, M. R., Dalir, A. H., & Farsadizadeh, D. (2014). Investigation of flow characteristics above trapezoidal broad-crested weirs. *Flow Measurement and Instrumentation*, 38, 139-148.

Mahtabi, G., & Arvanaghi, H. (2018). Experimental and numerical analysis of flow over a rectangular full-width sharp-crested weir. *Water Science and Engineering*, 11(1), 75-80.

Moss, W. D. (1972). Flow separation at the upstream edge of a square-edged broad-crested weir. *Journal of Fluid Mechanics*, 52(2), 307-320.

Mohammadzadeh-Habili, J., Heidarpour, M., & Haghiabi, A. (2016). Comparison the hydraulic characteristics of finite crested weir with quarter-circular crested weir. *Flow Measurement and Instrumentation*, 52, 77-82.

Na, Y., & Moin, P. (1998). Direct numerical simulation of a separated turbulent boundary layer. *Journal of Fluid Mechanics*, 374, 379-405.

Pearson, D. S., Goulart, P. J., & Ganapathisubramani, B. (2011). Investigation of turbulent separation in a forward-facing step flow. In *Journal of Physics: Conference Series* (Vol. 318, No. 2, p. 022031). IOP Publishing.

Pearson, D. S., Goulart, P. J., & Ganapathisubramani, B. (2013). Turbulent separation upstream of a forward-facing step. *Journal of Fluid Mechanics*, 724, 284-304.

Raffel, M., Willert, C. E., Scarano, F., Kähler, C. J., Wereley, S. T., & Kompenhans, J. (2018). Particle image velocimetry: a practical guide. Springer.

Sargison, J. E., & Percy, A. (2009). Hydraulics of broad-crested weirs with varying side slopes. *Journal of irrigation and drainage engineering*, 135(1), 115-118.

Simpson, R. L. (1989). Turbulent boundary-layer separation. *Annual Review of Fluid Mechanics*, 21(1), 205-232.

Stier, H., Gyr, A., & Kinzelbach, W. (1999). Laminar separation on a forward facing step. *European Journal of Mechanics-B/Fluids*, 18(4), 675-692.

Thielicke, W., & Stamhuis, E. (2014). PIVlab—towards user-friendly, affordable and accurate digital particle image velocimetry in MATLAB. *Journal of Open Research Software*, 2(1).

Wang, L., Melville, B. W., & Guan, D. (2018). Effects of upstream weir slope on local scour at submerged weirs. *Journal of Hydraulic Engineering*, 144(3), 04018002.

# 초록

## 하천보 상류에서 발생하는 흐름 박리에 관한 실험적 연구

서울대학교 공과대학

건설환경공학부

환경수리학 연구실

석사과정 방 주 영

하천보 상류에서 발생하는 박리 흐름을 입자 영상 유속계를 이용하여 실험실에서 연구했다. 본 연구에서 사용된 하천보는 일반적인 유한 마루 길이를 갖고, 전방 수직 벽이며, 하류단에 경사를 갖는 형태이다. 이는 하천설계기준을 기반으로 제작되었고, 수리 조건은 보의 상하류단 수심 관계를 이용하여 실험을 진행하였다.

평균 수직-수평 방향 유속을 가지고 계산한 유선에서 보 하방 재순환 흐름이 관측되고, 이 흐름은 외부 흐름에 의해 닫혀 있다. 역방향 흐름도 이 지역에서 발견된다. 제곱 평균 제곱근 장애선 불안전안 흐름이 재순환 흐름의 회전 중심에서 매우 강하게 발생한다.

Snapshot Proper Orthogonal Decomposition 을 이용하여 보 상류단의 결정론적 흐름을 추출하였다. 첫번째 모드는 약 20 ~ 25 %의 에너지를 갖고, 처음 3 번째 모드 까지는 크기의 차이는 존재하지만 비슷한 형상이 도출되었다.

역방향 흐름의 전체 면적에 대한 조건부 평균화를 이용하여 각각의 시간대에서 박리 흐름의 강도를 측정하였다. 재순환 흐름의 면적은 오른쪽으로 기울어진 분포를 가지고, 항상 0보다 큰 값을 가졌다. 약 40%의 박리 흐름은 닫힌 형태를 가진다. 상류의 분리 흐름에서 대규모 흐름 방출이 관측되고, 이는 보 상단에서 발생하는 재순환 흐름이 보 전방의 재순환 흐름과 연계되어 있음을 의미한다. 역방향 흐름의 면적과 그 상태의 박리 지점의 관계를 파악하였다. 이 관계를 통해, 역방향 흐름의 면적이 오른쪽으로 기울어진 분포를 가짐과 대규모 흐름 방출 현상을 해석할 수 있었다.

박리 지점과 재부착 지점을 평균 전단 응력이 0인 지점과 흐름이 하류로 흐르는 비율이 50%인 지점을 이용하여 추정하였다. 박리 지점과 재부착 지점은 보의 높이를 기준으로 하는 레이놀즈수와 상류의 프루드수에 영향을 받지만, 상류 수심에 강하게 영향을 받는다.

표제어: 하천보, 입자 영상 유속계, 경계층 박리, 조건부 평균, 역방향 흐름, Snapshot Proper Orthogonal Decomposition.